

Chapter 1 Introduction

1.1 What is chromism and electrochromism?

1.1.1 Chromism

Chromism is a reversible change in the color of a compound that occurs in response to an external stimulus. Many materials are chromic, including inorganic and organic compounds and conducting polymers (CPs), and many different mechanisms are involved. In recent years, the growing interest in low-power systems has led to the development of various energy-efficient chromic technologies with promising applications in smart windows, sunglasses, and information displays.¹⁾ In most cases, chromism is based on a change in the electronic states of molecules, particularly the π - and d-electron states; hence, this phenomenon is induced by various external stimuli that can alter the electron density of substances. Many natural compounds are known to exhibit chromism, and many artificial compounds with specific chromism have been synthesized to date. Chromism is classified on the basis of the type of external stimulus that causes the color change. The major types of chromism are summarized in Table 1.1.

Table 1.1 Classification of chromism caused by external stimuli.

Chromism	Type of stimuli
Thermochromism	Heat
Photochromism	Light irradiation
Gasochromism	Gas
Ionochromism	Ions
Solvatochromism	Solvent polarity
Halochromism	Change in pH
Piezochromism	Mechanical pressure
Electrochromism	Change in potential

Thermochromism is a reversible color change of a substance induced by a change in temperature. A large variety of substances, including organic, inorganic, organometallic, and supramolecular and polymeric systems exhibit this behavior. VO_x ²⁾ and cobalt hexacyanoferrate composites are two examples.³⁾

Photochromism is a phenomenon in which a compound changes color when exposed to light of a specific wavelength and reverts to its original color when irradiated with light of a different wavelength.⁴⁾ Various transition metal oxides, such as MoO_3 , WO_3 , TiO_2 , V_2O_5 , Nb_2O_5 show color changes upon exposure to either sunlight or UV radiation.⁵⁾

Gasochromism is observed when a reversible color change is induced by the reaction of a substance with gases such as oxygen, hydrogen, or argon. Tungsten oxide⁶⁻⁷⁾ is one of the most promising examples. V_2O_5 ,⁸⁾ Mg-Ni ,⁹⁾ and Mg alloyed with alkaline-earth metals¹⁰⁾ have also been reported to exhibit gasochromism.

Ionochromism is a phenomenon in which a reversible color change is caused by the addition of ions. This phenomenon can occur in addition to photochromism and can trigger an alteration in conductivity. When ionochromism does occur alongside photochromism, both relaxed and excited states can undergo ionochromism.¹¹⁾

Solvatochromism is a reversible color change induced by solvents and often derives from a change in solvent polarity. The color change in solvatochromic compounds occurs *via* charge-transfer (CT) mechanisms. Poly(3-alkylthiophenes) are known to be solvatochromic.¹²⁾

Halochromism is observed when a reversible color change is due to a change in the pH of a solution. Halochromic compounds include phenolphthalein and titanium dioxide. The compounds themselves are weak acids or bases and become involved in acid base reactions.¹³⁾

Piezochromism involves a reversible color change in response to mechanical grinding. The induced color reverts back to the original if the material is left in the dark over time or dissolved in an organic solvent.¹⁴⁾

1.1.2 Electrochromism

Upon electron-transfer or redox reactions, certain electroactive materials undergo visible and reversible color changes with significant variations in their optical absorbance spectra. This phenomenon is called “electrochromism (EC)”. Some materials also undergo reversible color changes when a burst of charge is applied. The color changes in electrochromic materials typically involve conversion from a transparent (bleached) state to a colored state or from one colored state to another at varying voltages. A wide range of materials and structures can be used to construct electrochromic devices (ECDs) for specific applications. The electrochromic effect results from the generation of different electronic absorption bands in the visible region, which correspond to the changes in at least two redox states.¹⁵⁻¹⁷⁾

1.2 Applications of electrochromic devices

In recent years, research on EC has become very attractive due to its applicability to energy-saving facilities and extremely low energy consumption. Accordingly, electrochromic materials are now used in ECDs such as (a) smart windows, (b) anti-glare rear view mirrors, and (c) information displays, as shown in Figure 1.1. That is, ECDs can be used for various architectural and nonarchitectural applications. Architectural applications include energy-efficient glazing, privacy glasses, skylights, among others. Automotive glazing includes sunroofs and mirrors. Most recently, electrochromic windows have been used in the Boeing 787 Dreamliner. The new Boeing 787 has windows that are 50% larger than those in other commercial aircrafts (12 to 20 in), which they can darken or clear electrochromically at the touch of a button. The delicacy and cost of installation are justified by expensive air-transport considerations.¹⁸⁻²¹⁾

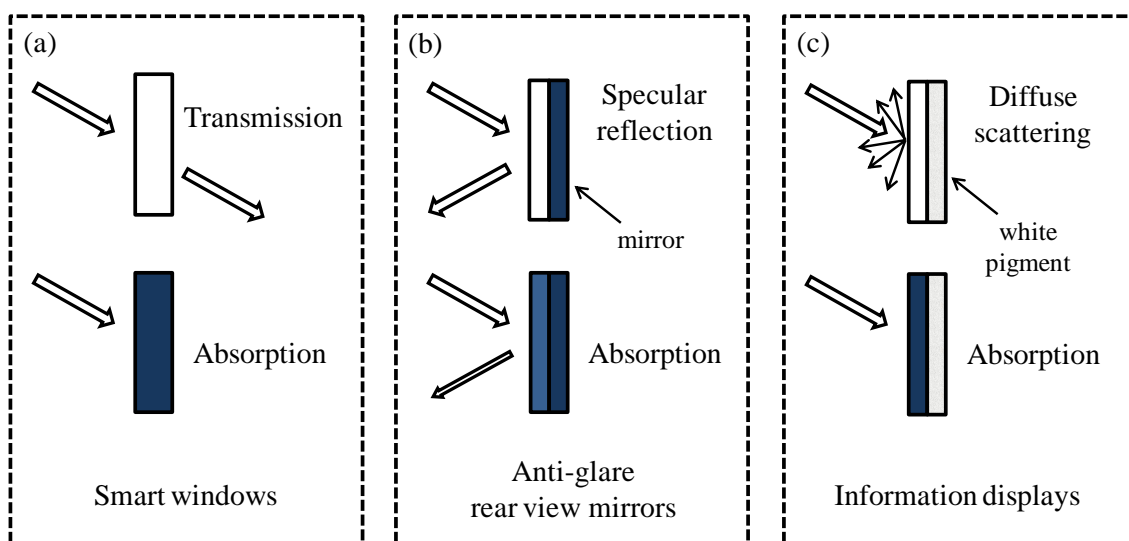


Figure 1.1 Applications of electrochromic devices.²²⁾

1.3 Electrochromic devices (ECDs)

1.3.1 Structure of ECDs

Figure 1.2 presents an illustration of the components of a standard ECD, showing the basic features and operating principles. The design embodies five superimposed layers on one substrate or positioned between two substrates in a laminate configuration. Normally, the substrates are made of glass or flexible polymer foils. The central portion consists of two conductive layers, two electrochromic layers and an electrolyte (ion conductor).

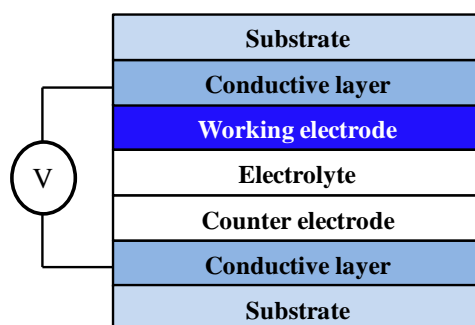


Figure 1.2 Standard construction of an ECD.

Prototype ECDs may be fabricated using optically transparent electrodes in a “sandwich” configuration, where the primary electrochromic electrode (working electrode, WE) and the charge-balancing counter electrode (CE) are separated by a layer of a liquid, gel, or solid electrolyte. Upon the application of appropriate electrode potentials, the ECD charge-discharge process provides switching between two colored states or between bleached and colored states; the ECD essentially operates similar to a rechargeable battery. For transmissive/absorptive ECDs, the CE system involves a redox reaction which undergoes an imperceptible visible color change or is composed of an electrochromic material that undergoes a color change which is complementary or reinforcing to that at the primary electrode.²³⁾ A complementary device offers the benefit of increasing coloration efficiency, which enhances the colored/bleached contrast and also promotes cycling stability by preventing undesirable side reactions between the

electrolyte and CE.¹⁵⁾ After the resulting current pulse has decayed and the color change has been effected, with little or no input of power, the new redox state persists because of the so-called “memory effect”²⁴⁾ or nonvolatile effect, which is an important property for energy-saving applications.²⁵⁾

1.3.2 Transmissive ECD and reflective ECD

There are two types of ECDs: transmissive (absorptive) and reflective.²⁶⁾ Generalized cross sections of transmissive and reflective ECDs are shown in Figures 1.3 (a) and (b), respectively.

A transmissive ECD requires that the CE, which provides electrochemical balance in these devices, be in the optical path. Hence, the CE in a transmissive ECD must be either optically passive (i.e., colorless in both oxidized and reduced states) or electrochromic in a complementary sense to the primary electrochromic element.²⁷⁾

In reflective ECDs, the CE is not visible because it is hidden behind a light-diffusing background. In this case, the CE can be made of any material that undergoes reversible electrochemistry; it is often constructed of the same material as that used for the primary electrochromic element. Reflective ECDs have an inherent white background because the micrometer scale electrolyte particles (TiO₂, polystyrene, etc.), completely scatter the light and change color by the redox reaction of electrochromic materials according to the potential.²⁸⁾

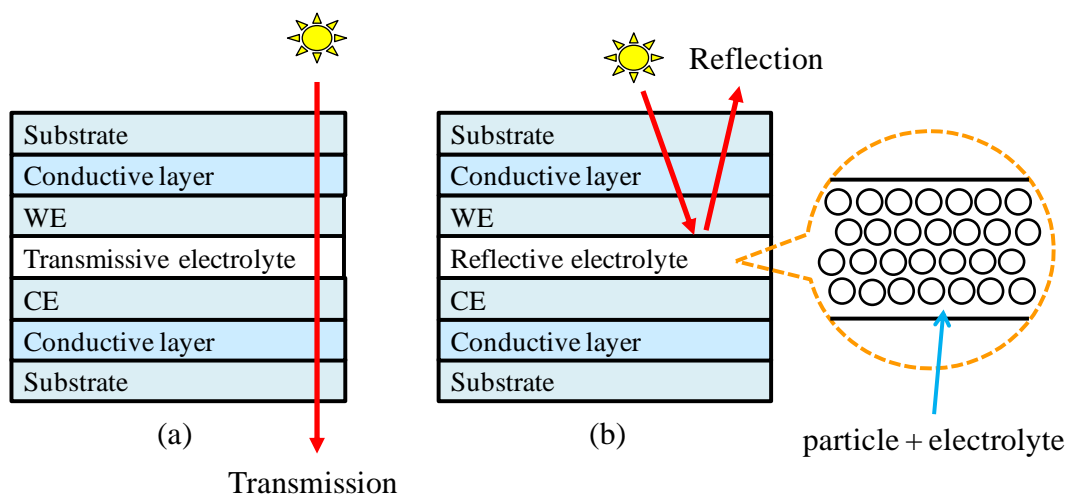


Figure 1.3 Cross-section diagram of (a) general transmissive ECD and (b) reflective ECD.

1.4 Electrochromic materials

To date, many types of electrochromic materials have been developed for ECD applications. In general, electrochromic materials can be roughly categorized into four major groups. First are metal hexacyanoferrate (MHCF) complexes such as $\text{Fe}_x[\text{Fe}(\text{CN})_6]_y$ (FeHCF, Prussian blue, PB), $\text{Ni}_x[\text{Fe}(\text{CN})_6]_y$ (NiHCF), $\text{Zn}_x[\text{Fe}(\text{CN})_6]_y$ (ZnHCF), and $\text{Cu}_x[\text{Fe}(\text{CN})_6]_y$ (CuHCF). Second are transition metal oxides such as WO_3 , NiO_x , CoO_x , V_2O_5 , and TiO_2 . Third are organic monomeric compounds such as viologen. Last are CPs such as polyaniline (PANI), polypyrrole (PPy), polythiophene (PT), poly(3-methylthiophene) (PMeT), and poly(3,4-ethylenedioxythiophene) (PEDOT).²⁹⁾

1.4.1 Metal hexacyanoferrate complexes (MHCFs)

Metal hexacyanomethylate complexes (Figure 1.4), $A_xM_A[M_B(\text{CN})_6]_y \cdot z\text{H}_2\text{O}$ ($A = \text{Li}, \text{Na}, \text{K}, \text{Rb}, \text{and Cs}$, $M_A = \text{Fe}, \text{Co}, \text{Ni}, \text{Cu}, \text{Zn}, \text{and In}$, $M_B = \text{V}, \text{Cr}, \text{Mn}, \text{Fe}, \text{and Co}$) have recently received attention as promising memory or switching materials, because their physical properties can be controlled by changing the combination and composition of their metal elements, that is, A , M_A , and M_B .³⁰⁾ In particular, MHCFs (e.g., PB and PB analogs) have attracted renewed and growing interest for electrochemical applications, such as ECDs, due to their unique structural characteristics, including a three-dimensional network and tunnel structure (Figure 1.4) and their low cost and low environmental toxicity.³¹⁻³²⁾

The redox reaction of MHCFs is shown in equation (1.1):



MHCFs composed of different metal elements possess a wide variety of chromic properties. (Table 1.2)

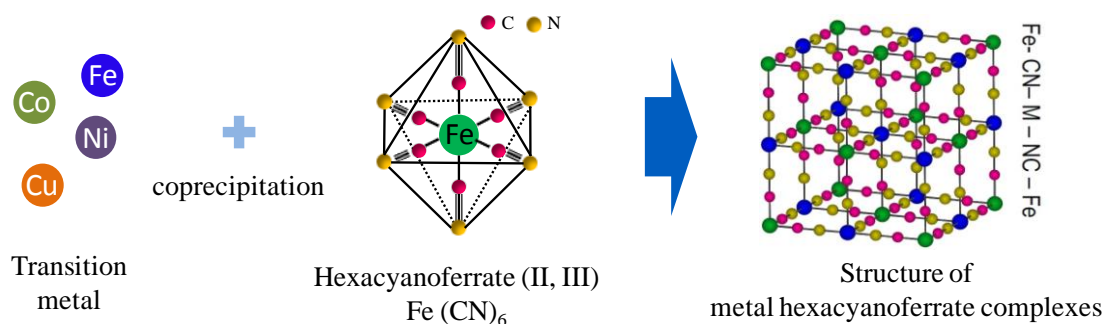


Figure 1.4 Schematic illustration of metal hexacyanoferrate complexes formed by the coprecipitation of transition metal and hexacyanoferrate components.

Table 1.2 Colors of electrochromic MHCs.

MHCF	Color		Ref.
	Oxidized state	Reduced state	
FeHCF	Blue	Transparent	29, 31
NiHCF	Yellow	Transparent	33
ZnHCF	Transparent	Transparent	34
CuHCF	Yellow	Reddish brown	35
CoHCF	Green	Reddish brown	34,36
InHCF	Yellowish	Transparent	37

Here, a brief introduction to a series of cheap insoluble MHCs, including iron, nickel, zinc and copper HCFs, is provided.

1) Iron HCF

Iron HCF ($\text{Fe}_x[\text{Fe}(\text{CN})_6]_y$, FeHCF) is a well-known synthetic coordination compound. This transition MHCF is also known as PB. Since the electrochemistry of FeHCF films was reported in 1978,³⁸⁾ numerous studies concerning the EC of MHCs have been conducted. FeHCF is an anodically coloring electrochromic material with promising electrochromic properties. It has been reported that an electrodeposited FeHCF film exhibited a blue/colorless EC transition with a fast response (≤ 100 ms) and high durability for 5×10^6 cycles.³⁹⁻⁴⁰⁾ In addition, FeHCF can be matched with a cathodic electrochromic material (e.g., WO_3) for the fabrication of ECDs with superior

performance. Several attempts at using FeHCF films for higher contrast and faster switching speeds have also been made in recent years.⁴⁰⁾ Furthermore, the excellent electrochromic performance of FeHCF makes it an ideal candidate for applications in smart windows and electronic paper displays.⁴⁰⁾

FeHCF exhibits four redox states: colorless (Everitt's salt, ES), sky blue (PB), light green (Berlin green, BG) and yellow (Prussian yellow, PY). According to previous reports, FeHCF exhibits fairly good stability in both ES and PB states.^{29,31)}

2) Nickel HCF

Among the MHCFs, nickel HCF ($\text{Ni}_x[\text{Fe}(\text{CN})_6]_y$, NiHCF) is considered as a model material for certain fundamental and applied studies for the following reasons. NiHCF films show well-defined and reproducible responses not only in supporting electrolytes containing hydrated K^+ but also in other alkali metal cations such as hydrated Li^+ , Na^+ , Rb^+ , and Cs^+ . NiHCF structures appear to be open and thus permit the unimpeded transport of alkali metal cations of different sizes while providing charge balance during the system's redox reaction.⁴¹⁾

As a film, NiHCF is also an anodically coloring electrochromic material, and NiHCF films have been used as CEs of FeHCF in ECDs. NiHCF films exhibit EC between yellow and colorless states. Correspondingly, Fe-NiHCF ECDs are blue and pale yellow in the colored and bleached state, respectively.³³⁾

Notably, NiHCF films can be readily fabricated (on various electrode substrates) by electrodeposition using potential cycling and coprecipitation methods.^{33,41)} In addition, NiHCF has very good retention properties compared with other MHCFs, and it can adsorb several elements from aqueous solutions. Furthermore, NiHCF- TiO_2 composite films exhibit interesting photoelectrochemical and/or photoelectrochromic behaviors.⁴²⁾

3) Zinc HCF

Zinc HCF ($\text{Zn}_x[\text{Fe}(\text{CN})_6]_y$, ZnHCF) is a candidate for use as a colorless CE. It is nearly colorless in both oxidized and reduced states, and it is more cost-effective than

other MHCFs.¹⁶⁾ As mentioned above, NiHCF films have been used as a CE in FeHCF ECDs; however, Ni-FeHCF ECD are pale yellow in the bleached state. In contrast, because ZnHCF is nearly transparent in both oxidized and reduced states, it is expected to be more colorless in the bleached state of ECDs. Some ZnHCFs have been reported to have hexagonal structures where the Zn atom is tetrahedrally coordinated by four N atoms of the CN ligands.⁴³⁾ However, a typical ZnHCF thin film suffers from low surface charge density, poor cycling stability, and uniformity problems, particularly when it is deposited on an ITO glass substrate.¹⁶⁾

4) Copper HCF

Copper HCF ($\text{Cu}_x[\text{Fe}(\text{CN})_6]_y$, CuHCF) exhibits two redox transitions, which are reasonably attributed to the redox activity of the $-\text{CN}$ bridged iron (III, II) and $-\text{NC}$ bridged copper (II, I) lattice ions.⁴⁴⁾ The two different metal ions, Cu and Fe, which are located in the system lattice along linear, cyanide-bridged, repeating units of the type $-\text{Fe}-\text{CN}-\text{Cu}-\text{NC}-\text{Fe}-$, are electroactive.⁴⁴⁾ CuHCF exhibits a color change from brown to pale yellow upon reduction. The electrochromic characteristics of CuHCF are thus suitable for interior architectural design applications, such as on wood and red brick. There are also many reports on the application of CuHCF for hydrogen storage,⁴⁵⁻⁴⁷⁾ cesium absorption,⁴⁸⁻⁵¹⁾ hydrogen peroxide detection,⁵²⁻⁵⁴⁾ battery electrodes,⁵⁵⁾ and electrochromic electrodes.³⁵⁾

5) MHCF nanoparticles

The importance of printed electronics for the fabrication of functional thin films and fine patterns intended for use in electronic devices has increased because solution techniques such as inkjet printing and spin coating, are simple manufacturing processes that consume less electricity and resources.⁵⁶⁾ Aqueous dispersions are also environmentally friendly, inexpensive, and compatible with the nonaqueous electrolyte solutions in ECDs.⁵⁷⁾

The conventional MHCF particles synthesized by the coprecipitation method are

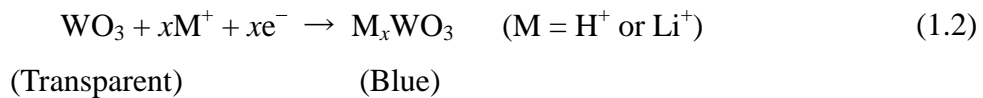
insoluble in organic and aqueous solvents. These insoluble MHCF particles are aggregate and form primary particles. Such nonuniform particle size distribution with large secondary particles is unsuitable for inkjet printing and spin coating methods. Therefore, to use MHCF thin films in ECDs, it is necessary to reduce their particle size and synthesize solvent-dispersible MHCF nanoparticles (NPs). The preparation of solvent-dispersible MHCF NPs (MHCF-NPs) has been previously proposed^{33,35,57-61)} as a new synthetic strategy for directly transforming insoluble MHCFs into MHCFs that are soluble in various solvents by convenient and simple processes that are suitable for industrial applications. Gotoh *et al.*⁵⁶⁾ and Ishizaki *et al.*⁵⁸⁾ reported water-dispersible MHCF-NPs. In these case, the insoluble MHCF aggregates were transformed into water-dispersible MHCF-NPs via surface modification using $[\text{Fe}^{\text{III}}(\text{CN})_6]^{3-}$ and $[\text{Fe}^{\text{II}}(\text{CN})_6]^{4-}$.

Table 1.3 Electrochromic transition metal oxides.

Oxides	Color		Ref.
	Oxidized state	Reduced state	
WO ₃	Transparent	Blue	62,63
TiO ₂	Transparent	Blue	62
MoO ₃	Transparent	Blue	64,65
V ₂ O ₅	Transparent	Dark yellow	62
Nb ₂ O ₅	Transparent	Green blue	62
MnO ₂	Brown	Pale yellow	66
IrO ₂	Brown	Transparent	67
RhO ₂	Dark green	Yellow	68
NiO	Brown-bronze	Transparent or pale green	69,70
Co ₃ O ₄	Brown	Transparent or green	62

1) Tungsten oxide

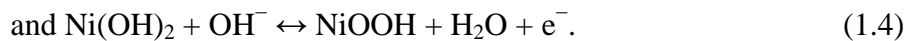
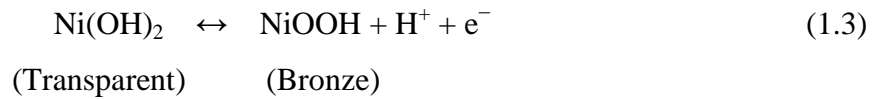
The most widely studied TMO is the tungsten trioxide (WO₃) system, because its EC was first reported in 1969. Tungsten oxide has a nearly cubic structure, which may be simply described as a type of an “empty perovskite” formed by WO₆ octahedra with shared corners. There is considerable empty space inside the cubes, and a large number of interstitial sites are present in which guest ions can be inserted. Tungsten trioxide with all of the tungsten atoms in the W^{VI} oxidation state is transparent. Upon electrochemical reduction, W^V sites are generated to give an electrochromic (blue coloration) effect. Although there is still controversy about the detailed coloration mechanism, it is generally accepted that the injection and extraction of electrons and cations (Li⁺, H⁺, among others) play an important role. WO₃ is a cathodic ion insertion material. Notably, the blue coloration in thin films of WO₃ can be erased by electrochemical oxidation. The generalized equation can be written as follows:⁶⁵⁻⁶⁶⁾



The fractional number of sites that are filled in the WO_3 lattice is indicated by the subscript x in the general formula M_xWO_3 . At low values of x , the films have an intense blue color due to photo-effected intervalence CT between adjacent W^{V} and W^{VI} sites. At higher values of x , ion insertion results in the irreversible formation of a metallic “bronze” which is red or golden in color. The process is promoted by cathodic polarization, which induces ion insertion and electron injection. The inserted ions expand the lattice of the guest oxide, while the compensating electrons modify its electronic structure, and in turn, its optical properties.

2) Nickel oxide and hydroxide

Among the promising candidates for electrochromic materials, nickel oxide (NiO_x) is attractive for a complimentary ECD, which combines the anodic brownish color of NiO_x with the cathodic blue color of WO_3 . However, the practical use of NiO_x remains restricted because of its poor capacity retention upon cycling, which correlates to a decrease in optical performance. Such a degradation phenomenon during cycling is closely related to the mechanism involved in NiO thin films.⁷⁰⁾ The electrochemical reaction between $\text{Ni}(\text{OH})_2$ and NiOOH is proposed for the EC mechanism of Ni oxide,⁷¹⁾ which is dominated by cationic transport. The reversible reactions describing the intercalation-deintercalation of ionic species can be represented as follows:^{62,72-73)}

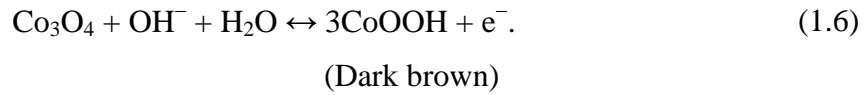
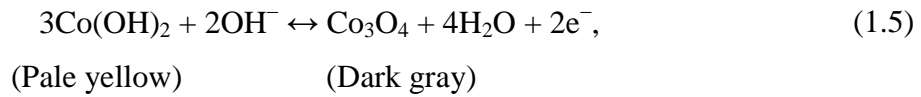


3) Cobalt oxide and hydroxide

Among typical inorganic EC materials, thin films of cobalt oxide (CoO_x) and hydroxide have recently received attention as possible electrochromic CE materials due to their comparatively lower material costs.⁷⁴⁾ Cobalt oxide is one of the many versatile

transition metal oxides with cubic spinel-type structures. Its particular properties give it a wide field of applications.⁷⁵⁾

Cobalt oxide and hydroxide films are anodically coloring electrochromic materials. They become colored by reduction processes and are used as ion storage and second EC layers. The possible electrochemical mechanisms can be expressed as follows:⁷⁶⁾



The EC behavior of Co oxide is similar to that of Ni oxide; the oxidized form is dark brown, while the reduced form is pale yellow. Co hydroxide (Co(OH)_2) and Co oxyhydroxide (CoOOH) thin films have been prepared by electrodeposition,⁷⁷⁻⁷⁸⁾ CVD,⁷⁹⁾ and sputtering⁸⁰⁾ techniques.

1.4.3 Organic compounds

Organic EC materials, including small molecules and CPS, show better EC properties than inorganic EC materials, namely, rapid optical response, high color contrast, high coloration efficiency, and various colors. In addition, these organic EC materials are typically obtained by simple procedures.

Among organic EC materials, CPs have been widely used in various applications because they exhibit several advantages, including good thermal stability, low cost, and easy preparation. CPs are organic macromolecules that consist of one or more backbone chains of alternating double and single bonds. In addition, conjugated polymers, and particularly PPy derivatives and PT derivatives, are important as electrochromic materials because they offer the possibility to develop devices with multi-color EC.

1) Viologens

Viologens are toxic bipyridinium derivatives of 4,4'-bipyridyl. The name is derived from the intensely blue color of these compounds that is observed when they are readily reduced to the radical monocation. They were first reported to possess electrochromic behavior by Michaelis and Hill in 1933.⁸¹⁾ The general chemical formula of the viologen family (4,4'-dipyridinium compounds) is shown in Figure 1.6, where R may be an alkyl, cyclo-alkyl or other substituent.¹⁷⁾

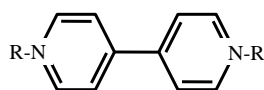


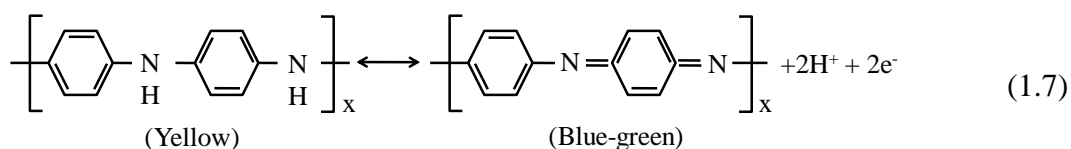
Figure 1.6 Chemical formula of viologens.

Among the viologen family, 1,1'-diheptyl-4,4'-bipyridinium (heptyl viologen, HV) and 1,1'-dimethyl-4,4'-bipyridinium (methyl viologen) are often used for EC applications. Viologens exhibit three redox states, the di-cation, radical cation, and di-reduced states, and each exhibits EC. Early applications of viologens were in aqueous electrolyte display systems. However, the leakage of solution-type devices was a potential problem. Thus, viologens were then immobilized on electrode surfaces to

form thin films by the formation of polymer complexes, functional cross-linked polymers, and electro polymerization. High switching speeds and memory effects are advantages of thin film viologen electrodes.^{17, 82)}

2) Polyaniline

One good example of an electrochromic polymer is PANI, which can be formed by either the electrochemical or chemical oxidation of aniline. If an electrode is immersed in hydrochloric acid containing a low concentration of aniline, a PANI film can be grown on the electrode. Depending on the oxidation state, PANI can either be pale yellow or dark green/black. The electrical and electrochromic properties of PANI depend on not only its oxidation state but also its protonation state, and hence the pH value of the electrolyte used. The electrochemistry of PANI thin films in aqueous acidic solutions and in organic media has been extensively investigated, and several redox mechanisms involving protonation-deprotonation and/or anion ingress-egress have been proposed. PANI films are poly electrochromic (transparent yellow to blue green), and the yellow-blue green transition is stable to repetitive color switching (equation 1.7).⁸³⁾



3) Polypyrrole

The electrochromic properties of PPy have been investigated in the thin film form. Ppy thin films are typically prepared by the electrochemical polymerization of pyrrole (either in aqueous or organic solvents such as acetonitrile, in the presence of a suitable electrolyte). Doped (oxidized) Ppy films are blue-violet (absorbance wavelength $\lambda = 670$ nm). Electrochemical reduction yields the yellow-green (absorbance wavelength $\lambda = 420$ nm) “undoped” form. The doping-dedoping process is written as follows:



The removal of all dopant anions from Ppy yields a pale yellow film. However, complete dedoping is only achieved if the Ppy films are extremely thin. The EC of Ppy is unlikely to be mainly exploited because of film degradation on repetitive color switching. CPs with improved electrochromic properties are, however, formed by the electrochemical polymerization of 3,4-disubstituted pyrrole.⁸³⁾

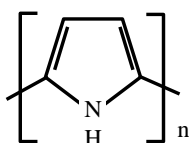


Figure 1.7 Chemical formula of PPy.

4) Polythiophene

Similar to Ppy, PT can be prepared via the electrochemical polymerization of thiophene. The electrochromic properties of PT and of the polymers of several substituted thiophenes have been reported. The tuning of the color states is possible by a suitable choice of the thiophene monomer. For example, the electrochromic properties of polymer films prepared from 3-methylthiophene-based oligomers are strongly dependent on the relative positions of the methyl groups on the polymer backbone. When a multi-color ECD is constructed, an electrochromic CP is often combined with a second electrochromic polymer showing a different specific color.⁸³⁾

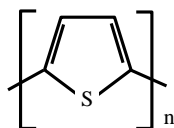


Figure 1.8 Chemical formula of PT.

PMeT can be readily prepared by either chemical or electrochemical methods. It is bright red in the oxidized state and light blue in the reduced state. In addition to this vivid color change, PMeT shows high coloration efficiency.¹⁶⁾ PEDOT, on the other hand, can be reversibly switched between sky blue in the oxidized state and deep blue in

the neutral state. PEDOT offers numerous additional advantages, and thus has been researched for many applications.²⁹⁾

1.5 Purpose of this study

EC materials for ECDs must exhibit 1) high coloration efficiency, 2) fast response time, 3) long cycle durability, 4) a variety of colors, 5) large transmittance change, and 6) cost-effectiveness for fabrication.

Cycle durability is very important for realizing practical ECDs. MHCFs and oxide materials have higher cycle durabilities than conventional organic EC materials. Therefore, in this study, MHCFs and oxides were investigated as EC materials for use in ECDs. Although FeHCF and WO_3 have been studied by numerous researchers, the other MHCFs and oxides have only been studied to a limited degree. Particularly, research on CE materials must be advanced to realize the practical application of ECDs. ZnHCF is considered to be a transparent CE for transmissive FeHCF ECDs, while CuHCF is considered for new colored EC electrodes. CoO_x is also considered to be a CE for oxide ECDs.

In addition to the EC materials themselves, the development of methods for their preparation and deposition as films is crucial for the fabrication ECDs. Fabrication techniques for ECDs must be effective over large areas, must be inexpensive, and must be appropriate for commercial-scale production. Possible methods that fit these criteria include the 1) ultracentrifuge separation method, 2) micro-mixer synthesis method, 3) chemical modification method, and 4) sputtering deposition method. The ultracentrifuge method can be used to separate NPs from powdery materials of different sizes, while the micro-mixer method can be used to rapidly synthesize homogenous MHCF-NPs and is appropriate for large-scale production. Chemical modification, meanwhile can be used to solubilize MHCF thin films, while sputtering is useful for the formation of homogenous large-area thin films.

In this study, the electrochemical and electrochromic properties of size-classified ZnHCF-NP thin films were investigated to improve the contrast and durability of ECDs. The electrochemical properties of CuHCF synthesized using a micro-mixer and the effects of chemical modification on CuHCF thin films were also investigated. Furthermore, the electrochromic properties of cobalt oxide and hydroxide films sputter-deposited in O_2 and H_2O atmospheres were studied.

References

- 1) Z. Jiao, J. L. Song, X. W. Sun, X. W. Liu, J. M. Wang, L. K., H. V. Demir: *Sol. Energy Mater. Sol. Cells* **98** (2012) 154.
- 2) C. Batista, R. M. Ribeiro, V. Teixeira: *Nanoscale Res. Lett.* **6** (2011) 301.
- 3) A. Zannotoa, R. Matassa, M. L. Saladino, M. Berrettoni, M. Giorgetti, S. Zamponi, E. Caponetti: *Mater. Chem. Phys.* **120** (2010) 118.
- 4) J. Z. Zhang, B. J. Schwartz, J. C. King, C. B. Harris: *J. Am. Chem. Soc.* **114** (1992) 10921.
- 5) S. Songara, M.K. Patra, M. Manoth, L. Saini, V. Gupta, G.S. Gowd, S.R. Vadera, N. Kumar: *J. Photochem. Photobiol. A: Chem.* **209** (2010) 68.
- 6) V. Wittwer, M. Datz, J. Ell, A. Georg, W. Graf, G. Walze: *Sol. Energy Mater. Sol. Cells* **84** (2004) 305.
- 7) V. Vitry, F. Renaux, R. Gouttebaron, J.-P. Dauchot, M. Hecq: *Thin Solid Films* **502** (2006) 265.
- 8) W.-L. Jang, Y.-M. Lu, Y.-R. Lu, C.-L. Chen, C.-L. Dong, W.-C. Chou, J.-L. Chen, T.-S. Chan, J.-F. Lee, C.-W. Pao, W.-S. Hwang: *Thin Solid Films* **544** (2013) 448.
- 9) S. Bao, Y. Yamada, K. Tajima, M. Okada, K. Yoshimura: *Vacuum* **83** (2009) 486.
- 10) K. Yoshimura, Y. Yamada, S. Bao, K. Tajima, M. Okada: *Sol. Energy Mater. Sol. Cells* **93** (2009) 2138.
- 11) T. S. Lee, H. Ahn, J. K. Lee, W. H. Park: *Optical Mater.* **21** (2002) 285.
- 12) J. Catalan: *Chem. Phys. Lett.* **457** (2008) 87.
- 13) L. V. Schueren, K. Hemelsoet, V. V. Speybroeck, K. D. Clerck: *Dyes. Pigm.* **94** (2012) 443.
- 14) L. Bu, Y. Li, J. Wang, M. Sun, M. Zheng, W. Liu, S. Xue, W. Yang: *Dyes. Pigm.* **99** (2013) 833.
- 15) J.-Y. Wang, C.-M. Yu, S.-C. Hwang, K.-C. Ho, L.-C. Chen: *Sol. Energy Mater. Sol. Cells* **92** (2008) 112.
- 16) S.-F. Hong, L.-C. Chen: *Electrochim. Acta* **55** (2010) 3966.

- 17) T.-H. Kuo, C.-Y. Hsu, K.-M. Lee, K.-C. Ho: Sol. Energy Mater. Sol. Cells **93** (2009) 1755.
- 18) J. Borratt and K. Dowd: Design Management Review **17** (2006) 24.
- 19) A.M. Soutar, D.R. Rosseinsky, W. Freeman, X. Zhang, X.X. How, H.J. Jiang, X.T. Zeng, X.G. Miao: Sol. Energy Mater. Sol. Cells **100** (2012) 268.
- 20) S. A. Agnihotry, P. Singh, A. G. Joshi, D. P. Singh, K. N. Sood, S. M. Shivaprasad: Electrochim. Acta **51** (2006) 4291.
- 21) D.-J. Yang, C.-Y. Hsu, C.-L. Lin, P.-Y. Chen, C.-W. Hu, R. Vittal, K.-C. Ho: Sol. Energy Mater. Sol. Cells **99** (2012) 129.
- 22) C. G. Granqvist: “*Handbook of Inorganic Electrochromic Materials*”, (Elsevier, Amsterdam, 1995) p. 10.
- 23) R. J. Mortimer, T. S. Varley: Sol. Energy Mater. Sol. Cells **109** (2013) 275.
- 24) P. R. Somani, S. Radhakrishnan: Mater. Chem. Phys. **77** (2002) 117.
- 25) L. Su, H. Wang, Z. Lu: Mater. Chem. Phys. **56** 266 (1998).
- 26) L.M.N. Assis, L. Ponez, A. Januszko, K. Grudzinski, A. Pawlicka: Electrochim. Acta **111** (2013) 299.
- 27) R. D. Rauh, S. F. Cogan: Solid State Ionics **28-30** (1988) 1707.
- 28) J-H. Ryu, J.-H. Lee, S.-J. Han, K.-D. Suh: Colloids and Surfaces A: Physicochem. Eng. Aspects **315** (2008) 31.
- 29) K.-C. Chen, C.-Y. Hsu, C.-W. Hu, K.-C. Ho: Sol. Energy Mater. Sol. Cells **95** (2011) 2238.
- 30) H. Kamioka, Y. Morimoto, W. Kosaka, S. Ohkoshi: J. Phys. Soc. Jpn. **77** (2008) 093710.
- 31) C.-F. Lin, C.-Y. Hsu, H.-C. Lo, C.-L. Lin, L.-C. Chen, K.-C. Ho: Sol. Energy Mater. Sol. Cells **95** (2011) 3074.
- 32) J. Chen, K. Huang, S. Liu: Electrochem. Commu. **10** (2008) 1851.
- 33) S. Hara, H. Shiozaki, A. Omura, H. Tanaka, T. Kawamoto, M. Tokumoto, M. Yamada, A. Gotoh, M. Kurihara, M. Sakamoto: Appl. Phys. Express, **1** (2008) 104002.
- 34) S.-F. Hong, L.-C. Chen: Sol. Energy Mater. Sol. Cells **104** (2012) 64.
- 35) M. Ishizaki, M. Sakamoto, H. Tanaka, T. Kawamoto, M. Kurihara: Mol. Cryst.

- Liquid Cryst. **539** (2011) 18.
- 36) S. Pahal, M. Deepa, S. Bhandari, K.N. Sood, A.K. Srivastava: Sol. Energy Mater. Sol. Cells **94** (2010) 1064.
 - 37) J.-Y. Wang, C.-M. Yu, S.-C. Hwang, K.-C. Ho, L.-C. Chen: Sol. Energy Mater. Sol. Cells **92** (2008) 112.
 - 38) V.D. Neff, J. Electrochem. Soc. **125** (1978) 886.
 - 39) Z. Jiao, J. L. Song, X. W. Sun, X. W. Liu, J. M. Wang, L. Ke, H. V. Demir: Sol. Energy Mater. Sol. Cells **98** (2012) 154.
 - 40) Y. Rong, S. Kim, F. Su, D. Myers, M. Taya: Electrochim. Acta **56** (2011) 6230.
 - 41) P. J. Kulesza, M. A. Malik, R. Schmidt, A. Smolinska., K. Miecznikowski, S. Zamponi, A. Czerwinski, M. Berrettoni, R. Marassi: J. Electroanal. Chem. **487** (2000) 57.
 - 42) N. R. Tacconi, K. Rajeshwar, R. O. Lezna: Electrochim. Acta **45** (2000) 3403.
 - 43) J. R.-Hernandez, E. Reguera, E. Lima, J. Balmaseda, R. M.-Garcia, H. Y.-Madeira: J. Phys. Chem. Solids **68** (2007) 1630.
 - 44) O. Makowski, J. Stroka, P. J. Kulesza, M. A. Malik, Z. Galus: J. Electroanal. Chem. **532** (2002) 157.
 - 45) J. Balmaseda, E. Reguera, J. Rodríguez-Hernández, L. Reguera, M. Autie: Micropor. Mesopor. Mater. **96** (2006) 222.
 - 46) M. Avila, L. Reguera, J. Rodríguez-Hernández, J. Balmaseda, E. Reguera: J. Solid Chem. **181** (2008) 2899.
 - 47) C.P. Krap, J. Balmaseda, B. Zamora, E. Reguera: Int. J. Hydrogen Energy **35** (2010) 10381.
 - 48) S. Ayrault, B. Jimenez, E. Garnier, M. Fedorff, D. J. Jones, C. Loos-Neskovic: J. Solid State Chem. **141** (1998) 475.
 - 49) C. Loos-Neskovic, S. Ayrault, V. Badillo, B. Jimenez, E. Garnier, M. Fedorff, D. J. Jones, B. Merinov: J. Solid State Chem. **177** (2004) 1817.
 - 50) R. Chen, H. Tanaka, T. Kawamoto, M. Asai, C. Fukushima, M. Kurihara, M. Watanabe, M. Arisaka, T. Nankawa: Electrochem. Commu. **25** (2012) 23.
 - 51) R. Chen, H. Tanaka, T. Kawamoto, M. Asai, C. Fukushima, H. Na, M. Kurihara, M. Watanabe, M. Arisaka, T. Nankawa: Electrochim. Acta **87** (2013) 119.

- 52) R. Garjonyte, A. Malinauskas: *Sens. Actuators B* **56** (1999) 93.
- 53) L. Guadagnini, D. Tonelli, M. Giorgetti: *Electrochim. Acta* **55** (2010) 5036.
- 54) T.-H. Tsai, T.-W. Chen, S.-M. Chen: *Int. J. Electrochem. Sci.* **6** (2011) 4628.
- 55) C. D. Wessells, R. A. Huggins, Y. Cui: *Nature Commu.* **2** (2011) 520.
- 56) A. Gotoh, H. Uchida, M. Ishizaki, T. Satoh, S. Kaga, S. Okamoto, M. Ohta, M. Sakamoto, T. Kawamoto, H. Tanaka, M. Tokumoto, S. Hara, H. Shiozaki, M. Yamada, M. Miyake, M. Kurihara: *Nanotechnology* **18** (2007) 345609.
- 57) H. Shiozaki, T. Kawamoto, H. Tanaka, S. Hara, M. Tokumoto, A. Gotoh, T. Satoh, M. Ishizaki, M. Kurihara, M. Sakamoto: *Jpn. J. Appl. Phys.* **47** (2008) 1242.
- 58) M. Ishizaki, K Kanaizuka, M. Abe, Y. Hoshi, M. Sakamoto, T. Kawamoto, H. Tanaka, M. Kurihara: *Green Chem.* **14** (2012) 1537.
- 59) S. Hara, H. Tanaka, T. Kawamoto, M. Tokumoto, M. Yamada, A. Gotoh, H. Uchida, M. Kurihara, M. Sakamoto: *Jpn. J. Appl. Phys.* **46** (2007) L945.
- 60) M. Ishizaki, Y. Sajima, S. Tsuruta, A. Gotoh, M. Sakamoto, T. Kawamoto, H. Tanaka, M. Kurihara: *Chem. Lett.* **38** (2009) 1058.
- 61) M. Ishizaki, A. Gotoh, M. Abe, M. Sakamoto, H. Tanaka, T. Kawamoto, M. Kurihara: *Chem. Lett.* **39** (2010) 762.
- 62) N. Ozer, C. M. Lampert: *Sol. Energy Mater. Sol. Cells* **54** (1998) 147.
- 63) J.L. He, M.C. Chiu: *Surf. Coat. Technol.* **127** (2000) 43.
- 64) S.S. Mahajan, S.H. Mujawar, P.S. Shinde, A.I. Inamdar, P.S. Patil: *Int. J. Electrochem. Sci.* **3** (2008) 953.
- 65) S.-Y. Lin, C.-M. Wang, K.-S. Kao, Y.-C. Chen, C.-C. Liu: *J. Sol-Gel Sci. Technol.* **53** (2010) 51.
- 66) N. Sakai, Y. Ebina, K. Takada, T. Sasaki: *J. Electrochem. Soc.* **152** (2005) E384.
- 67) Y. Jung, J. Lee, Y. Tak: *Electrochem. Solid-State Lett.* **7** (2004) H5.
- 68) S. Gottesfeld: *J. Electrochem. Soc.* **127** (1980) 272.
- 69) I. Porqueras, E. Bertran: *Thin Solid Films* **41-44** (2001) 398.
- 70) I. Bouessay, A. Rougier, P. Poizota, J. Moscovici, A. Michalowicz, J.-M. Tarascon: *Electrochim. Acta* **50** (2005) 3737.
- 71) Y. Abe, H. Ueta, T. Obata, M. Kawamura, K. Sasaki, H. Itoh: *Jpn. J. Appl. Phys.*

- 49** (2010) 115802.
- 72) H. Ueta, Y. Abe, K. Kato, M. Kawamura, K. Sasaki, H. Itoh: Jpn. J. Appl. Phys. **48** (2009) 015501.
- 73) C. M. Lampert and C.G. Granqvist, *Large Area Chromogenics: Materials and Devices for Transmittance Control; Chemical and Optical Studies of Electrochromic Hydrated Nickel Oxide Films and Devices* (Optical Engineering Press, Bellingham WA) (1989).
- 74) P. M. S. Monk, N. Farooq: J. Mater. Sci.-Mater. Electron. **6** (1995) 389.
- 75) N. Bahlawane, E. F. Rivera, K. K.-Höinghaus, A. Brechling, U. Kleineberg: Appl. Catal. B-Environ. **53** (2004) 245.
- 76) L. Tian, J. Bian, B. Wang, Y. Qi: Electrochim. Acta **55** (2010) 3083.
- 77) Y. F. Yuan, X. H. Xia, J. B. Wu, J. S. Gui, Y. B. Chen, S. Y. Guo: J. Membrane Sci. **364** (2010) 298.
- 78) L. B. Kong, M. C. Liu, J. W. Lang, M. Liu, Y. C. Luo, L. Kang: J. Solid State Electrochem. **15** (2011) 571.
- 79) W. J. Zhou, M. W. Xu, D. D. Zhao, C. L. Xu, H. L. Li: Micropor. Mesopor. Mater. **117** (2009) 55.
- 80) H.-K. Kim, T.-Y. Seong, J.-H. Lim, W. I. Cho, Y. S. Yoon: J. Power Sources **102** (2001) 167.
- 81) L. Michaelis, E. S. Hill: J. Gen. Physiol. **16** (1933) 859.
- 82) C.-W. Hu, K.-M. Lee, R. Vittal, D.-J. Yang, K.-C. Ho: J. Electrochem. Soc. **157** (2010) 75.
- 83) P. R. Somani, S. Radhakrishnan: Mater. Chem. Phys. **77** (2002) 117.

Chapter 2 Experimental method

2.1 Film deposition

2.1.1 Spin coating method

Spin coating has been used for several decades for the preparation of thin films. A typical process involves the deposition of a small puddle of a liquid solution onto the center of a substrate followed by the spinning of the substrate at high speed. Centripetal acceleration causes the liquid solution to spread to the edge of the substrate leaving a thin film of the liquid solution on the entire surface (Figure 2.1).

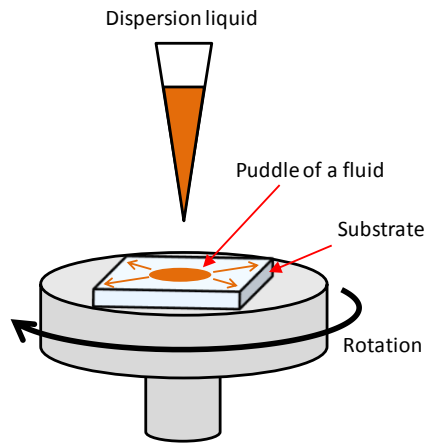


Figure 2.1 Schematic of the spin coating method.

The final film thickness depends on the nature of the liquid solution (viscosity, drying rate, percent solids, surface tension, among others); the final rotational speed, acceleration, and atmosphere contribute to the properties of the coated film. It is therefore necessary to choose the optimum parameters for the spin process to obtain high-quality thin films.

The film thickness h (m) is determined from the film thickness h_0 and viscosity η (Pa) of the liquid solution and the process parameters, including the angular velocity (spin speed) ω (s^{-1}), and spin time t (s):¹⁻³⁾

$$h = \frac{h_0}{\left(1 + \frac{4\omega^2 h_0^2 t}{3\eta}\right)^{\frac{1}{2}}} \quad (2.1)$$

2.1.2 Reactive RF magnetron sputtering

Thin films of metal oxides (e.g. WO_3 , NiO_x , CoO_x , and Nb_2O_5) have been mostly prepared by dry processes such as vacuum evaporation and sputtering.⁴⁻⁷⁾ Sputtering is a physical vapor deposition technique. In the basic sputtering process, the source material (target) is bombarded by energetic positive ions generated in a glow discharge plasma situated in front of the target.⁸⁾ The positively charged gas ions from the plasma are attracted and accelerated toward the target by an electric field obtained by applying a negative potential to the target with respect to the substrate electrode. Thus, the source electrode for the target is known as the cathode, and the substrate electrode is the anode.⁸⁾

The sputtered atoms from the target then condense in a thin film on the desired substrate. (Figure 2.2 (a)) For the deposition of insulating films, radio frequency (RF) sputtering is preferred, because it avoids the positive charging of the target; an alternating potential rather than DC is applied (AC power supply frequency 13.56 kHz).⁹⁾ For the deposition of metal films, an inert sputtering gas (e.g. Ar) is used, and a reactive component (e.g., O_2 or H_2O) is introduced as a process gas to deposit compound thin films. Reactive magnetron sputtering occurs whenever the chemical composition of the deposited coating substantially differs from the composition of the sputtering targets.

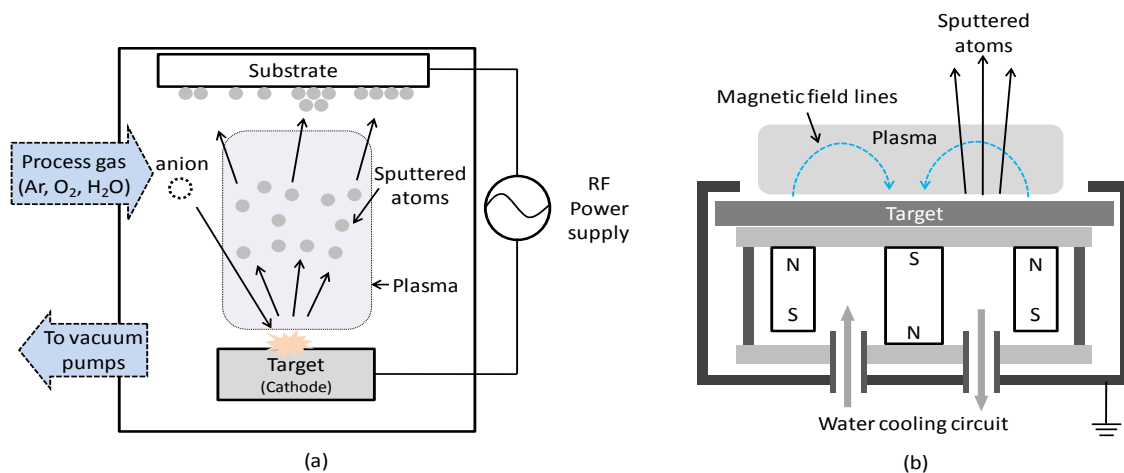


Figure 2.2 Details of the (a) RF sputter deposition process and (b) magnetic structure of a magnetron sputter gun⁹⁾.

Magnetron sputtering is used to increase the deposition rate. The magnets are mounted outside the vacuum environment, as shown in Figure 2.2 (b). The plasma is trapped by a combination of electric and magnetic field confinement based on the magnetron principle.

2.2. Particle-size classification

In general, a wide distribution of particle sizes is obtained for the as-synthesized particles. Therefore, it is necessary to use a particle-size classification technique to obtain uniform-sized particles. Centrifugation is a useful method for precise classification.¹⁰⁾ Figure 2.3 shows the centrifugal process for general colloidal liquid. Protocols for centrifugation typically specify the level of acceleration to be applied to the sample, rather than the rotational speed, such as revolutions per minute (rpm). The acceleration is often quoted in multiples of g , the acceleration due to gravity at the Earth's surface. This distinction is important because two rotors with different diameters running at the same rotational speed will subject samples to different accelerations.

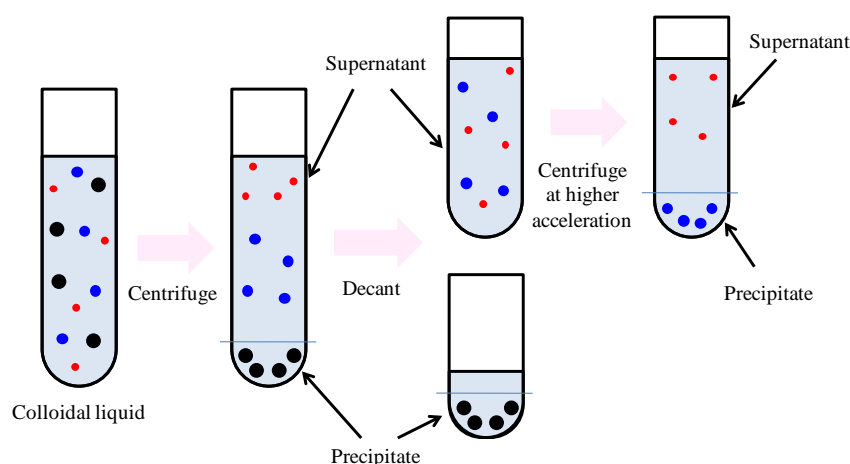


Figure 2.3 Centrifugal process for general colloidal liquids.

The acceleration can be calculated as the product of the radius r and the square of the angular velocity ω . The relative centrifugal force is a measurement of the force applied to a sample within a centrifuge; it can be calculated by the following equation:¹¹⁾

$$\text{RCF} = \frac{r\omega^2}{g}. \quad (2.2)$$

This relationship may be rewritten as follows:

$$\text{RCF} = 1.118 \cdot 10^{-5} \cdot r \cdot N^2, \quad (2.3)$$

where N is the rotational speed.

2.3 Film thickness and surface and cross-sectional morphologies

2.3.1 Field emission scanning electron microscopy

The scanning electron microscope (SEM) is one of the most versatile instruments available for the analysis of the microstructure, morphology, thickness, and chemical composition of materials.

Field emission SEM (FE-SEM) relies on the generation and liberation of electrons from a field emission source for image formation. In contrast to conventional SEM (thermal electron emission type), in which a tungsten filament is heated to produce a stream of electrons, the field emission source is a thin, sharp, single crystal tungsten wire that remains at ambient temperature. Electrons are thought to originate from a point source on the filament, which may be less than 5 nm in diameter; they are drawn by an electrical field. This extremely fine source for the field emission system allows the attainment of higher resolution. The field emission gun acts as a cathode in front of first and second anodes. A potential difference (extraction voltage of 3 ~ 6 kV) is applied between the first anode and the tip; this difference generates an electric field concentrated at the tip, resulting in the emission of electron. The emitted electrons pass through the first anode and are accelerated by the second anode voltage (V_o), or accelerating voltage, of the gun, which is determined by the potential difference between the tip and the second grounded anode (electron extraction voltage),¹²⁾ as shown in Figure 2.4 (a).

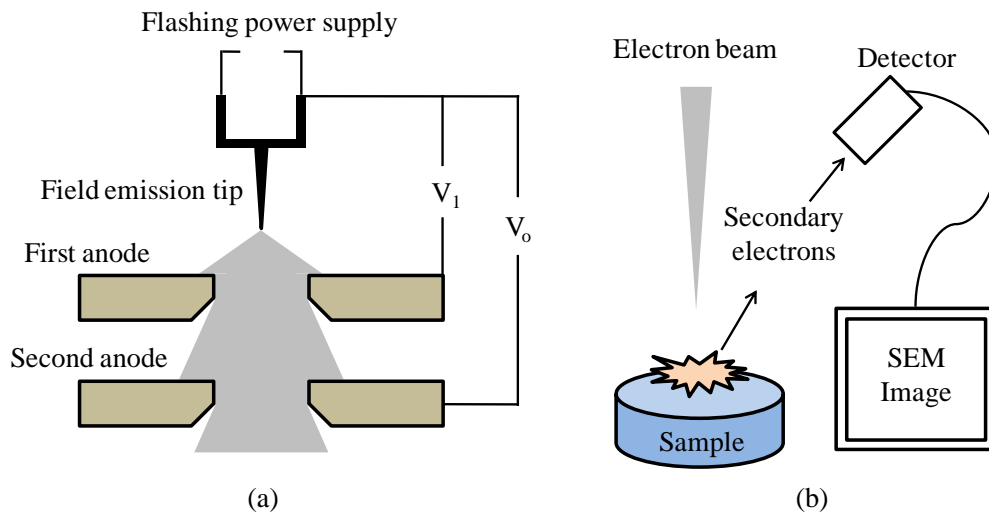


Figure 2.4 Schematic presentation of (a) a field emission gun and (b) the measurement principles for the scanning electron microscope.

The higher the accelerating voltage, the faster the electrons travel down the column, resulting in a more penetrating beam. These primary electrons are focused and deflected by electron magnetic coils (lenses) to produce a narrow electron probing beam that scans the object or specimen. The electrons are accelerated in a strong electrical field within a high vacuum column (10^{-9} to 10^{-10} Torr). This ultra-high vacuum acts to stabilize the emission of electrons and prevent the contamination of the filament tip. Subsequently, secondary electrons are produced as a result of interactions with the atoms at the sample surface. These electrons are detected by a system in the microscope column composed of a collector, scintillator, and photomultiplier tube. The photoelectrons generated by the photomultiplier are then converted into an electronic signal, which is further amplified and digitized. The end result is a detailed image of the topography of the specimen surface that can then be displayed,¹²⁾ as shown in Figure 2.4 (b).

The brightness on the screen is proportional to the number of secondary electrons emitted from the specimen. It is also necessary to ensure that the tip of the tungsten wire remains free of contaminants and oxides. Therefore, it is necessary to periodically heat or flash the tip (voltage is applied momentarily to the tip) to remove any free absorbed gas molecules, often resulting in reversible, momentary instability of the beam. However, the failure to flash the tip results in the observer visualizing white flashes or

“hot spots”. Compared to the diameter of the probing electron beam in conventional SEM, that in FESEM (the beam current per unit area per solid angle) is smaller given the very small source size as it travels down the column, which results in more intense brightness (brightness linearly increases with accelerating voltage), greater spatial resolution capabilities (1.5 nm; three to six times better than that of conventional SEM), reduced in chromatic aberration, improved depth of field, and enhancement of surface details at high magnifications (at low voltages, fine features are more easily observed). A resolution of 0.5 nm has been achieved under ideal conditions, and 5 nm is regularly achieved at an acceleration voltage of 30 kV with conducting materials.¹³⁾

In addition, the field emission scanning electron microscope operates at lower accelerating voltages (0.5 to 30 kV), resulting in high-quality images that have less electrostatic distortion and increased image contrast. The main benefit of using a lower accelerating voltage when observing high-magnification views of specimens is reduced beam penetration into the specimen, which can obscure surface details, and a reduced likelihood of charging and damage to uncoated, nonconductive, and beam-sensitive samples.^{12,14)}

2.3.2 Multi-beam interferometry

A thin film is a layer of material sub-nanometer to micron thickness. Multi-beam interferometry is a method used to estimate film thickness *via* optical interference.

When light strikes the film surface, it is either transmitted or reflected at the upper surface. The light that is transmitted reaches the bottom surface and may once again be transmitted or reflected. The Fresnel equation provides a quantitative description of how much light will be transmitted or reflected at an interface. In addition, the light reflected from the upper and lower surfaces will interfere, and the degree of constructive or destructive interference is dependent on the difference in their phases. This difference is in turn dependent on the thickness of the film layer, the refractive index of the film, and the angle of incidence of the original wave with respect to the film.¹⁵⁾

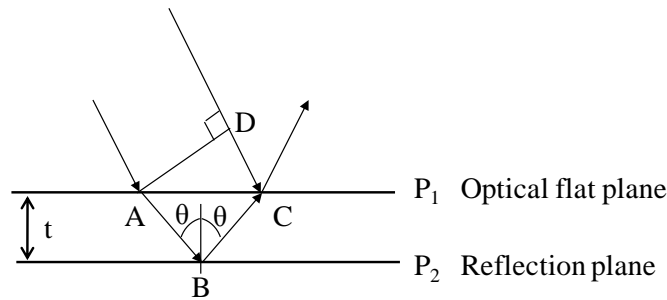


Figure 2.5 Conceptual diagram of light reflection and transmission for parallel planes.

The optical path difference Δd for the light reflected by both upper and lower boundaries must be calculated to determine the conditions for interference. When parallel light is incident to the reflection planes P_1 and P_2 , Δd is calculated by the following equation:

$$\Delta d = \overline{AB} + \overline{BC} - \overline{CD}. \quad (2.4)$$

Maximum reflections are obtained when

$$m\lambda = \Delta d, \quad (2.5)$$

and minimum reflections are obtained when

$$m \left(\lambda + \frac{1}{2} \right) = \Delta d, \quad (2.6)$$

where m is an integer and λ is the wavelength of the incident light.

In multi-beam interferometry, $\theta = 0$; that is the incident light is vertical, as shown in Figure 2.6.

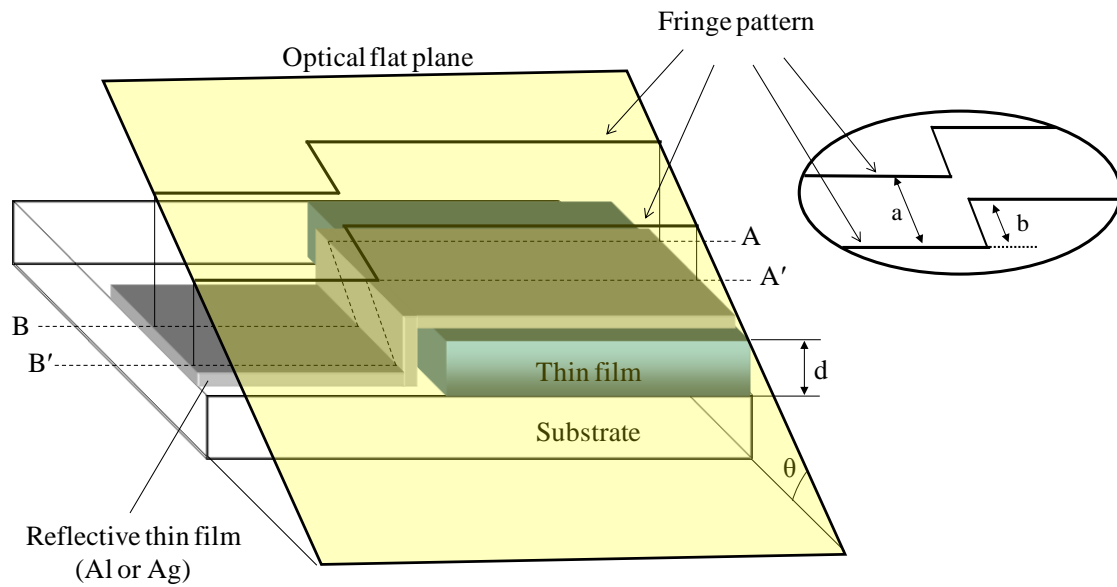


Figure 2.6 Fringe pattern obtained in multi-beam interferometry.¹⁶⁾

If an optical flat is placed on a thin film sample, as shown in Figure 2.6, a fringe pattern is obtained. From the distance between two adjacent fringes a and the difference in fringes b , the film thickness d can be calculated by the following equation:

$$d = \frac{b}{a} \cdot \frac{\lambda}{2}. \quad (2.7)$$

2.4. Plasma state

The plasma state during sputtering can be characterized by plasma emission spectroscopy, which is a diagnostic tool that provides *in situ* information about the deposition process and can be performed without disturbing film deposition conditions.¹⁷⁾

In plasmas, a process gas molecules and atoms are typically excited by high-energy electrons. The gas molecules and atoms absorb energy through collisions with the electrons and are excited from their ground states. After a short lifetime, the excited molecules and atoms return to their corresponding ground states, which simultaneously results in the emission of electromagnetic radiation, generally in the form of light in the UV visible region. The emitted radiation is analyzed using a spectrograph, which separates the various wavelengths.

The intensity of each peak in the spectrum is directly proportional to the concentration of the corresponding element in the gas. Therefore, plasma emission spectroscopy is a method for analyzing various elements in the plasma.

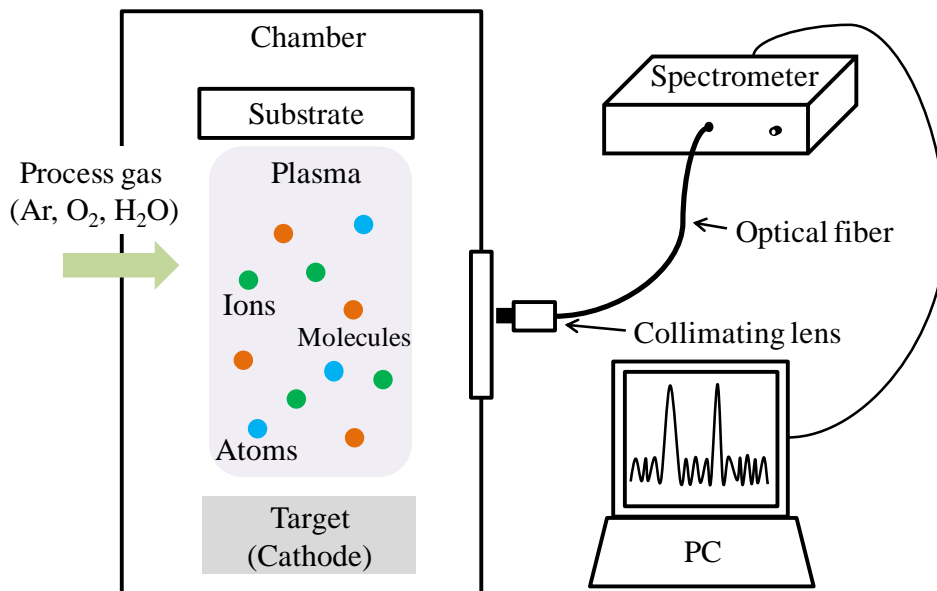


Figure 2.7 Schematic diagram of plasma emission spectroscopy.

2.5 Crystal structure

X-ray diffraction (XRD) analysis is a very powerful and suitable technique for characterizing the microstructure of thin films. It is nondestructive, noncontact, and provides useful information, such as the presence and composition of different phases, film thickness, grain size, and orientation and strain state.

X-rays are electromagnetic radiation similar to light, but with a much shorter wavelength. They are produced when electrically charged particles of sufficient energy are decelerated. Figure 2.8 presents the schematics of an X-ray diffractometer. In an X-ray tube, the high voltage maintained across the electrodes draws electrons toward a metal target (the anode). X-rays are produced at the point of impact, and radiate in all directions. Tubes with copper targets produce their strongest characteristic radiation at a wavelength of approximately 1.54 Å.

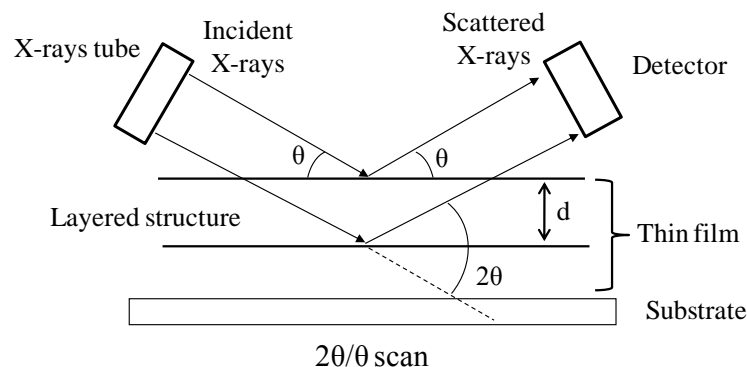


Figure 2.8 Incident X-Rays are diffracted by the layers of atoms in a crystalline material.

The relationship by which diffraction occurs is known as Bragg's law, which is given by equation 2.8:¹⁸⁾

$$n\lambda = 2d \sin\theta, \quad (2.8)$$

where d is the interplanar spacing, θ is the diffraction angle, λ is the wavelength of the x-rays, and n is order of diffraction. Because every crystalline material has a characteristic atomic structure, each diffracts X-rays in a unique and characteristic pattern.

2.6 Film density

X-ray reflectivity (XRR) is a powerful, nondestructive tool for investigating the thickness, surface roughness and film density of thin film.¹⁹⁻²⁰⁾

When the incident angle is small ($0 \sim 2$ degrees), the X-ray beam is totally reflected. The XRR technique requires the alignment of the incident and reflected angles θ with an error less than ± 0.005 degrees.²⁰⁾ Above the critical angle of total reflectance, the beam penetrates the sample and is refracted. (Figure 2.9)

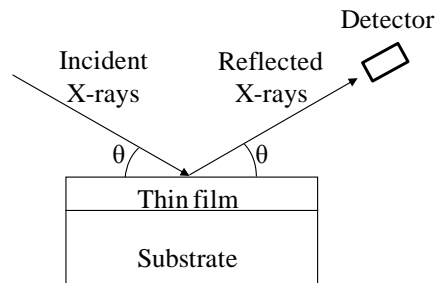


Figure 2.9 X-ray reflection in thin films at low incidence angle θ ($0 \sim 2^\circ$).

The slope of the spectrum and the decay rate of the oscillations provide information on surface roughness, as shown in Figure 2.10. In addition, the density and thickness of thin films can be calculated from the critical angle and oscillation period of the spectrum, respectively.²⁰⁻²¹⁾

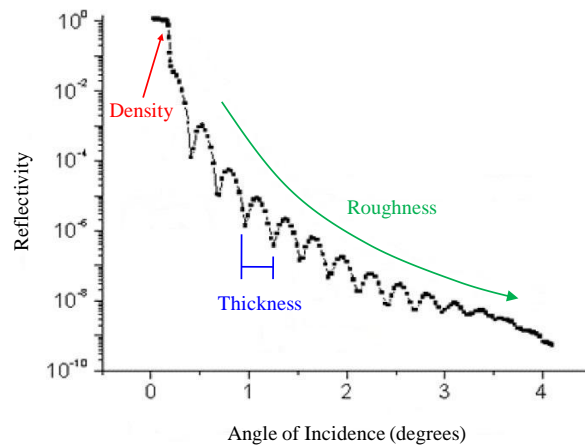


Figure 2.10 Analysis of the X-ray reflectivity spectrum.

2.7 Chemical bonding state

Infrared (IR) spectroscopy involves the measurement of the absorption of different IR frequencies by a sample positioned in the path of an IR beam. The main goal of IR spectroscopic analysis is to determine the chemical functional groups in the sample. Different functional groups absorb characteristic frequencies of IR radiation.²²⁾

A molecule can be excited to a higher vibrational state by absorbing IR radiation. The probability of a particular IR frequency being absorbed depends on the actual interaction between this frequency and the molecule. In general, a frequency will be strongly absorbed if its photon energy coincides with the vibrational energy levels of the molecule. While the absorption frequency depends on the vibrational frequency of the molecules, the absorption intensity depends on how effectively the infrared photon energy can be transferred to the molecule, which in turn depends on the change in the dipole moment that occurs as a result of molecular vibration.²³⁾

The IR region is divided into three sections: near, mid, and far. The mid IR region (4000 ~ 400 cm^{-1} or wavenumbers) is of the greatest practical use for IR spectroscopy. An increase in wavenumber corresponds to an increase in energy.²⁴⁾ In IR spectroscopy, infrared radiation is absorbed by molecules and converted into molecular vibrational energy (stretching and bending) when the radiant energy matches the energy of a specific molecular vibration. The absorption of radiant energy is represented by the absorbance A , which is calculated as the logarithm, to the base 10, of the reciprocal of the transmittance T .²²⁾

$$A = \log_{10}(1/T). \quad (2.9)$$

The wavenumbers (also referred to as frequencies) at which a molecule absorbs radiation indicate the functional groups that are present in the molecule. Certain groups of atoms absorb energy and give rise to bands at approximately the same frequencies, regardless of the molecule. The analysis of an IR spectrum is thus possible with the help of tables that correlate frequencies to functional groups.

Fourier transform infrared (FTIR) spectroscopy has long been utilized as an analytical technique for qualitatively determining the presence of various chemical bonds in gases, liquids, solids, and on surfaces²⁵⁾ because it is a rapid, economical, easy, and non-destructive technique.²⁶⁾ In FTIR spectroscopy an interferogram of the sample signal is collected using an interferometer and then a Fourier transform of the interferogram is performed to obtain the spectrum (Figure 2.11).

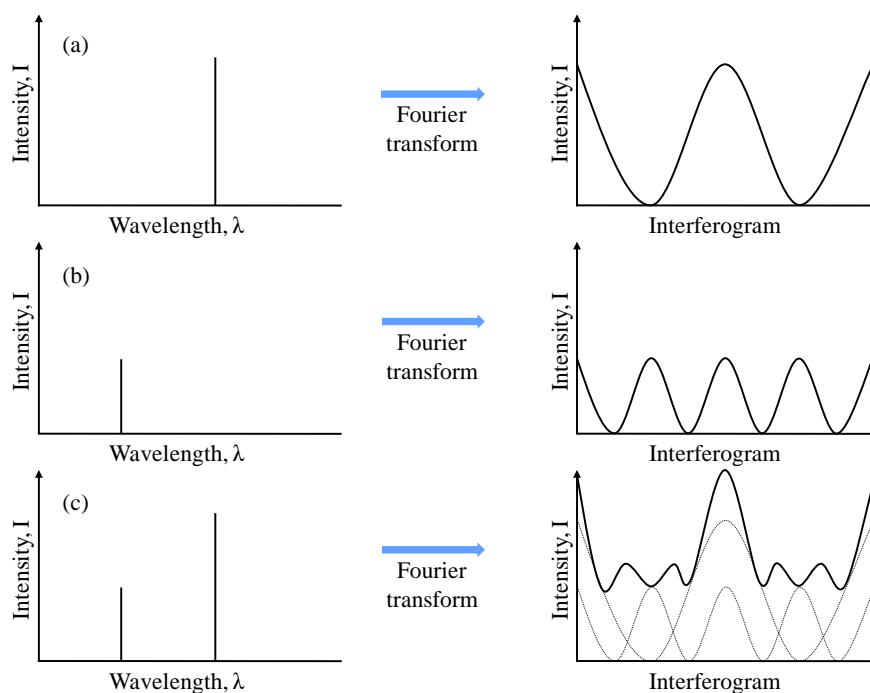


Figure 2.11 (a) He-Ne laser line through an interferometer and (b) He-Ne laser line with $1/2$ the intensity and $\lambda/2$ passed through an interferometer, (c) both λ and $\lambda/2$ line sources passed through an interferometer.

2.8 Particle size and colloidal stability

2.8.1 Dynamic light scattering

Dynamic light scattering (DLS) is an important tool for characterizing the size of NPs in a solution. DLS measures the light scattered from a laser that passes through a colloidal solution, and by analyzing the modulation of the scattered light intensity as a function of time, the hydrodynamic size of the particles and particle agglomerates can be determined. DLS measures Brownian motion, which is the random movement of particles due to the bombardment of surrounding solvent molecules, and relates this behavior to the size of the particles. Typically, DLS is used to analyze particles suspended within a liquid, and the larger the particle, the slower the Brownian motion, because smaller particles are moved further and with greater speed by the solvent molecules (Figure 2.12).

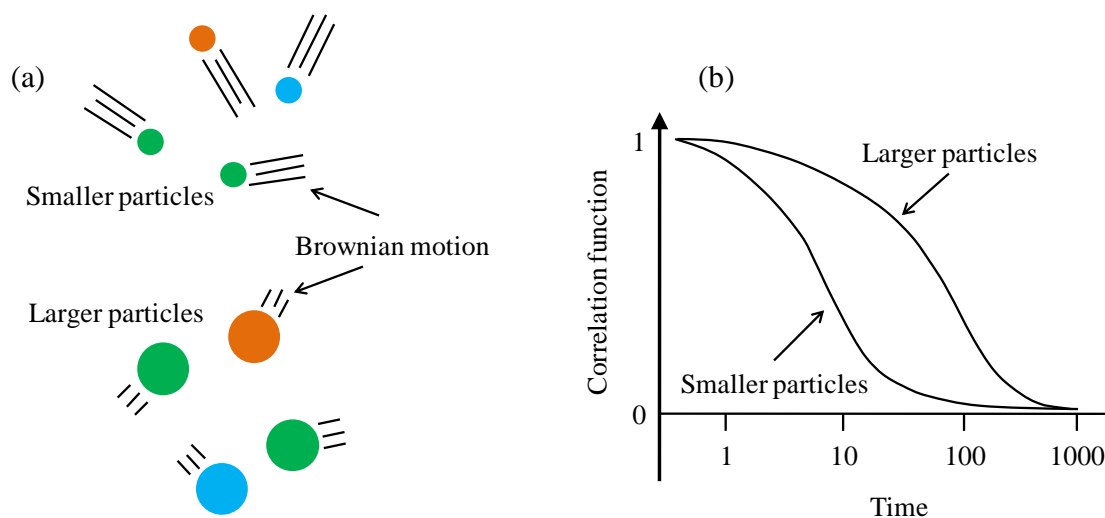


Figure 2.12 (a) Schematic representation of Brownian motion and (b) the relationship of the correlation function with time.

An accurately known temperature is necessary for DLS, because the knowledge of viscosity is required. The temperature must also be stable, otherwise, convection currents in the sample will cause nonrandom movements that will lead to errors in data interpretation. The velocity of the Brownian motion is defined by the property known as

the translational diffusion coefficient D . The size of a particle is calculated from D using the Stokes-Einstein equation:²⁷⁾

$$d(H) = \frac{kT}{3\pi\eta D}, \quad (2.10)$$

where $d(H)$ is the hydrodynamic diameter of the particles, D is the translational diffusion coefficient, k is Boltzmann's constant, T is the absolute temperature, and η is the viscosity of the solvent.

2.8.2 Zeta potential

Electrokinetic techniques are the most widely used experimental methods for studying charged surfaces. The electrical potential at the slipping plane is defined as the electrokinetic potential, or more commonly the zeta potential (ζ).²⁸⁾ The zeta potential can be deduced from electrokinetic measurements, and in addition to being experimentally accessible, correlates with particle stability. Highly stable colloidal systems are characterized by high zeta potentials, whereas low zeta potentials indicate less stable systems (see Table 2.1).²⁹⁾

Table 2.1 Colloidal stability of particles and their zeta potentials³⁰⁻³¹⁾

Zeta potential (mV)	Colloidal stability
0 to ± 5 ,	Rapid coagulation or flocculation
± 10 to ± 30	Incipient instability
± 30 to ± 40	Moderate stability
± 40 to ± 60	Good stability
more than ± 61	Excellent stability

In the case of ZrO_2 particles, the formation of soft agglomerates in suspension is observed to occur when the absolute value of the zeta potential is less than ~ 30 mV, which is commonly observed in many oxide suspensions.³⁰⁾

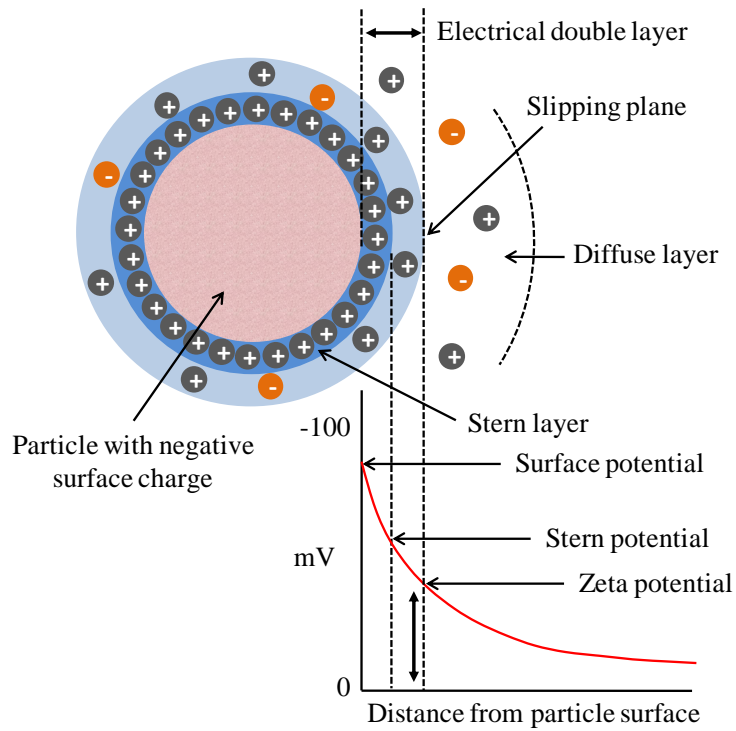


Figure 2.13 Two methods for visualizing the double layer. The left view shows the change in charge density around a colloid. The right shows the distribution of positive and negative ions around a charged colloid.

NPs have a surface charge that attracts a thin layer of ions of the opposite charge to the NP surface. This double layer of ions travels with the NP as it diffuses throughout the solution, as shown in Figure 2.13. The zeta potential of particles typically falls in the range from +100 mV to -100 mV. Dispersions with a low zeta potential eventually aggregate because of Van der Waals inter particle attractions.

2.9 Chemical composition

The chemical composition of the MHCF samples was measured by atomic emission spectroscopy (AES), which involves the quantitative analysis of the optical emission from excited atoms for the determination of analyte concentrations. Analyte atoms in solution are aspirated into the excitation region where they are desolvated, vaporized, and atomized by a flame, discharge, or plasma. These high-temperature atomization sources provide sufficient energy to promote the atoms to high energy levels. The atoms then decay back to lower levels by emitting light (see Figure 2.14 (a)). Because the transitions are between distinct atomic energy levels, the emission lines in the spectrum are narrow. However, the spectra of multi-elemental samples can be very congested, and the spectral separation of nearby atomic transitions requires a high-resolution spectrometer.

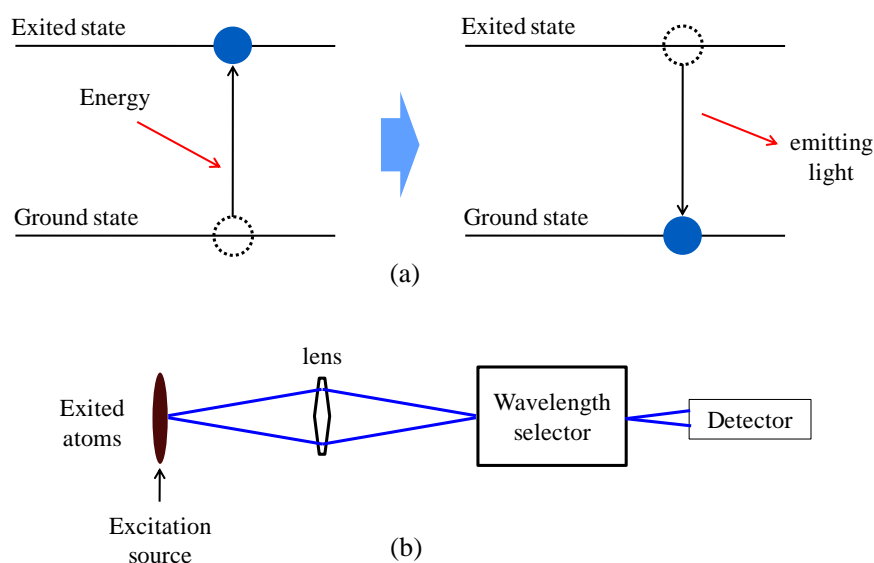


Figure 2.14 Schematic diagram of (a) atomic emission and (b) an AES experiment.

AES has a high throughput with the capacity for multi-element monitoring. For emission spectroscopy systems, various excitation sources have been used to produce excited atoms that emit light for elemental analysis. Emission sources include flames, electrical arcs/sparks, and plasma instruments (Figure 2.14 (b)). In particular, plasma-based systems in which a microwave-induced plasma is produced *via* various mechanisms have been widely used.³²⁾

2.10 Electrochemical and electrochromic properties

2.10.1 Electrochemical measurements

Electrochemical, parameters such as reversibility, ion storage capacity, and cycle stability can be determined from cyclic voltammetry (CV), chronocoulometry (CC) and chronoamperometry (CA) experiments using a WE, a reference electrode (RE), and a CE, and the application of a potential (V) or current (I) as shown in Figure 2.15.

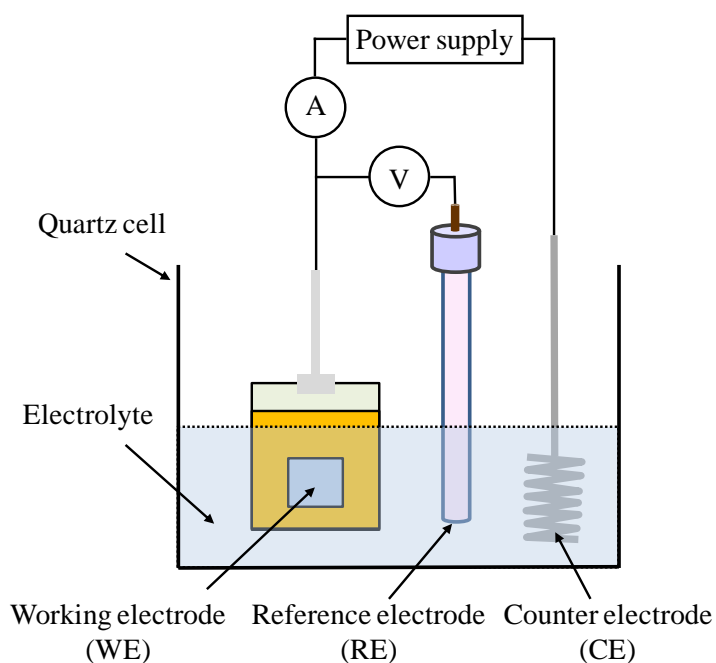


Figure 2.15 Schematic diagram of a three electrode cell.

1) Cyclic voltammetry

In linear sweep voltammetry (LSV), a fixed potential range is employed, similar to that used in potential step measurements. However, in LSV, the voltage is scanned from a lower limit to an upper limit, as shown in Figure 2.16 (a). The voltage scan rate (v) is calculated from the slope of the line. Clearly, by changing the time taken to sweep the range. The characteristics of a recorded linear sweep voltammogram depend on a number of factors:

- (i) rate of the electron transfer reaction,
- (ii) chemical reactivity of the electroactive species,
- (iii) voltage scan rate.

CV is very similar to LSV. In this case the voltage is swept between two values (V_1 and V_2 , see Figure 2.16 (b)) at a fixed rate, and when the voltage reaches V_2 , the scan is reversed, and the voltage is swept back to V_1 . A typical cyclic voltammogram recorded for a reversible single-electrode transfer reaction is shown in Figure 2.16 (c).³³⁾

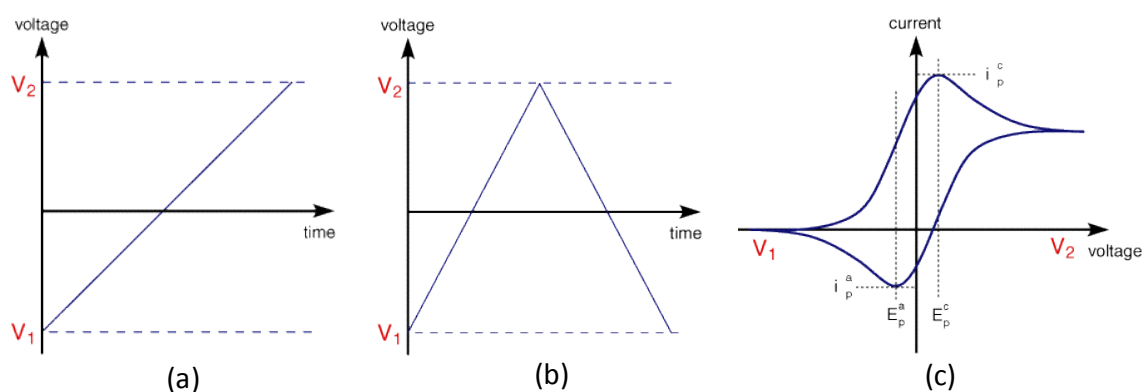


Figure 2.16 Potential changes for (a) linear sweep voltammetry and (b) cyclic voltammetry, and (c) a cyclic voltammogram.

The forward sweep produces a response identical to that observed for the LSV experiment. When the scan is reversed, we simply move back through the equilibrium positions gradually converting the electrolysis product. The current flow is now from the solution species back to the electrode, thus occurring in a sense opposite to that during the forward sweep, but otherwise, the behavior can be explained in an identical manner. For reversible electrochemical reactions, the CV has certain well-defined characteristics.

2) Chronocoulometry

CC is a the classical electrochemical technique frequently used in electroanalytical chemistry. As its name implies, it is the measurement of charge (coulombs) as a function of time (chrono). Applications of this technique include the determination of the surface area of electrodes, diffusion coefficients, concentration, kinetics of both heterogeneous electron transfer reactions and chemical reactions coupled to electron transfer, adsorption, and the effective time window for an electrochemical cell. A potential step experiment can also be used to record the charge versus time dependence. The analysis of CC data is based on the Anson equation, which defines the charge-time dependence for linear diffusion control:³⁴⁾

$$Q(t) = 2nFACD^{\frac{1}{2}}\pi^{\frac{1}{2}}t^{\frac{1}{2}}, \quad (2.11)$$

where, Q represents the charge, n is the number of electrons transferred, A is the real electrochemical surface area of the electrode, F is Faraday's constant (96,485 C/mole), C is the concentration of the mediator, D is the diffusion coefficient of the mediator, and t is time. There is a linear relationship between the charge Q and the square root of time ($t^{1/2}$).

Given the number of electrons transferred n and Faraday's constant F , which are well known, the diffusion coefficient of the mediator D can be calculated by CC.

3) Chrono amperometry

The study of the variation of the current response with time under potentiostatic conditions is known as CA. The current resulting from a step in the value of the potential in a system where there is no electrode reaction corresponding to the mass-transport-limited current can be calculated for the simple system O (oxidant) + $ne^- \leftrightarrow R$ (reductant), where only O or R is initially present. This current is the faradic current, because it is due only to a faradic electrode process (only electron transfer). However, the application of a potential step at t_0 to an electrode as shown in Figure 2.17 (a), gives rise to a diffusion-limited current whose value varies with time. The Cottrell equation³⁵⁾ (equation 2.12):

$$i(t) = i_d(t) = \frac{nFAD_o^{1/2}C_o^*}{\pi^{1/2}t^{1/2}}, \quad (2.12)$$

where i_d represents the diffusion-limited current, C_o^* represents the initial concentration of the reducible analyte *, and D_o represents the diffusion coefficient for species O, indicates a decrease in the current with $t^{1/2}$, which is shown in Figure 2.17 (b).

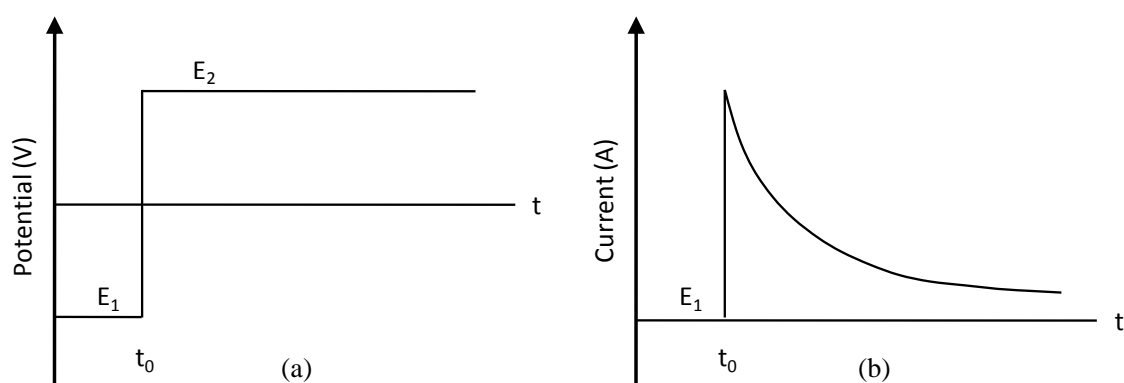


Figure 2.17 (a) Potential step applied in a typical chrono amperometry study, and (b) variation of the current with time according to the Cottrell equation.

2.10.2 Electrochromic measurements

1) Coloration efficiency

The performance of ECD can be described by many parameters, such as listed below:

- (i) transferred charge during oxidation (Q_o) and reduction(Q_r),
- (ii) optical density change ΔOD , and
- (iii) coloration efficiency η ,

which is defined as the change in the optical density for the charge (Q) consumed per unit electrode area (A). These parameters are calculated by the following equations:³⁶⁾

$$\Delta OD = -\log \frac{T_c}{T_b}, \quad (2.13)$$

$$\eta(\lambda) = \frac{\Delta OD(\lambda)}{Q}, \quad (2.14)$$

where T_b and T_c are the transmittance of the device in the bleached and colored states, respectively. The determination of coloration efficiency is a good method for quantifying the electroactive properties of an ECD.

2) Response time

The response speed of an ECD device is an important parameter for devices that are used as displays. The response time is calculated by taking the time for the transmittance change from the bleached to the colored state when a potential step is applied to the ECD. The *in situ* transmittance change is determined using a spectrometer. The response times for coloring and bleaching are defined as the time required for achieving an 80% change in the transmittance (Figure 2.18).

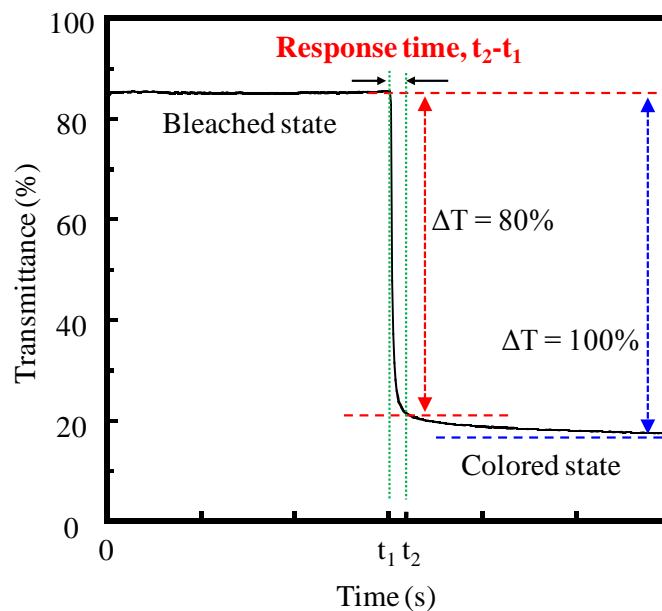


Figure 2.18 Definition of response time.

References

- 1) Y.-Y. Huang, K.-S. Chou: *Ceram. Int.* **29** (2003) 485.
- 2) D. B. Hall, P. Underhill, J. M. Torkelso: *Poly. Eng. Sci.* **38** (1998) 2039.
- 3) A. G. Emslie, F. T. Bonner, L. G. Peck: *J. Appl. Phys.* **29** (1958) 858.
- 4) E. Washizu, A. Yamamoto, Y. Abe, M. Kawamura, K. Sasaki: *Solid State Ionics* **165** (2003) 175.
- 5) Y. Abe, T. Suzuki, M. Kawamura, K. Sasaki, H. Itoh: *Sol. Energy Mater. Sol. Cells* **99** (2012) 38.
- 6) W. Estrada, M. C. A. Fantini, S. C. de Castro, C. N. P. Fonseca, A. Gorenstein: *J. Appl. Phys.* **74** (1993) 5835.
- 7) Y. Huang, Y. Zhang, X. Hu: *Sol. Energy Mater. Sol. Cells* **77** (2003) 155.
- 8) Y. He: *CuInS₂ Thin Films for Photovoltaic: RF Reactive Sputter Deposition and Characterization*, (Justus Liebig University Giessen, 2003) p.13.
- 9) P.J. Kelly, R.D. Arnell: *Vacuum* **56** (2000) 159
- 10) D. E. Clark: *Safety and the laboratory centrifuge*, Division of Chemical Health and Safety of the American Chemical Society (Elsevier Science Inc., 2001) p.7
- 11) O. M. Griffith: *Practical Techniques for Centrifugal Separations*, THERMO FISHER SCIENTIFIC Application Guide, p.5.
- 12) V. D.C. Shields: *High resolution ultrastructural investigation of insect sensory organs using field emission scanning electron microscopy* (Microscopy: Science, Technology, Applications and Education, FORMATEX 2010) p.321.
- 13) J. M. Huggett, H. F. Shaw: *Clay Minerals* **32** (1997) 197.
- 14) J. Pawley: *Scanning* **19** (1997) 324.
- 15) M. Weitz, T. Heupel, T.W. Hänsch: *Appl. Phys. B* **65** (1997) 713.
- 16) ANELVA Inc.: 911-9159 Nano scope manual, p.8.
- 17) S. Beke, L. Korosi, L. Nanai, F. Brandi: *Vacuum* **86** (2012) 2002.
- 18) B. D. Cullity, S. R. Stock: *Elements of X-ray Diffraction Third Edition* (2001 Prentice Hall, NJ 07458) p.95.
- 19) T.C. Huang, R. Gilles, G. Will: *Thin Solid Films* **230** (1993) 99.
- 20) D. Windover, E. Barnat, J. Y. Kim, M. Nielsen, T.-M. Lu, A. Kumar, H. Bakhru,

- C. Jin, S. L. Lee: Adv. X-ray Anal. **42** (2000) 590.
- 21) Y. Fujii: Adv. Anal. Chem. **3** (2013) 9.
- 22) F. A. Settle: *Handbook of Instrumental Techniques for Analytical Chemistry* (Leandregg, 1997), p.249.
- 23) L.-E. Amand, C. J. Tullin: *The Theory Behind FTIR analysis*, p.2.
- 24) Online edition for students of organic chemistry lab courses at the University of Colorado, Boulder, Dept of Chem and Biochem. *Infrared Spectroscopy: Theory* (2002) p.155.
- 25) S.W. King, M. French, J. Bielefeld, W.A. Lanford: J. Non-Crystalline Solids **357** (2011) 2970.
- 26) S. Petit, J. Madejova: Develop. Clay Sci. **5** (2013) 213.
- 27) N. D. Jaeger, H. Demeyere, R. Finsy, R. Sneyers, J. Vanderdeelen, P. Meeren, M. Laethem: Part. Part. Syst. Charact. **8** (1991) 179.
- 28) J. Kim and D. F. Lawler: Bull. Korean Chem. Soc. **26** (2005) 1083.
- 29) R. D. Letterman: Water Quality and Treatment, 5th Ed. McGraw-Hill, (New York, (1999)) sec. 6.1.
- 30) R. Greenwood, K. Kendall: J. Europ. Cera. Soc. **19** (1999) 479.
- 31) D. Hanaor, M. Michelazzi, C. Leonelli, C. C. Sorrell: J. Europ. Cera. Soc. **32** (2012) 235.
- 32) W. Li, P. Simmons, D. Shrader, T. J. Herrman, S. Y. Dai: Talanta **112** (2013) 43.
- 33) A. J. Bard, L. R. Faulkner: *Electrochemical Method; Fundamentals and Applications, Second Edition*, (JOHN WILEY & SONS, Inc, 2000) p.227.
- 34) V. Fragkou, Y. Ge, G. Steiner, D. Freeman, N. Bartetzko, A. P. F. Turner: Int. J. Electrochem. Sci. **7** (2012) 6214.
- 35) A. J. Bard, L. R. Faulkner: *Electrochemical Method; Fundamentals and Applications, Second Edition*, (JOHN WILEY & SONS, Inc, 2000) p.163.
- 36) K.-C. Chen, C.-Y. Hsu, C.-W. Hu, K.-C. Ho: Sol. Energy Mater. Sol. Cells **95** (2011) 2238.

Chapter 3 Improvement of Electrochemical and the Electrochromic Properties of Particle Size-Classified Zinc Hexacyanoferrate Nanoparticles and Their Application in Electrochromic Devices

3.1 Introduction

Transmissive ECD requires a CE material that is colorless in both oxidized and reduced states or electrochromic in a complementary sense to a WE. NiHCF films have been used as CEs for FeHCF transmissive ECDs because of their good durability. NiHCF films exhibit EC between yellow and colorless in the oxidized and reduced states, respectively, and FeHCF films are blue and transparent, respectively. Therefore, the Fe-NiHCF ECD is pale yellow in the bleached state. In contrast, an ECD with a combination of FeHCF and ZnHCF films exhibits a color change resembling that of the EC of FeHCF because ZnHCF is nearly colorless in both oxidized and reduced states. However, ZnHCF films have a lower cycling stability.¹⁻²⁾ The typical particle size of ZnHCF particles is 200–500 nm,¹⁾ which is much larger than those of FeHCF and NiHCF-NPs (less than 100 nm).³⁻⁸⁾ The large particle size of the ZnHCF particles may explain its low cycling stability. To reduce the particle size of ZnHCF-NPs synthesis methods that are environmentally friendly, inexpensive, and compatible with various MHCFs have been reported.⁵⁾ For example, the particle size of water-dispersible FeHCF-NPs was estimated to be approximately 10 nm.⁹⁾

In this chapter, a method for the preparation of ZnHCF-NPs less than 100 nm in size is described. First, a solution of water-dispersible ZnHCF particles was prepared.⁶⁾ The ZnHCF particles were segregated into components with different sizes *via* centrifugation. The effects of the particle size on the cycle durability and transferred charge density of ZnHCF-NP thin films were then examined to clarify their potential as CEs for ECDs. In addition, transmissive ECDs with a combination of FeHCF-NP and ZnHCF-NP thin films were fabricated, and the electrochromic and electrochemical properties of these devices were evaluated.

3.2 Experimental procedure

3.2.1 Preparation of zinc and iron HCF thin films

The method for preparing water-dispersible ZnHCF-NPs resembles that used to prepare FeHCF-NPs.⁶⁾ An aqueous solution (300 mL) of ZnCl₂ (21.8 g), 10 wt% HCl (5 mL), and an aqueous solution (300 mL) Na₄[Fe(CN)₆]·10H₂O (38.8 g) was vigorously stirred for 10 min using a homogenizer. The resulting white precipitate (insoluble ZnHCF precursor) was washed with Milli-Q (Milli pore Milli-Q system) water five times in a centrifuge to yield insoluble ZnHCF-NPs. Next, 200 mL of an aqueous solution of Na₄[Fe(CN)₆]·10H₂O (11.62 g) was added to the ZnHCF precursor as a surface modifier, and the mixture was stirred at room temperature for 1 day to afford the desired water-dispersible ZnHCF-NPs (ZnHCF-NP^{mix}).

The ZnHCF-NPs were then separated using an ultracentrifuge (Optima L-90K, Beckman Coulter, Inc.), and three types of size-classified ZnHCF-NPs were obtained at acceleration levels of 1,700 g, 9,000 g, and 20,000 g, where g represents the gravitational acceleration unit (see Figure 3.1).

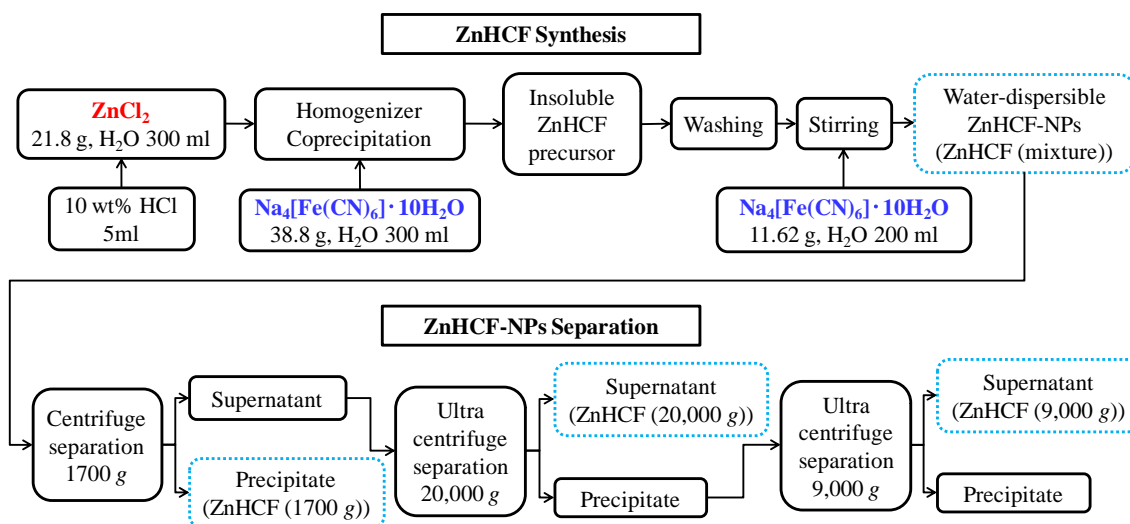


Figure 3.1 Flow chart for ZnHCF synthesis and separation of the ZnHCF-NPs.

Water-dispersible FeHCF-NPs were also synthesized in a similar manner.⁶⁾ An

aqueous solution (90 mL) of $\text{Na}_4[\text{Fe}(\text{CN})_6]\cdot 10\text{H}_2\text{O}$ (17.42 g, 36 mmol) was added to 90 mL of an aqueous solution of $\text{Fe}(\text{NO}_3)_3\cdot 9\text{H}_2\text{O}$ (19.38 g, 48 mmol), and the mixture was vigorously stirred for 3 min. The resulting blue precipitate was washed five times with Milli-Q water, and then 60 ml of an aqueous solution of $\text{Na}_4[\text{Fe}(\text{CN})_6]\cdot 10\text{H}_2\text{O}$ (4.1 g) was added to increase the dispersibility in the aqueous solution *via* surface modification. The water-dispersible FeHCF-NP solution was stirred at room temperature for 1 week.

Generally, wet chemical deposition techniques are cost-effective methods for the preparation of large-area thin films, and are also technically less demanding than physical evaporation techniques.¹⁰⁻¹¹⁾ Spin coating is widely used for the deposition of metal coordination complex thin films such as MHCFs. Thus, thin films of the ZnHCF samples were fabricated on indium tin oxide (ITO)/glass substrates by spin coating using aqueous dispersions of each ZnHCF-NP with a concentration of 0.1 g/mL. The film thickness of the ZnHCF thin films was controlled by adjusting the rotation rate of the spin coater. To fabricate the ECDs, the film thickness of the ZnHCF thin films was also controlled to match the charge capacity of the redox reactions with that of the FeHCF WEs. The conditions for spin coating are summarized in Table 3.1.

Table 3.1 Rotation rates of spin coating for the ZnHCF-NP thin films described in section 3.3. (in dry air)

Dispersion liquids	For thin films	For ECDs
ZnHCF (mixture)	3000 rpm 10 s, 3500 rpm 10 s	600 rpm 60 s, 1500 rpm 10 s
ZnHCF (1,700 g)	3000 rpm 10 s, 3500 rpm 10 s	600 rpm 60 s, 1500 rpm 10 s
ZnHCF (9,000 g)	2500 rpm 10 s, 3000 rpm 10 s	800 rpm 10 s, 1200 rpm 10 s
ZnHCF (20,000 g)	2000 rpm 10 s, 2500 rpm 10 s	1300 rpm 10 s, 1800 rpm 10 s

The FeHCF-NP thin films used to fabricate ECDs were spin-coated at rotation rates of 3000 rpm for 10 s and 3500 rpm for 10 s using 0.1 g/mL FeHCF-NPs aqueous dispersions, and the thickness of the films was confirmed to be approximately 150 nm by FESEM analysis as shown in Figure 3.2 (b).

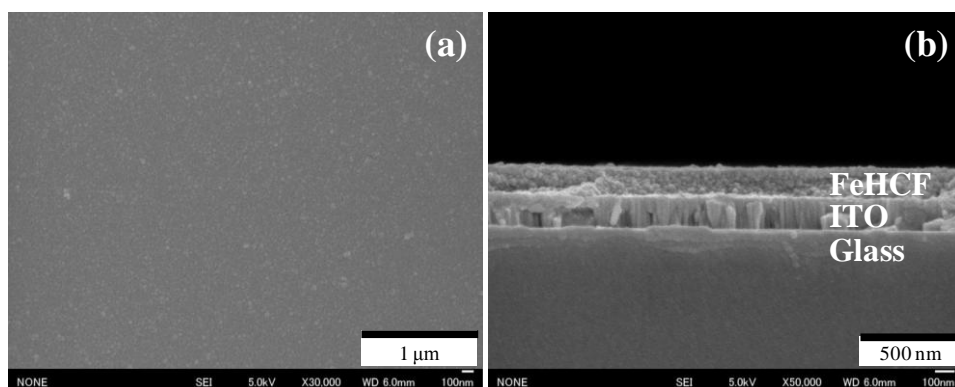


Figure 3.2 FESEM images of the FeHCF-NP thin film on an ITO/glass substrate: (a) top-view and (b) cross-sectional image.

3.2.2 Assembly of transmissive Fe-ZnHCF ECDs

The layered structure of the Fe-ZnHCF ECDs was prepared as schematically shown in Figure 3.3. The mixed electrolyte consisted of potassium bis(trifluoromethanesulfonyl)imide (KTFSI)/ propylene carbonate (PC) electrolyte and polymethyl methacrylate (PMMA) (KTFSI/PMMA/PC = 3.83 g/36 g/120.5 g). The electrolyte was spread on the FeHCF film by an air pulse dispensing method (Shot Master 200DS, Musashi Engineering Inc., Japan). The CE coated with the size-classified ZnHCF-NP and the WE with the FeHCF-NPs were bonded together using a UV-cured resin under a vacuum. The distance between the two ITO/glass substrates of the ECDs was 100 μm , and the active area was $17 \times 19 \text{ mm}^2$.

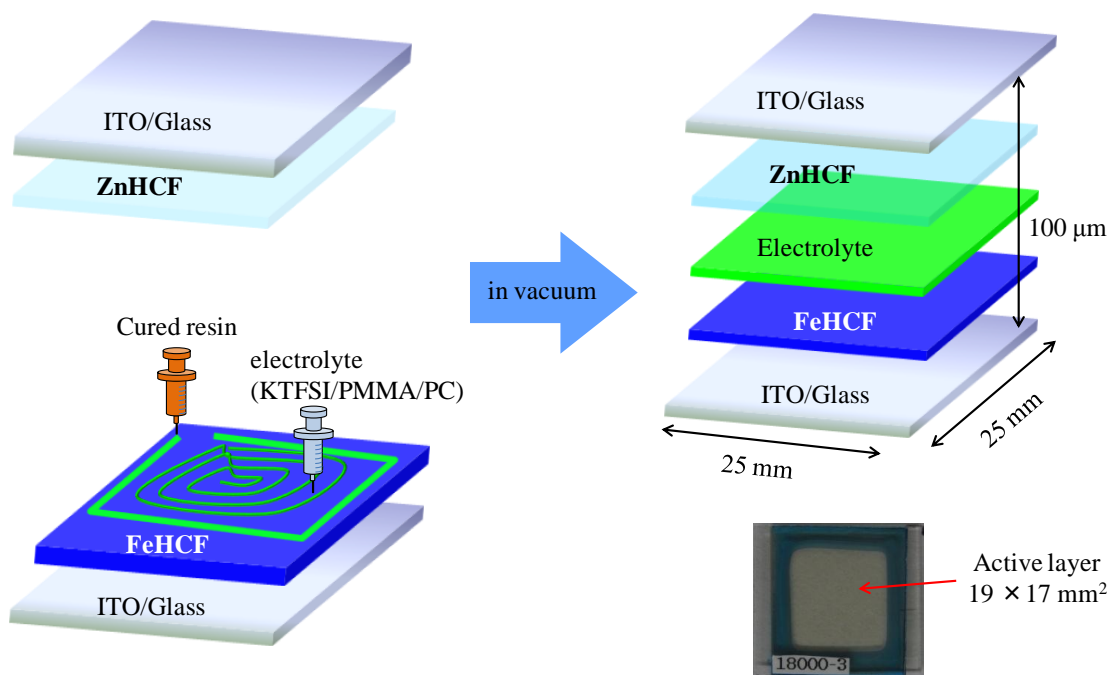


Figure 3.3 Schematic illustration and photograph of a Fe-ZnHCF ECD and its preparation method.

3.2.3 Characterization methods

The crystal structure and particle size of the ZnHCF-NPs were evaluated by XRD analysis at room temperature using a Rigaku Ultima III X-ray diffractometer with monochromatic Cu K α ($\lambda = 1.54 \text{ \AA}$) radiation in the 2θ range from 5 to 65° with a scan speed of 1°/min and a step size of 0.04°. The particle size, morphology and thickness of the ZnHCF and FeHCF thin films were investigated using a field emission scanning electron microscope (FE-SEM, S-4800II, Hitachi) at an acceleration voltage of 5kV and a working distance of ~8 mm. The average particle size of the particles in the ZnHCF dispersions was determined using a Delsa™ nano submicron particle size and zeta potential particle analyzer (PN A54412AA, Beckman Coulter, Inc., Ireland). The electrochemical response of the ZnHCF thin films and ECDs were studied by CV using an electrochemical analyzer (ALS-6115D, BAS, Japan), and *in situ* optoelectrochemical measurements were performed using a spectrometer (UV-USB4000, Ocean Optics). The cyclic durability of the ZnHCF-NP thin films was determined by CC, in which constant oxidation voltages of 1.4 V and 0.4 V for 15 s, respectively, were repeatedly applied for 10,000 cycles.

3.3 Characterization of the ZnHCF-NPs and their thin films

3.3.1 Surface and cross-sectional morphologies and particle size

First, the particle sizes of the size-classified ZnHCF-NPs by the centrifuge process were measured. The difference in the particle sizes is readily apparent in the FE-SEM images of the films shown in Figure 3.4. The particle size of the ZnHCF-NPs mixture (as-synthesized water-dispersible nanoparticles) was very widely distributed from 20 nm to 250 nm, as shown in the second column in Table 3.2. In contrast, the thin films of the ZnHCF-NPs prepared by the centrifuge separation process had a narrow size distribution, as can be seen in Figures 3.4 (b) ~ (d) and Table 3.2. The particle size decreased with increasing acceleration in the centrifuge process. The results also show that the separated ZnHCF-NP thin films had a dense structure. A similar tendency was observed for the average particle size (d_{avg}) of the dispersed particles as estimated by DLS, (third column in Table 3.2). Hereafter, the mixture of the water-dispersible ZnHCF-NPs is referred to as ZnHCF-NP^{mix}, and the classified NPs are referred to as ZnHCF-NP²¹⁴, ZnHCF-NP⁷¹, and ZnHCF-NP⁵⁹, as listed in the fourth column in Table 3.2.

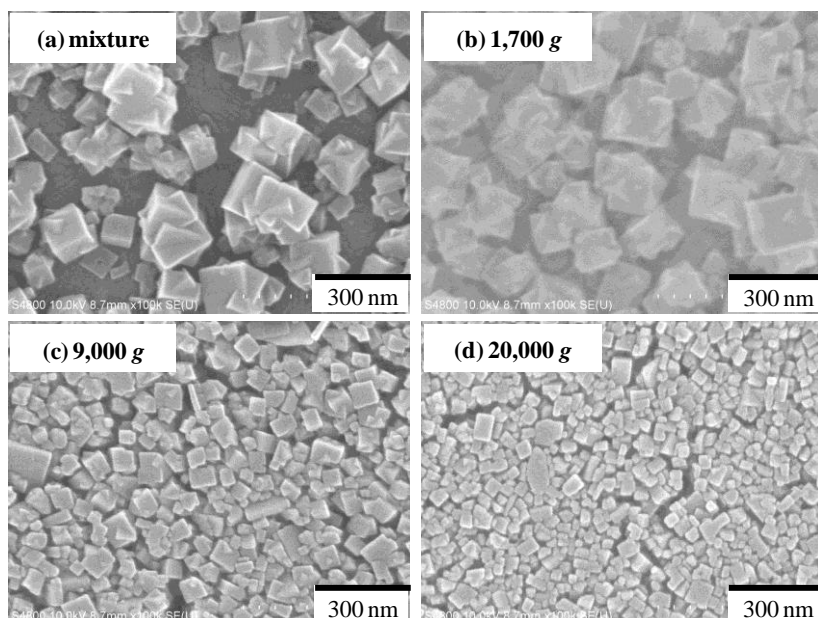


Figure 3.4 Top-view FE-SEM images of the size-controlled ZnHCF-NP thin films on ITO substrates.

Table 3.2 Particle size distribution and average particle size, d_{avg} , of the ZnHCF-NPs.

Acceleration	Particle size distribution*	d_{avg} **	Sample name
w/o	20–250 nm	183 nm	ZnHCF-NP ^{mix}
1,700 g	100–250 nm	214 nm	ZnHCF-NP ²¹⁴
9,000 g	30–80 nm	71 nm	ZnHCF-NP ⁷¹
20,000 g	20–60 nm	59 nm	ZnHCF-NP ⁵⁹

*The distribution were obtained from FE-SEM images. **The average particle sizes were obtained from DLS measurement.

The thin films of the ZnHCF-NP^{mix} and ZnHCF-NP²¹⁴ NPs shown in Figures 3.5 (a) and (b), respectively, had a rough structure with variously shaped NPs. In contrast, the ZnHCF-NP⁷¹ and ZnHCF-NP⁵⁹ thin films were uniformly spread on the ITO glass substrates.

The film thickness of each sample was determined from three SEM images using 10 sections per image, and the standard deviations (SD) of the film thicknesses depended on the particle sizes of the ZnHCF-NPs; those of the ZnHCF-NP⁷¹ and ZnHCF-NP⁵⁹ films were calculated to be 9.67 nm and 7.26 nm, respectively. These values are smaller than those for the ZnHCF-NP^{mix} (21.27 nm) and ZnHCF-NP²¹⁴ (27.25 nm) films. The small SD values indicate that the films with smaller NPs Had smooth surface.

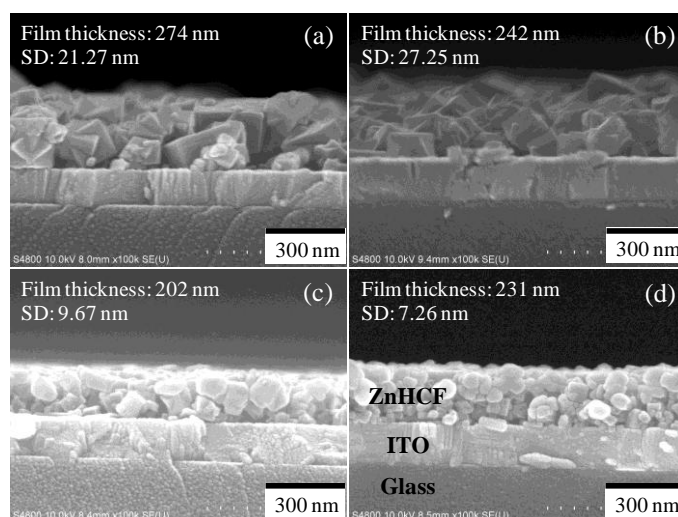


Figure 3.5 Cross-sectional FE-SEM images of the ZnHCF thin films on ITO substrates; (a) ZnHCF-NP^{mix}, (b) ZnHCF-NP²¹⁴, (c) ZnHCF-NP⁷¹, and (d) ZnHCF-NP⁵⁹. SD means the standard deviation of the film thickness measured from the SEM images.

3.3.2 Crystal structure

The crystal structures of the ZnHCF-NPs were investigated by XRD analysis. The powder XRD patterns of the dried size-classified ZnHCF-NPs are shown in Figure 3.6. The crystal structures of all of the samples were found to be trigonal- $\text{Zn}_3[\text{Fe}(\text{CN})_6]_2$ ($\text{Zn}:\text{Fe} = 3:2$)¹², indicating no change following the classification of the ZnHCF-NPs. Moreover, the crystallite sizes of the classified ZnHCF-NPs were estimated using the width of the main peak near $2\theta = 16.3^\circ$, which corresponds to the (113) plane, using the Scherrer equation, and the values are shown in Table 3.3. The crystallite sizes, of all of the samples estimated from the XRD results were approximately 20 nm. The differences in the particle sizes seen in Table 3.2 and the crystallite sizes listed in Table 3.3 can be explained by the fact that the XRD peaks reflect the sizes of the primary particles, while the DLS results reflect the sizes of the secondary particles.

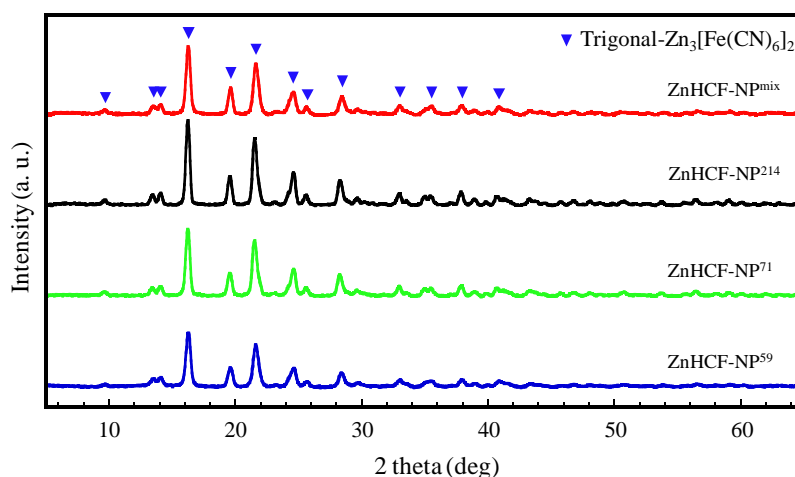


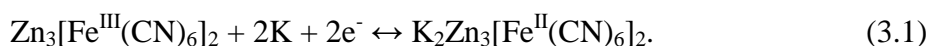
Figure 3.6 Powder XRD patterns of the size-classified ZnHCF-NPs.

Table 3.3 Full-width at half maximum of the (113) XRD peaks shown in Figure 3.6 and the crystallite size for each size-classified ZnHCF-NPs calculated from the Scherrer analysis.

Sample	FWHM (deg)	Crystallite size (nm)
ZnHCF-NP ^{mix}	0.40	22
ZnHCF-NP ²¹⁴	0.36	24
ZnHCF-NP ⁷¹	0.38	22
ZnHCF-NP ⁵⁹	0.42	20

3.3.3 Electrochemical properties

Cyclic voltammograms for each of the ZnHCF-NP thin films are shown in Figure 3.7, in each of which a pair of main peaks can be observed due to the redox reaction of the iron centers ($\text{Fe}^{\text{II/III}}$).¹³⁾ The redox reaction at the main current peak of the ZnHCF-NP thin films (approximately 1.0 V for oxidation and 0.8 V for reduction) is as follows:



The difference in the oxidation and reduction peak current potentials decreased, and the peak current increased with decreasing ZnHCF-NP particle size. This result indicates the acceleration of the redox reaction due to the use of smaller particles. The ZnHCF-NP thin films with smaller particles had smaller differences in the redox potentials and peak voltages. The improved electrochemical properties, namely the higher current density and smaller difference in the peak voltages, for the smaller particle size ZnHCF-NPs may be due to the shortening of the ion-diffusion path for the smaller NPs.

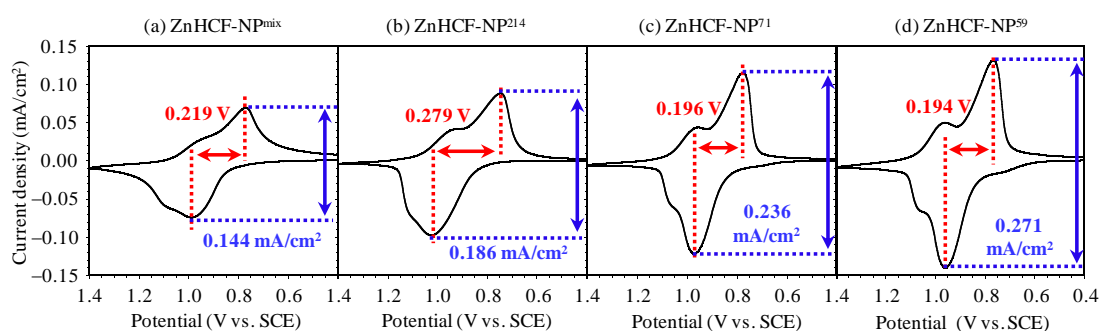


Figure 3.7 Initial cyclic voltammograms for the size-controlled ZnHCF-NP thin films.

3.3.4 Electrochromic property

To clarify the electrochromic activity, the optical properties of the ZnHCF-NPs thin films were evaluated. Figure 3.8 shows the transmittance spectra of the ZnHCF-NPs thin films in the oxidized and reduced states. All of the thin films exhibit slight changes in their transmittance spectra except in the short wavelength region below 500 nm. Notably, the transmittance in the bleached state for the ZnHCF-NP films with smaller particles (ZnHCF-NP⁷¹ and ZnHCF-NP⁵⁹) was higher than that for the films with larger particles (ZnHCF-NP²¹⁴ and ZnHCF-NP^{mix}). This result may be due to the suppression of light scattering.

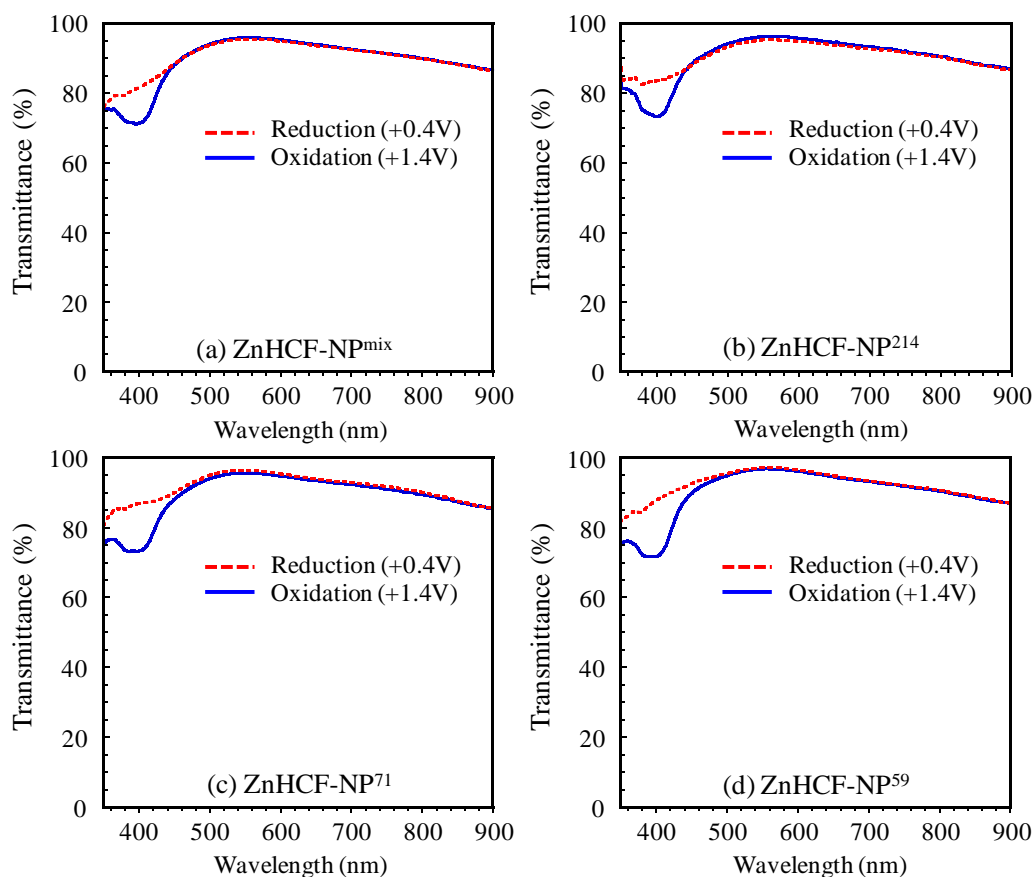


Figure 3.8 Transmittance spectra of the ZnHCF-NP thin films in reduced and oxidized states measured after applying constant voltages of 0.4 V and 1.4 V (vs. SCE) for 200 s.

The degree of the color change was evaluated on the basis of the coloration efficiency (η), and the spectra are shown in Figure 3.9. The coloration efficiency did not depend much on the size of the NPs, indicating that the active electrochromic species in the films were not that different for the different films. These results suggest that the electrochromic species in all of the films was the same and that it was the iron center of the HCF portion of the ZnHCF.

The ZnHCF-NP thin films exhibited maximum η values of 12.9 ~ 16.6 cm^2/C at $\lambda = 400$ nm. In addition, the value of η decreased below 2.3 cm^2/C in the long wavelength region ($\lambda > 450$ nm). Such a low value for η is essential for the use of the films as CEs in transmissive ECDs.

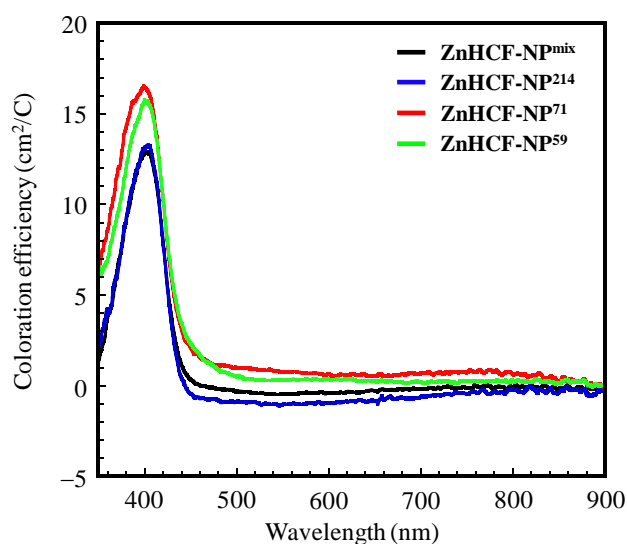


Figure 3.9 Coloration efficiency of the size-classified ZnHCF-NP thin films as functions of wavelength.

3.3.5 Durability

To study the durability of the ZnHCF-NP thin films, the transferred charge density during oxidation and reduction was measured, and the results are shown in Figure 3.10. The transferred charge density of the ZnHCF-NP^{mix} film drastically decreased during the initial 500 cycles and subsequently stabilized. By contrast, the thin films fabricated from the smaller classes of ZnHCF-NPs (ZnHCF-NP⁷¹ and ZnHCF-NP⁵⁹) maintained a large transferred charge density, even up to 2,500 cycles.

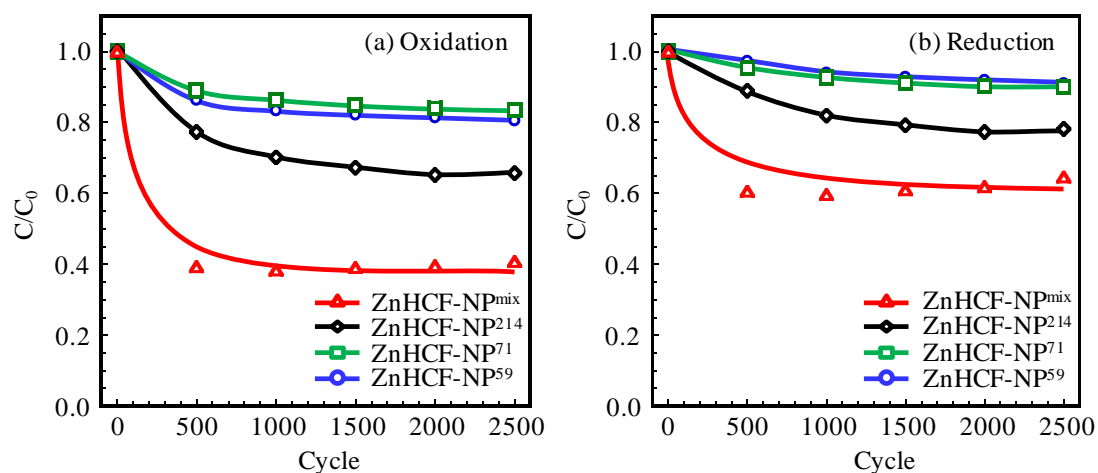


Figure 3.10 Cycle stability of the transferred charge density for the ZnHCF-NP thin films during (a) oxidation at 1.4 V and (b) reduction at 0.4 V for 15 s. C_0 and C indicate the transferred charge density at the initial cycle and those after cycles, respectively.

The best cycle durability was obtained for the thin film with the smallest class of ZnHCF-NPs⁵⁹. This thin film was then subjected to 10,000 cycles, and the CV, and CC results are shown in Figure 3.11. In this case, 80% of the initial charge capacity was maintained, even after 10,000 cycles. Consequently, the smaller ZnHCF-NP film is regarded as a very promising material for use as CE for FeHCF ECDs.

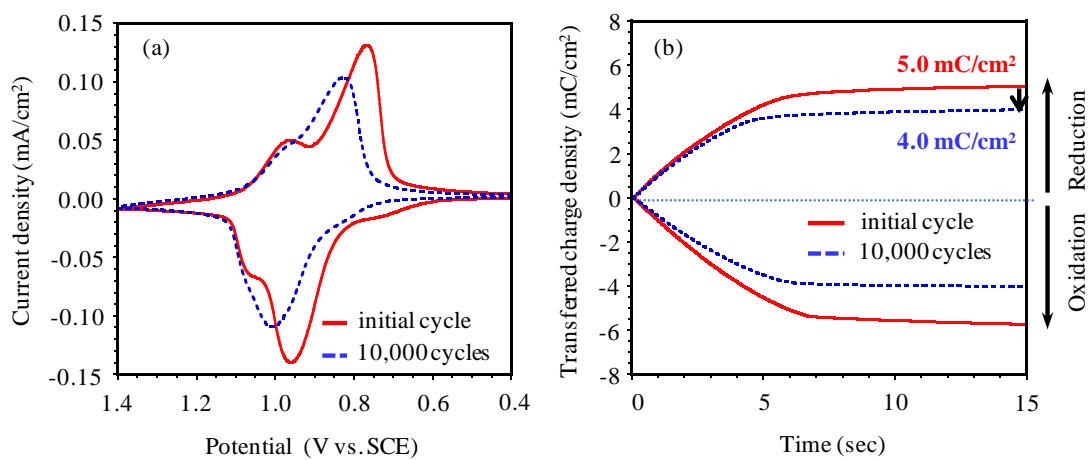


Figure 3.11 Cycle stability of the ZnHCF-NP⁵⁹ thin film: (a) cyclic voltammograms for the initial and 10,000th cycles and (b) transferred charge density during CC for the initial and 10,000th cycles.

3.4 Electrochemical and electrochromic properties of Fe-ZnHCF ECDs.

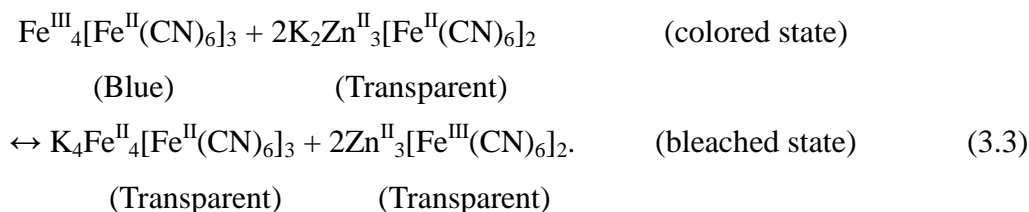
Transmissive ECDs were prepared using a combination of FeHCF-NP and size-classified ZnHCF-NP thin films, and the electrochromic and electrochemical properties of these ECDs were evaluated. Hereafter, the ZnHCF-NP/FeHCF-NP ECDs composed of ZnHCF-NP^{mix}, ZnHCF-NP²¹⁴, ZnHCF-NP⁷¹, and ZnHCF-NP⁵⁹ are referred to as ZnHCF-NP^{mix}, ZnHCF-NP²¹⁴, ZnHCF-NP⁷¹, and ZnHCF-NP⁵⁹ ECDs, respectively.

The cyclic voltammograms of the ECDs are shown in Figure 3.12, in which the horizontal axis represents the potential between the FeHCF-NP (WE) and ZnHCF-NP (CE). A main current peak was observed at potentials from -0.8 V to -0.5 V with subpeaks at -0.2 V to 0.2 V. The potential for the reaction corresponds to the redox potential difference between the FeHCF-NP and ZnHCF-NP films.

The redox reaction of ZnHCF-NP thin films was shown in equation (3.1), and that of FeHCF-NP thin films is expressed by the following equation:⁹⁾



When the Fe-ZnHCF ECD is colored, ZnHCF undergoes reduction (Fe^{3+} is reduced to Fe^{2+}) accompanied by the intake of a K^+ ion while FeHCF undergoes oxidation (Fe^{2+} gets oxidized to Fe^{3+}) accompanied by the release of a K^+ ion. Because of polarity reversal, the reactions proceed in the opposite directions. The electrochromic reaction of the ECD can be written as follows:



In the CV curves for the Fe-ZnHCF ECDs shown in Figure 3.12, a pair of well-defined redox peaks was observed. Similar to the results obtained for the ZnHCF

films (Figure 3.7), the Fe-ZnHCF ECDs with smaller ZnHCF-NP particles had smaller differences in their redox potentials. The smaller differences in the redox potentials for the ZnHCF⁵⁹ ECDs may again be due to the shortening of the ion-diffusion path in the ZnHCF-NPs films with smaller NPs.

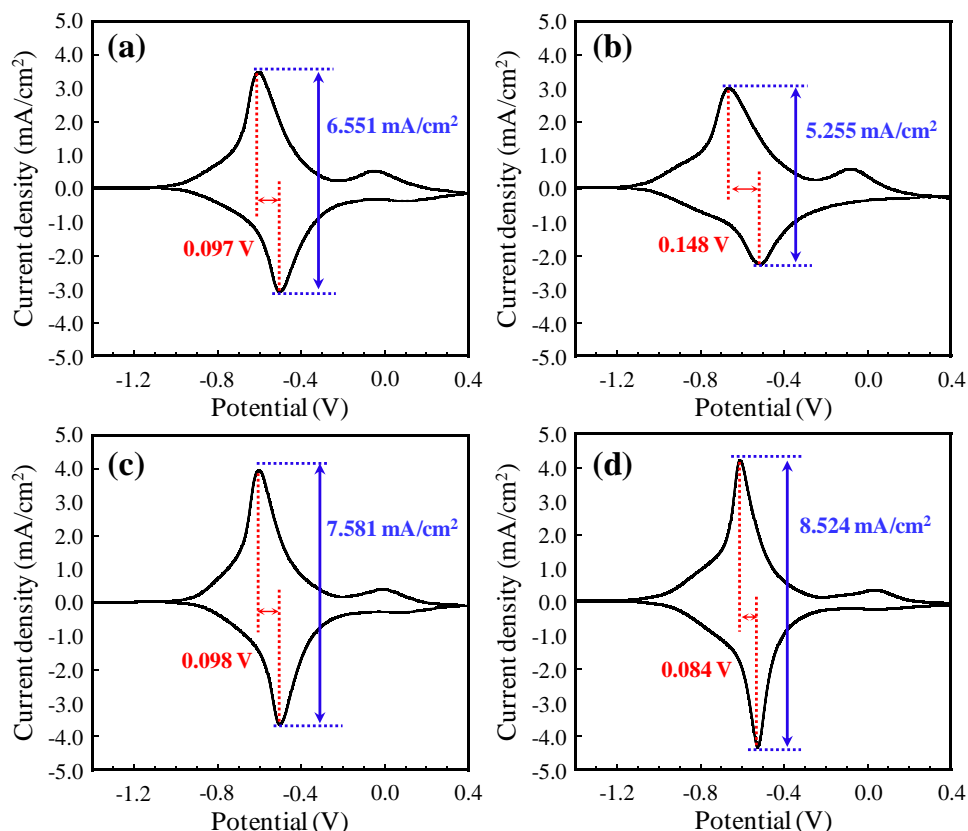


Figure 3.12 Cyclic voltammograms ($-1.4 \text{ V} \sim 0.4 \text{ V}$, 5 mV/s) for the Fe-ZnHCF ECDs. (a) ZnHCF^{mix}, (b) ZnHCF²¹⁴, (c) ZnHCF⁷¹, and (d) ZnHCF⁵⁹.

The changes in the transmittance spectra for the particles in response to applied voltages of $V = -0.2 \text{ V}$ and -1.2 V are shown in Figure 3.13. The Fe-ZnHCF ECDs, with both ZnHCF-NPs and FeHCF-NPs, exhibited clear EC. The maximum transmittance change ΔT at $\lambda = 700 \text{ nm}$ for all of the ECDs was approximately 60%, which was due to the transmittance change of the FeHCF-NPs between blue and colorless. In the shorter-wavelength region, in contrast, the value of ΔT was quite small (2-6% at $\lambda = 400 \text{ nm}$) and less than 1/10 that at $\lambda = 700 \text{ nm}$. This result indicates that the coloration change of the Fe-ZnHCF ECDs in the bleached state at $\lambda = 400 \text{ nm}$ is suppressed. Note

that the transmittance at $\lambda = 400$ nm changes in the direction opposite to that at $\lambda = 700$ nm for the redox reaction. Thus, when the change in the transmittance increases at $\lambda = 700$ nm, it decreases at $\lambda = 400$ nm. In addition, the transmittance change is fairly independent of the size of the NPs, as was the case for the ECDs mentioned in section 3.3.4.

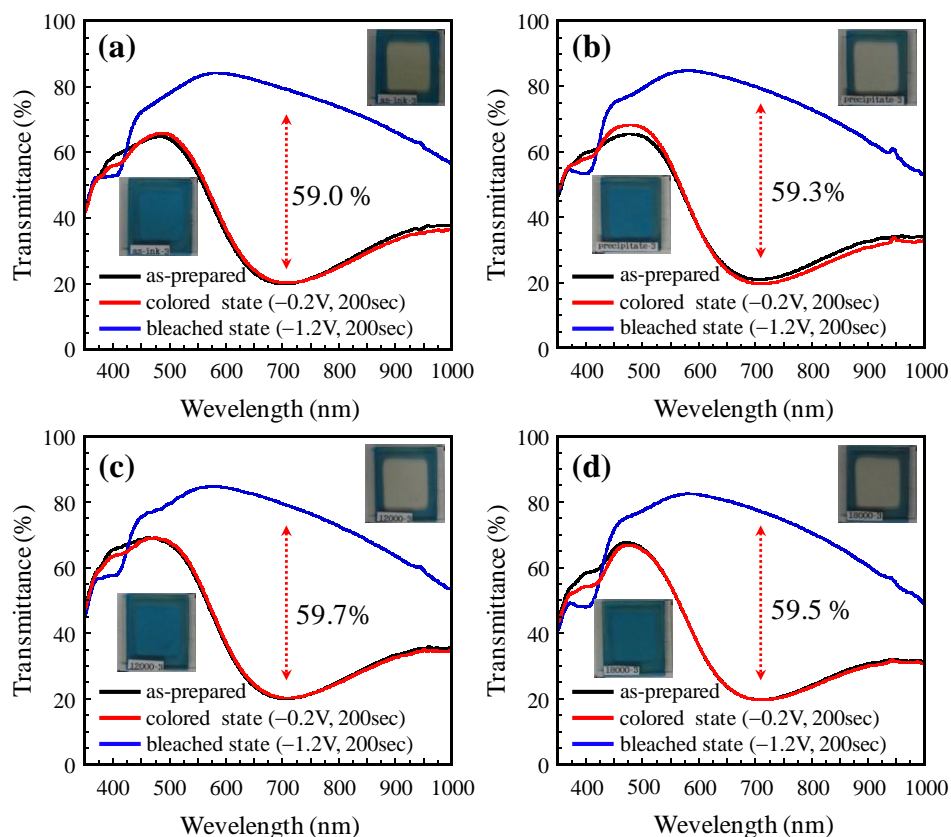


Figure 3.13 Transmittance spectra of the Fe-ZnHCF ECDs. (a) ZnHCF-NP^{mix}, (b) ZnHCF-NP²¹⁴, (c) ZnHCF-NP⁷¹, and (d) ZnHCF-NP⁵⁹ ECDs. Insets show photographs of ECDs in the colored and bleached states under the application voltages of $V = -0.2$ V and -1.2 V, respectively.

Figures 3.14 and 3.15 show the charge and transmittance changes during coloring (-0.2 V) and bleaching (-1.2 V) of the Fe-ZnHCF ECDs, respectively, where constant potentials were applied for 200 s for each step. It can be seen in Figure 3.14 that the charging speed increased by decreasing the size of the ZnHCF NPs. This behavior may be due to an increase in the diffusion rate of the K^+ ions into the ZnHCF particles.

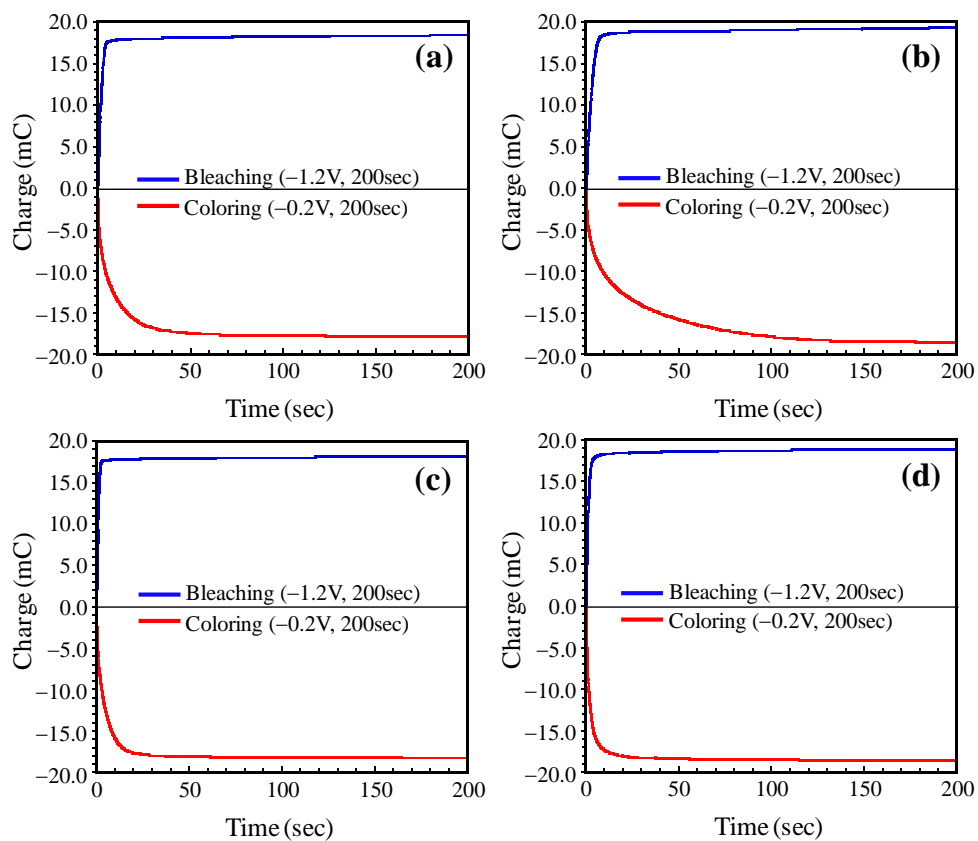


Figure 3.14 Charge during coloring (-0.2 V) and bleaching (-1.2 V) of the ECDs with size-classified ZnHCF films; (a) ZnHCF^{mix}, (b) ZnHCF²¹⁴, (c) ZnHCF⁷¹, and (d) ZnHCF⁵⁹.

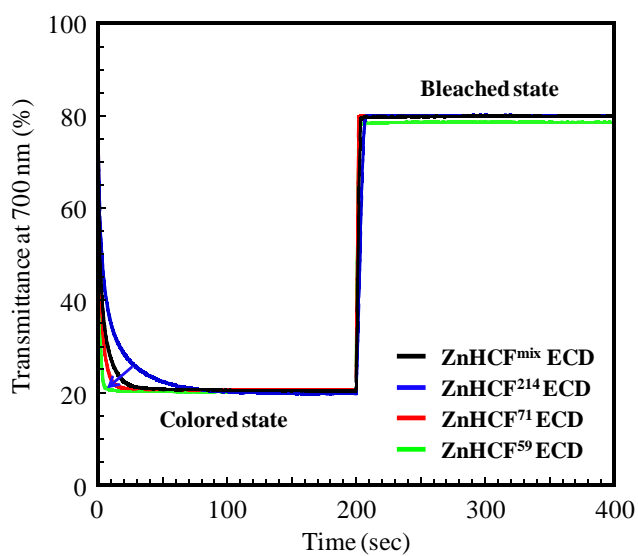


Figure 3.15 Transmittance changes for the Fe-ZnHCF ECDs at 700 nm.

Table 3.4 Electrochromic response times for the Fe-ZnHCF and Fe-NiHCF ECDs.

Structure	Coloring time (s)	Bleaching time (s)	
ZnHCF ^{mix} ECD	6.1	2.8	This study
ZnHCF ²¹⁴ ECD	13.7	5.1	This study
ZnHCF ⁷¹ ECD	3.9	1.7	This study
ZnHCF ⁵⁹ ECD	2.1	1.7	This study
Fe-NiHCF ECD	6.7	7.1	Ref. 9

The response times for coloring and bleaching are defined as the time required for an 80% transmittance change to occur from the initial state to the final state, as shown in Figure 2.18. Table 3.4 lists the response times for the Fe-ZnHCF ECDs during coloring and bleaching along with those of the Fe-NiHCF-NP ECD. The coloring and bleaching response times depended on the ZnHCF particle size, and the response times for the ZnHCF⁷¹ and ZnHCF⁵⁹ ECDs were shorter than those for the ZnHCF^{mix} and ZnHCF²¹⁴ ECDs. The high response speed may be caused by the increase in the surface area of the ZnHCF-NPs and a decrease in the ion-diffusion path for the acceptance of K⁺ ions from the electrolyte, as schematically shown in Figure 3.16.

Notably, the coloring and bleaching response times of the Fe-ZnHCF⁷¹ and Fe-ZnHCF⁵⁹ ECDs were shorter than those of the Fe-NiHCF ECD.⁹⁾

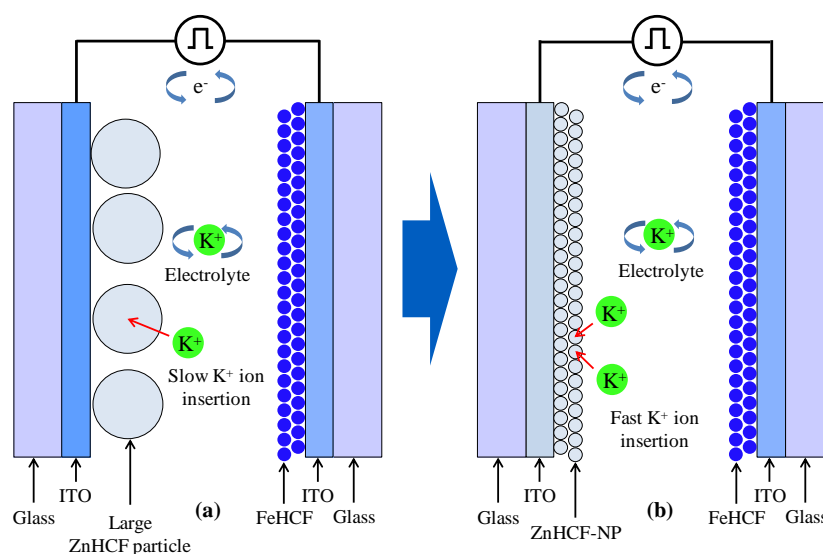


Figure 3.16 Schematic illustration of the mechanism for the increased response rate for the Fe-ZnHCF ECDs. FeHCF ECDs with (a) large and (b) small ZnHCF-NPs.

3.5 Summary

ZnHCF-NPs with particle sizes less than 100 nm were prepared by ultracentrifuge processing at accelerations of 9,000 ~ 20,000 *g*. The current density and transferred charge density of the ZnHCF-NP thin films during redox reactions increased with decreasing particle size. ZnHCF-NP thin films with smaller NPs exhibited more stable redox reactions compared to thin films with larger particles. The largest current density and maximum transferred charge density of 5.0 mC/cm² were obtained for the ZnHCF-NP thin film with an average particle size of 59 nm. The ZnHCF-NP⁵⁹ film exhibited stable cycling up to 10,000 cycles. In addition, the transmittance of the ZnHCF-NP thin films with smaller particles near $\lambda = 400$ nm for the bleached state was higher than that of the ZnHCF thin films with larger particles.

Furthermore, blue-colorless ECDs were fabricated using FeHCF films as the WEs and size-classified ZnHCF-NP thin films as the CE. A rapid response of the Fe-ZnHCF ECD (coloring time of 2.1 s and bleaching time of 1.7 s) was realized by the size reduction of the ZnHCF-NPs. The increased surface area of the ZnHCF-NPs and a decreased ion-diffusion path are thought to cause the improvement in response time.

These results indicate that ZnHCF-NPs thin films prepared by an ultracentrifuge process should be regarded as promising candidates as CE materials for FeHCF ECDs.

References

- 1) S.-F. Hong, L.-C. Chen: *Electrochim. Acta* **55** (2010) 3966.
- 2) S.-F. Hong, L.-C. Chen: *Sol. Energy Mater. Sol. Cells* **104** (2012) 64.
- 3) S. Hara, H. Tanaka, T. Kawamoto, M. Tokumoto, M. Yamada, A. Gotoh, H. Uchida, M. Kurihara, M. Sakamoto: *Jpn. J. Appl. Phys.* **46** (2007) L945.
- 4) M. Ishizaki, A. Gotoh, M. Abe, M. Sakamoto, H. Tanaka, T. Kawamoto, and M. Kurihara: *Chem. Lett.* **39** (2010) 762.
- 5) M. Ishizaki, K Kanaizuka, M. Abe, Y. Hoshi, M. Sakamoto, T. Kawamoto, H. Tanaka, M. Kurihara: *Green Chem.* **14** (2012) 1537.
- 6) Gotoh, H. Uchida, M. Ishizaki, T. Satoh, S. Kaga, S. Okamoto, M. Ohta, M. Sakamoto, T. Kawamoto, H. Tanaka, M. Tokumoto, S. Hara, H. Shiozaki, M. Yamada, M. Miyake, M. Kurihara: *Nanotechnology* **18** (2007) 345609.
- 7) D. M. Delongchamp, P. T. Hammond: *Adv. Funct. Mater.*, **14** (2004) 224.
- 8) H. Shiozaki, T. Kawamoto, H. Tanaka, S. Hara, M. Tokumoto, A. Gotoh, T. Satoh, M. Ishizaki, M. Kurihara, M. Sakamoto: *Jpn. J. Appl. Phys.* **47** (2008) 1242.
- 9) S. Hara, H. Shiozaki, A. Omura, H. Tanaka, T. Kawamoto, M. Tokumoto, M. Yamada, A. Gotoh, M. Kurihara, M. Sakamoto: *Appl. Phys. Express* **1** (2008) 104002.
- 10) E. Ozkan Zayim, I. Turhan, F.Z. Tepehan, N. Ozer: *Sol. Energy Mater. Sol. Cells* **92** (2008) 164.
- 11) S.A. Mahmoud, S.A. Aly, M. Abdel-Rahman, K. Abdel-Hady: *Physica B* **293** (2000) 125.
- 12) PDF card, 01-075-9864.
- 13) Ali Eftekhari: *J. Electroanal. Chem.* **537** (2002) 59.

Chapter 4 Improvement of the Electrochemical Properties of Water-Dispersible Copper Hexacyanoferrate Nanoparticle Films by Cu²⁺ Injection

4.1 Introduction

Copper HCF (Cu_x[Fe(CN)₆]_y, CuHCF) can be applied to wood and red brick surfaces because it exhibits a color change between brown and pale yellow due to redox reactions. For using CuHCF in ECDs, it is necessary to prepare solvent-dispersible NPs. Previously, Ishizaki *et al.* reported the synthesis of water-dispersible CuHCF-NPs via surface modification using [Fe^{II}(CN)₆]⁴⁻ ions.¹⁾ The surface modification mechanism for the water-dispersible MHCF-NPs was explained later in reports by Gotoh²⁾ and Ishizaki³⁾. However, surface-modified CuHCF-NPs have two major disadvantages: 1) useless side reactions in the cyclic voltammogram due to the surface modifier, which decrease the coloration efficiency of ECDs and 2) the high solubility of spin-coated films, which makes it difficult to fabricate multi-layer structures.

Currently, CuHCFs are synthesized by batch methods, which suffer from several disadvantages, such as limited reproducibility, extensive, time, high cost, and the consumption of large amounts of raw materials. To address these issues, a micro-mixer method was used in this study for the preparation of CuHCF. This method has been used for the mass production of organic compounds and drug substances, but has not yet been reported for the synthesis of MHCFs.

In this study, Cu²⁺ ions were injected into surface-modified CuHCF-NPs to reduce their solubility and eliminate side reactions. The electrochemical and electrochromic properties of CuHCF-NP thin films synthesized using the micro-mixer method and treated with Cu²⁺ injection were then investigated.

4.2 Experimental procedures

4.2.1 Preparation of CuHCF-NPs and thin films

Insoluble CuHCF particles were prepared by reacting a 0.6 mol/L $\text{CuSO}_4 \cdot 5\text{H}_2\text{O}$ aqueous solution and a 0.4 mol/L $\text{K}_3[\text{Fe}(\text{CN})_6]$ aqueous solution in a micro-mixer at a flow rate of 50 ml/min for each solution (Figure 4.1). Approximately 30 ml of insoluble CuHCFs (sol) was collected and washed with Milli-Q water four times using a centrifuge to yield the as-synthesized insoluble CuHCFs. Next, a 2.25 mM $\text{K}_3[\text{Fe}(\text{CN})_6]$ aqueous solution (10ml) was added to the as-synthesized insoluble CuHCFs and the mixture was stirred at room temperature for 3 days to achieve the surface modification of the dispersed CuHCF-NPs. Films of the surface-modified CuHCF NPs were deposited by the spin coating method on ITO/glass and Si substrates.

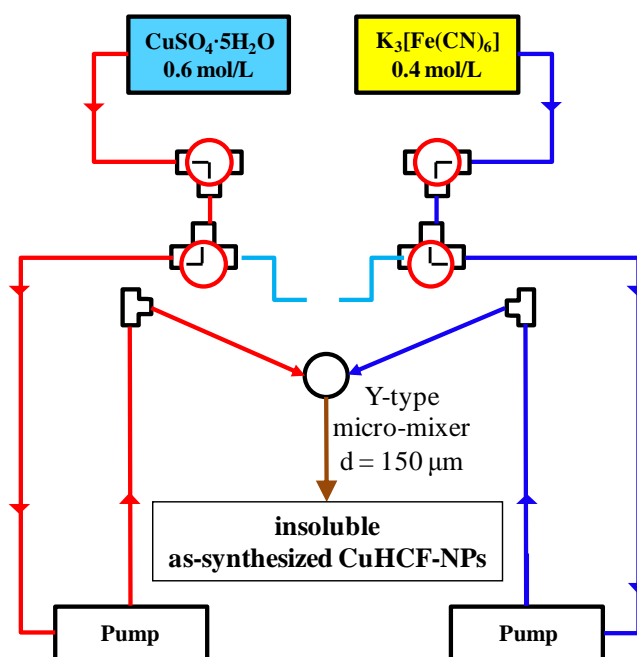


Figure 4.1 Schematic diagram of the micro-mixer process used in this study.

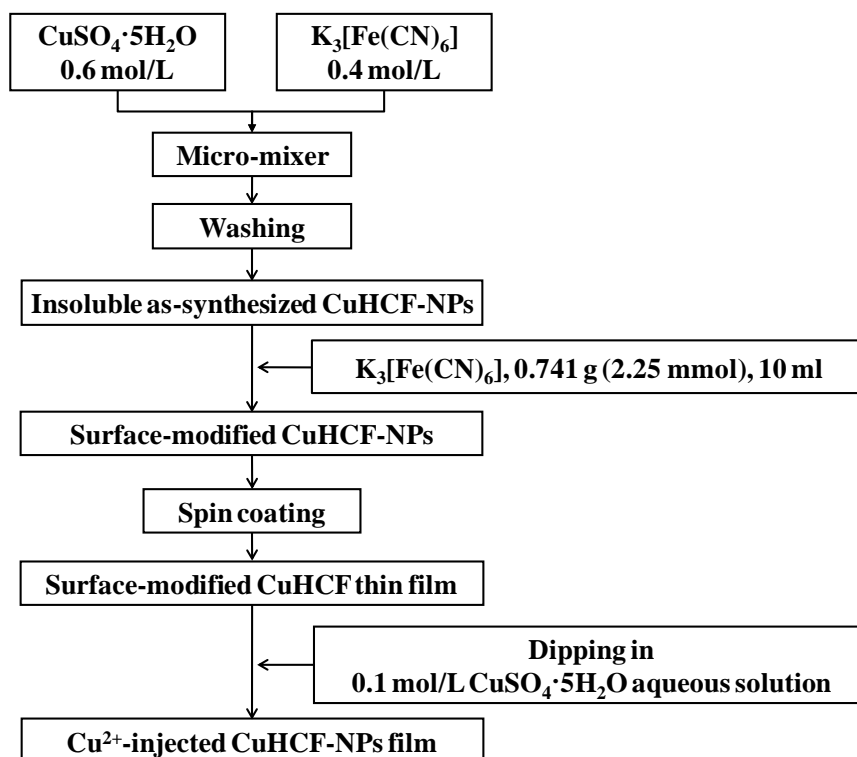


Figure 4.2 CuHCF surface modification and Cu^{2+} -injection process.

Cu^{2+} ions were injected into the surface-modified CuHCF film by rapidly dipping it into a 0.1 mol/L $\text{CuSO}_4 \cdot 5\text{H}_2\text{O}$ aqueous solution. Thus, three types of CuHCF films were prepared to compare their properties: (a) from as-synthesized NPs, (b) from surface-modified NPs and (c) Cu^{2+} -injected NPs (Figure 4.2). The effects of the surface modification and Cu^{2+} injection processes on the structure of the CuHCF NPs are schematically shown in Figure 4.3.

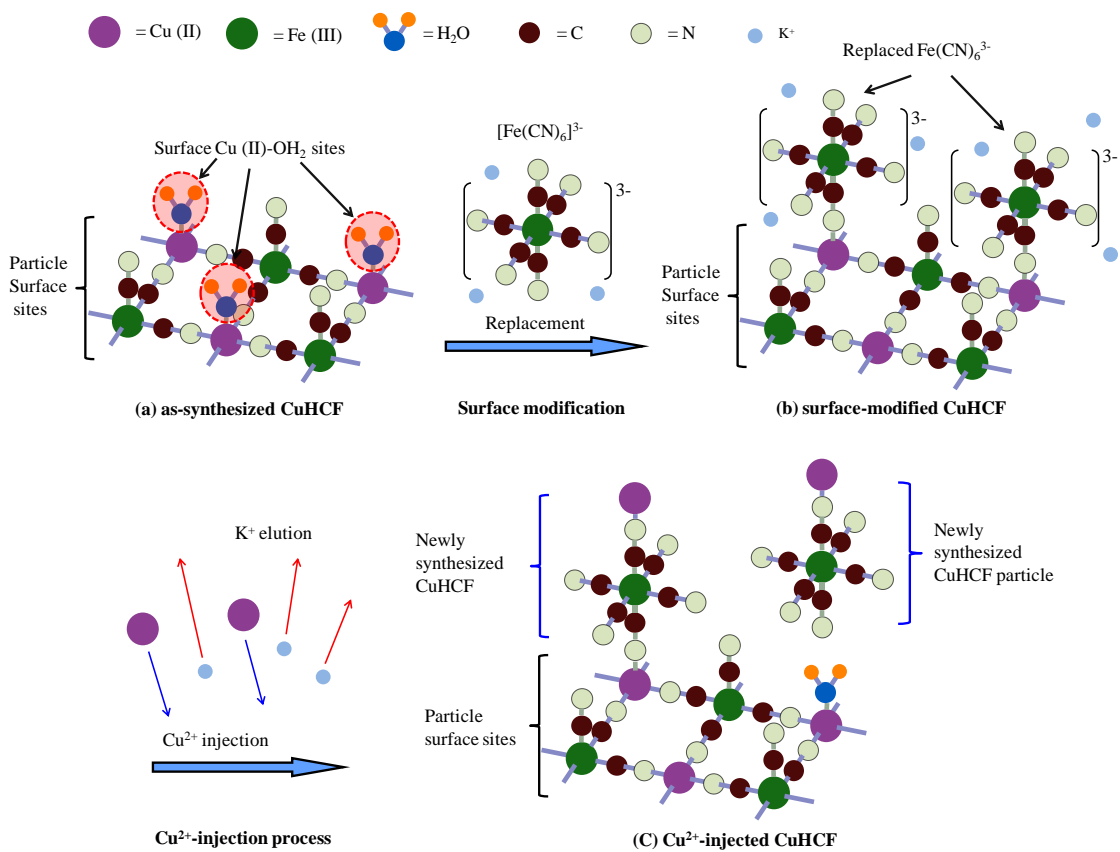


Figure 4.3 Effects of surface modification and Cu²⁺ injection processes on the structure of the CuHCF NPs.

4.2.2 Characterization methods

The crystal structures of the as-synthesized and surface-modified CuHCF powders and Cu²⁺-injected CuHCF films were evaluated by XRD analysis at room temperature with Cu K α ($\lambda = 1.54 \text{ \AA}$) radiation in the 2θ range from 10° to 70° (Ultima III, Rigaku). The zeta potentials of the three aqueous CuHCF particle solutions were measured using a Delsa™ nano submicron particle size and zeta potential analyzer (PN A54412AA, Beckman Coulter, Inc., Ireland) to characterize the dispersivity of the CuHCF-NPs. The compositions of the CuHCF samples were characterized by microwave plasma atomic emission spectrometry (MP-AES) (4100 MP-AES, Agilent Technologies). The surface morphology and structure of the CuHCF films were studied using a field emission scanning electron microscope (FE-SEM, S-4800II, Hitachi) at an accelerating voltage of 5 kV. The electrochemical and electrochromic properties of the CuHCF electrodes were determined by CV using an electrochemical analyzer (ALS-6115D, BAS, Japan). *In situ* optoelectrochemical measurements were conducted using a UV vis spectrophotometer. The CuHCF films, Pt wire, and saturated calomel electrode were used as the WE, CE and RE, respectively. The electrolyte was a mixture of 0.1 M KTFSI and PC.

4.3 Characterization of the CuHCF-NPs and thin films

4.3.1 Crystal structure

Figure 4.4 shows the XRD patterns of the as-synthesized and surface-modified CuHCF powders and the Cu^{2+} -injected thin film on a Si substrate. The crystal structures of all of the samples were found to be cubic $\text{Cu}^{\text{II}}_3[\text{Fe}^{\text{III}}(\text{CN})_6]_2$; however, the XRD pattern for the surface-modified CuHCF also exhibited XRD peaks due to $\text{K}_3[\text{Fe}^{\text{III}}(\text{CN})_6]$, which was added as a surface modifier. Because the XRD peaks due to $\text{K}_3[\text{Fe}^{\text{III}}(\text{CN})_6]$ disappeared in the XRD pattern for the Cu^{2+} -injected film, it was concluded that the surface modifier was removed during the injection of Cu^{2+} . The crystallite sizes of the CuHCF particles were estimated on the basis of the width of the main peak near $2\theta = 17.5^\circ$, which corresponds to the (200) plane of $\text{Cu}^{\text{II}}_3[\text{Fe}^{\text{III}}(\text{CN})_6]_2$, by the Scherrer equation, and the values are listed in Table 4.1. The crystallite size for all of the samples estimated from the XRD results was approximately 20 nm.

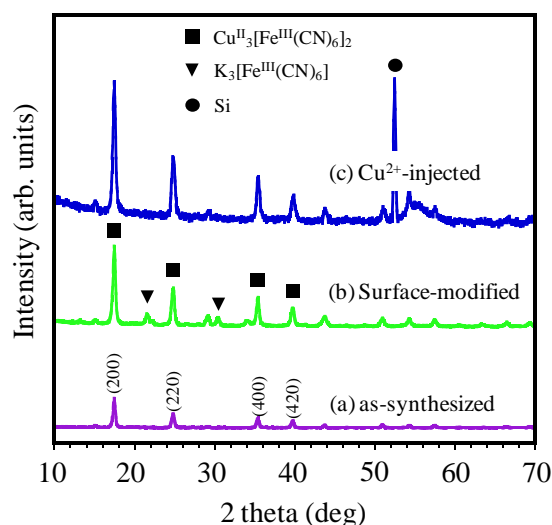


Figure 4.4 XRD patterns of the CuHCF particles and film.

Table 4.1 Full-width at half-maximum for the (200) plane and the crystallite size estimated by the Scherrer equation for each type CuHCF-NP and the film.

Sample	FWHM (deg)	Crystallite size (nm)
as-synthesized	0.37	23
surface-modified	0.41	21
Cu^{2+} -injected	0.42	20

4.3.2 Zeta potential

The zeta potentials of each of the CuHCF particle solutions are shown in Table 4.2. The zeta potential of the as-synthesized CuHCF particle solution was *ca.* -40 mV due to the presence of residual $\text{Fe}(\text{CN})_6^{3-}$ ions on the surface of the CuHCF-NPs. This zeta potential value increased to *ca.* -47 mV after surface modification and then decreased to less than -30 mV after Cu^{2+} injection. The high zeta potential of -47 mV indicated that the surface-modified CuHCF film was soluble in the aqueous solution, and the decreased zeta potential (< -30 mV) revealed the low dispersivity of the Cu^{2+} -injected CuHCF film. The low dispersivity of the film after Cu^{2+} injection indicated that it was suitable for use as an electrode in ECD with aqueous electrolytes, and that it should be possible to fabricate a multi-layer structure by stacking the insoluble coating.

Table 4.2 Change in the zeta potential of CuHCF particle solutions following surface modification and Cu^{2+} -injection.

CuHCF samples	Zeta potential (mV)	Dispersivity
as-synthesized	-39.70	Medium
surface-modified	-46.56	High
Cu^{2+} -injected	-27.48	Low

4.3.3 Surface and cross-sectional morphologies

Figure 4.5 shows the SEM images of the CuHCF films deposited on ITO coated glass substrates. The film thickness of the as-synthesized and surface-modified CuHCF thin films was approximately 200 nm (Figures 4.5 (d) and (e)). Dispersed CuHCF NPs were observed for the sample after surface modification (Figure 4.5 (a) and (b)). The change in the particle size of the surface-modified CuHCF-NPs is attributed to their high dispersivity, as mentioned in Chapter 4.3.2. However, the size of the CuHCF-NPs (Figure 4.5 (c)) decreased after Cu^{2+} injection onto the film surface. The NPs of Cu^{2+} injected into the CuHCF film are thought to be formed as a result of the reaction of the injected Cu^{2+} with the $\text{Fe}(\text{CN})_6^{3-}$ surface modifier on the film surface. The formation of the newly synthesized CuHCF-NPs was confirmed in the cross-sectional image of the Cu^{2+} -injected CuHCF film (Figure 4.5 (f)).

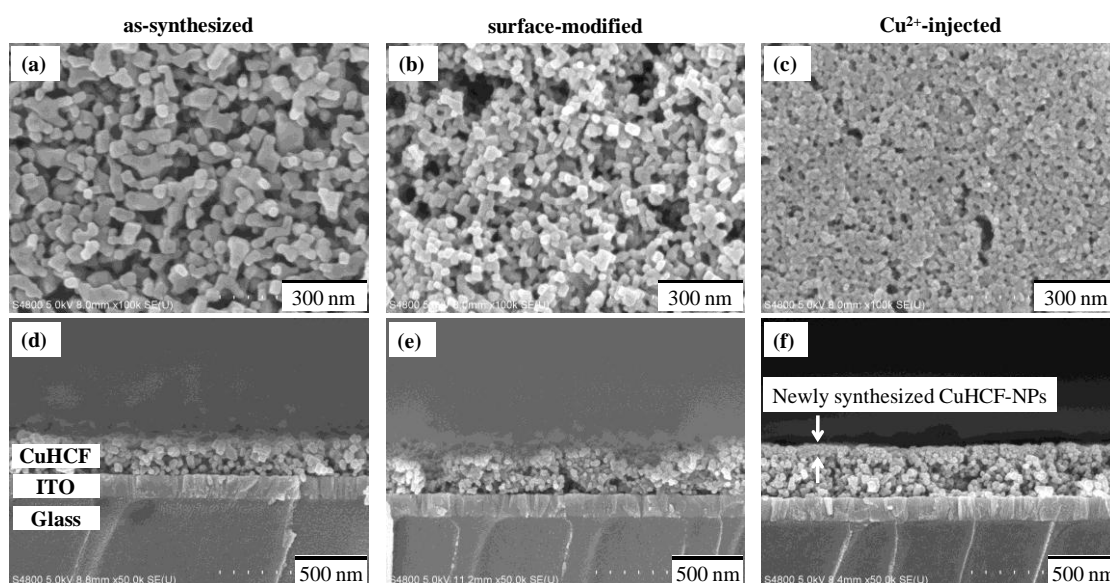


Figure 4.5 Surface (a) ~ (c) and cross-sectional (e) ~ (f) morphologies and structures of the CuHCF films.

4.3.4 Chemical composition

Table 4.3 lists the compositions of the CuHCF samples determined by MP-AES, and the change in the amounts of potassium, copper, and iron due to surface modification and Cu^{2+} injection was observed. The amount of copper in the surface-modified CuHCF film decreased by 39% compared with that of the as-synthesized CuHCF film, while the copper content in the Cu^{2+} -injected CuHCF NP film increased by 39% compared to that of the surface-modified CuHCF film.

Table 4.3 Compositions of the CuHCF samples determined using MP-AES.

CuHCF samples	Compositions	Cu/Fe	Increased amount Cu ions
as-synthesized	$\text{K}_{0.08}\text{Cu}_{1.46}[\text{Fe}(\text{CN})_6]_{1.00}$	1.46	-
surface-modified	$\text{K}_{1.01}\text{Cu}_{1.01}[\text{Fe}(\text{CN})_6]_{1.00}$	1.01	-39%
Cu^{2+} -injected	$\text{K}_{0.01}\text{Cu}_{1.40}[\text{Fe}(\text{CN})_6]_{1.00}$	1.40	+39%

4.3.5 Electrochemical properties

Figure 4.6 shows the cyclic voltammograms for each of the CuHCF films. The main peaks in Figures 4.6 (a) and (c) at approximately 0.5 ~ 0.6 V for oxidation and 0.9 ~ 1.0 V for reduction indicate the redox reaction between Fe^{2+} and Fe^{3+} . The electrochemical reaction can be written the following equation (4.1):⁴⁾



However, the surface-modified CuHCF film exhibited a side redox reaction as indicated in Figure 4.6 (b). The anodic peak at 0.0 V and the cathodic peak at 0.4 V are considered to be due to the $\text{Cu}^+/\text{Cu}^{2+}$ couple.^{4,6)} The current density of the main peak increased after Cu^{2+} injection due to the presence of newly synthesized CuHCF-NPs, which were formed by the reaction of $\text{Fe}(\text{CN})_6^{3-}$ in the surface modifier with the injected Cu^{2+} . In addition, the small peaks due to side reactions disappeared after Cu^{2+} injection because the $\text{Fe}(\text{CN})_6^{3-}$ ions of the surface modifier were converted to CuHCF-NPs.

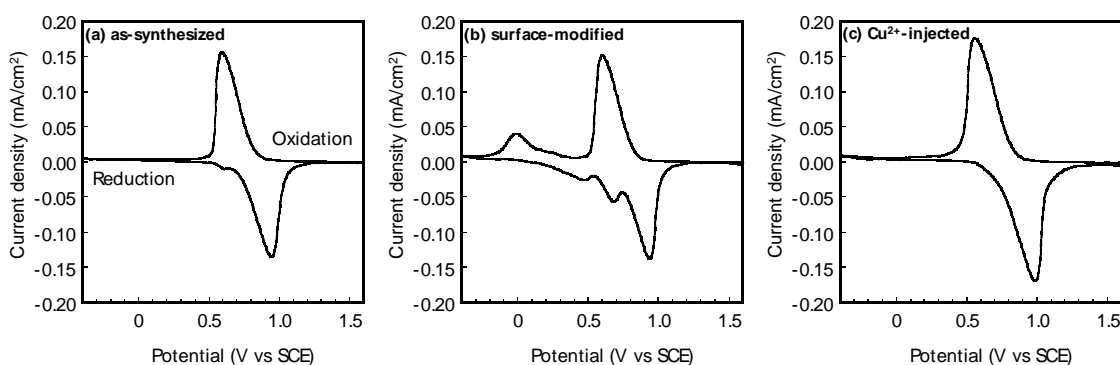


Figure 4.6 Cyclic voltammograms of the CuHCF films. (Scan rate: 5 mV/s)

4.3.6 Electrochromic properties

Figure 4.7 shows the absorbance spectra of the each CuHCF film electrodes after reduction (-0.4 V) and oxidation (1.6 V) for 200 s. The values seen in Figure 4.7 indicate the difference in the absorbance ΔA in the reduced and oxidized states at wavelengths of 400 and 500 nm. The broad band at $\lambda = 500$ nm is associated with the CT of iron to copper in cupric ferrocyanide, and the band at $\lambda = 400$ nm is attributed to the CT from cyanide to iron for the ferricyanide species.⁵⁾ The ratios of the percent increases in absorbance at 400 and 500 nm ($\Delta A_{400\text{nm}}$ and $\Delta A_{500\text{nm}}$) following surface modification and Cu^{2+} injection are listed in Table 4.4. The $\Delta A_{500\text{nm}}/\Delta A_{400\text{nm}}$ of the surface-modified CuHCF film was 24% after surface modification, and this value corresponds well to the 39% decrease in the amount of copper shown in Table 4.3. In addition, the 32% increase in the $\Delta A_{500\text{nm}}/\Delta A_{400\text{nm}}$ value for the Cu^{2+} -injected CuHCF-NP film corresponds to the 39% increase in copper shown in Table 4.3. These results indicate that the absorbance spectra can be explained by the change in the chemical compositions of the CuHCF film electrodes.

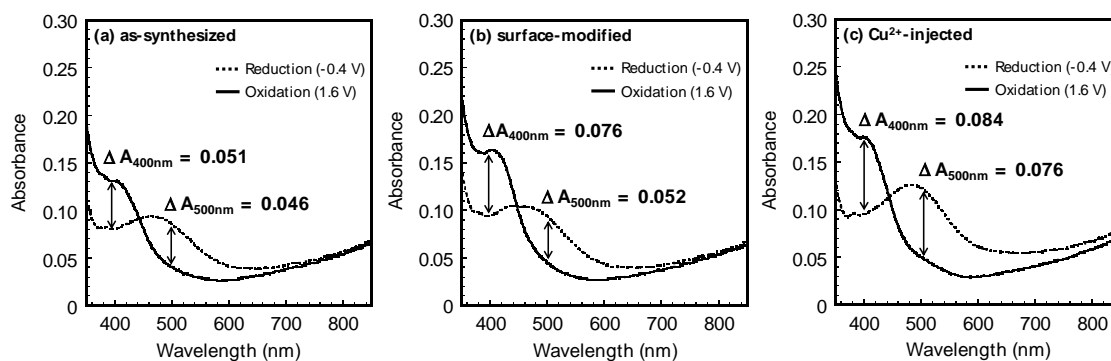


Figure 4.7 Absorbance spectra for CuHCF thin films in the reduced and oxidized states measured after application of constant voltages at -0.4 V and 1.6 V (vs. SCE), respectively, for 200 s.

Table 4.4 Change in the absorbance of the CuHCF films

CuHCF film	$\Delta A_{500\text{nm}}/\Delta A_{400\text{nm}}$	Percent change
as-synthesized	0.90	
surface-modified	0.68	-24%
Cu^{2+} -injected	0.90	+32%

4.4 Summary

Insoluble and aggregated CuHCF particles were synthesized for the first time using a micro-mixer. The insoluble CuHCF particles were then converted into water-dispersible CuHCF-NPs using a surface modifier. Finally, a film prepared from the soluble surface-modified CuHCF-NPs film was converted to an insoluble CuHCF-NPs film using Cu^{2+} injection.

The quantity of iron and copper ions in the as-synthesized and Cu^{2+} -injected CuHCF-NPs films corresponded to the changes in the absorbance of the films at 400 and 500 nm. This quantitative agreement can be explained by the charge-transfer absorbance of Fe and Cu species in the CuHCF films.

References

- 1) M. Ishizaki, M. Sakamoto, H. Tanaka, T. Kawamoto, M. Kurihara: *Mol. Cryst. Liquid Cryst.* **539** (2011) 18.
- 2) A. Gotoh, H. Uchida, M. Ishizaki, T. Satoh, S. Kaga, S. Okamoto, M. Ohta, M. Sakamoto, T. Kawamoto, H. Tanaka, M. Tokumoto, S. Hara, H. Shiozaki, M. Yamada, M. Miyake, M. Kurihara: *Nanotechnology* **18** (2007) 345609.
- 3) M. Ishizaki, K Kanaizuka, M. Abe, Y. Hoshi, M. Sakamoto, T. Kawamoto, H. Tanaka, M. Kurihara: *Green Chem.* **14** (2012) 1537.
- 4) D. R. Shankaran, S. S. Narayanan, Fresenius: *J. Anal. Chem.* **364** (1999) 686.
- 5) L. M. Siperko, T. Kuwana: *J. Electrochem. Soc.* **130** (1983) 396.
- 6) M. Giorgetti, L. Guadagnini, D. Tonelli, M. Minicucci, and G. Aquilanti: *Phys. Chem. Chem. Phys.* **14** (2012) 5527.

Chapter 5 Effects of Substrate Temperature on the Electrochromic Properties of Cobalt Oxide and Oxyhydroxide Thin Films Prepared by Reactive Sputtering Using O₂ and H₂O Gases

5.1 Introduction

A Co oxide film is an anodically coloring electrochromic material that is becoming increasingly important in the field of ECDs. It is used as ion storage and second EC layers that are colored by oxidation.¹⁻²⁾ The EC of Co oxide is similar to that of Ni oxide, for which the oxidized form (NiOOH) is a dark brown, and the reduced form (Ni(OH)₂) is transparent.³⁻⁴⁾

Various methods have been developed for the preparation of Co oxide films.⁵⁻¹⁰⁾ However, cobalt hydroxide thin films have been mainly prepared by wet-processing techniques such as electrodeposition¹¹⁻¹²⁾ and chemical bath deposition,¹³⁾ and applications of dry-processing techniques are scarce.

Sputtering techniques have been widely used to fabricate metal and oxide thin films because it is superior in its ability to form large-area films with high productivity, and the stoichiometry of the deposited films can be easily controlled. In our laboratory, Ueta *et al.*¹⁴⁾ prepared nickel hydroxide thin films by reactive sputtering using an O₂ + H₂O mixed gas and obtained an EC coloration efficiency of 29 cm²/C in a 1 M aqueous KOH electrolyte solution. Moreover, Li *et al.*¹⁵⁾ prepared hydrated ZrO₂ thin films by reactive sputtering in an H₂O atmosphere and found that substrate cooling was very effective for increasing the H₂O content and decreasing the film density and resulted in high proton-conductivity films.

In this study, the sputter deposition of cobalt oxide and hydroxide thin films in O₂ and H₂O gases was performed, and the structure and electrochemical properties of the thin films were investigated with the aim of clarifying the applicability of sputtering techniques to the fabrication of cobalt hydroxide thin films.

5.2 Experimental procedures

5.2.1 Preparation of Co oxide and oxyhydroxide thin films

Thin films with a thickness of approximately 100 nm were prepared using an RF magnetron sputtering apparatus, as schematically shown in Figure 5.1. A 2-inch Co target disk (99.9% purity) was sputtered with O_2 and H_2O gases. The total sputtering gas pressure and sputtering power were maintained at 6.7 Pa and 50 W, respectively. The substrate temperature was varied from $-20\text{ }^\circ\text{C}$ to $200\text{ }^\circ\text{C}$. Glass, Si, and ITO-coated glass were used as substrates. The deposition rate of the films prepared in O_2 gas was $0.6 \sim 0.7\text{ nm/min}$, and no remarkable temperature dependence was observed. On the other hand, the deposition rate of the films deposited in H_2O gas decreased from 1.2 nm/min at a substrate temperature of $-20\text{ }^\circ\text{C}$ to 0.5 nm/min at a substrate temperature of $200\text{ }^\circ\text{C}$. In Table 5.1, the sputter parameters used in this study are summarized.

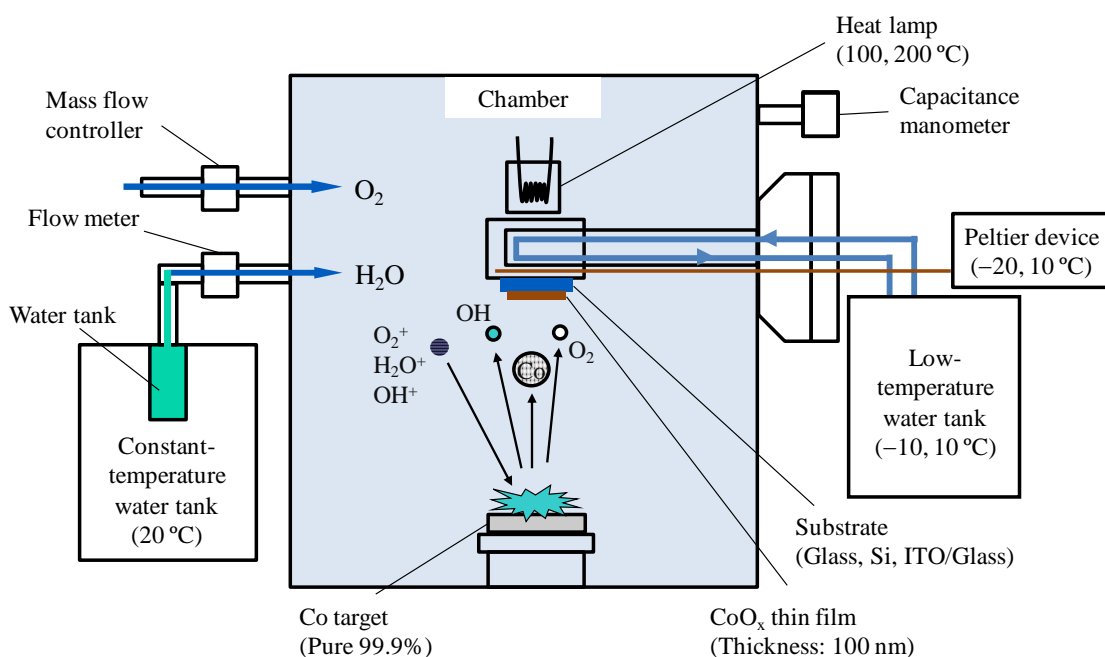


Figure 5.1 Schematic illustration of the RF magnetron sputtering apparatus.

Table 5.1 Summary of the sputtering parameters for the deposition of Co oxide and oxyhydroxide thin films.

Apparatus	RF magnetron sputtering
Target	Co (Purity 99.9%)
Substrate	Glass, Si, ITO/Glass
Sputtering gas	O ₂ , H ₂ O
Gas pressure	6.7 (Pa)
Gas flow rate	1 (ccm)
Sputter power	50 (W)
Substrate temperature	-20, 10, 100, 200 (°C)
Film thickness	100 (nm)
Deposition rate	O ₂ (0.6 ~ 0.7), H ₂ O (0.5 ~ 1.2) (nm/min)

5.2.2 Characterization methods

The film thickness was measured by multi-beam interferometry. The crystal structures of the deposited films were characterized by XRD analysis (X'pert PRO, PANalytical) at room temperature using Cu K α ($\lambda = 1.54 \text{ \AA}$) radiation in the 2θ range from 10° to 65° . The film density and optical properties were characterized by XRR analysis (X'pert PRO, PANalytical), and UV vis spectrophotometry (U-2910, HITACHI), respectively. The chemical bonding state was evaluated by FTIR (FT-IR 6100, JASCO Inc.). The plasma state during sputtering was characterized by plasma emission spectroscopy (S2000 fiber optic spectrometer, Ocean Optics Inc.). CV (HSV-100, Hokuto Denko, Japan) and *in situ* optical modulation measurements (USB2000 Spectrometer, Ocean Optics) were performed in a 0.1 M aqueous KOH electrolyte solution over the voltage scan range from -0.44 to $+0.56$ V and at a potential scan rate of 20 mV/s. Ag/AgCl and Pt were used as the RE and CE, respectively.

5.3 Characterization of cobalt oxide and oxyhydroxide thin films

5.3.1 Plasma emission spectra

Figure 5.2 shows the spectra obtained from plasma emission in O_2 and H_2O gases. Emission peaks due to O_2^+ ions and O atoms are observed for the O_2 plasma. In contrast, the emission peak intensity due to O atoms decreased, and the emission peaks due to H atoms and OH radicals appeared¹⁶⁾ in the spectrum for the H_2O plasma. This result indicates that some H_2O molecules were decomposed into active species, such as O and H atoms and OH radicals, through the following reactions in the plasma:¹⁷⁾



It is thought that the OH radicals and H atoms are incorporated into the films and promote the formation of Co hydroxide.

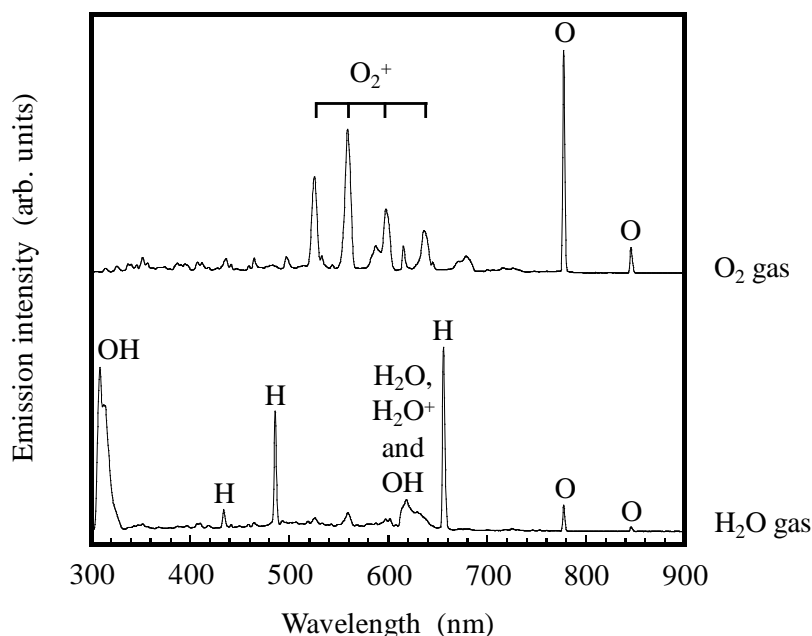


Figure 5.2 Plasma emission spectra in O_2 and H_2O gases.

5.3.2 Crystal structure

The structures of the films deposited on Si substrates were studied by XRD analysis using Cu K α radiation. As can be seen in Figure 5.3 (a), the diffraction peaks of the spinel Co₃O₄ phase¹⁸⁾ were observed for the films prepared in O₂ gas at all substrate temperatures. In H₂O gas, diffraction peaks due to the spinel Co₃O₄ phase were observed for the films prepared at substrate temperatures of 100 °C and 200 °C (Figure 5.3 (b)). However, the peak intensity decreased with decreasing substrate temperature, and no remarkable peaks were observed for the films deposited in H₂O gas at 10 °C and -20 °C, which indicates that these films were amorphous.

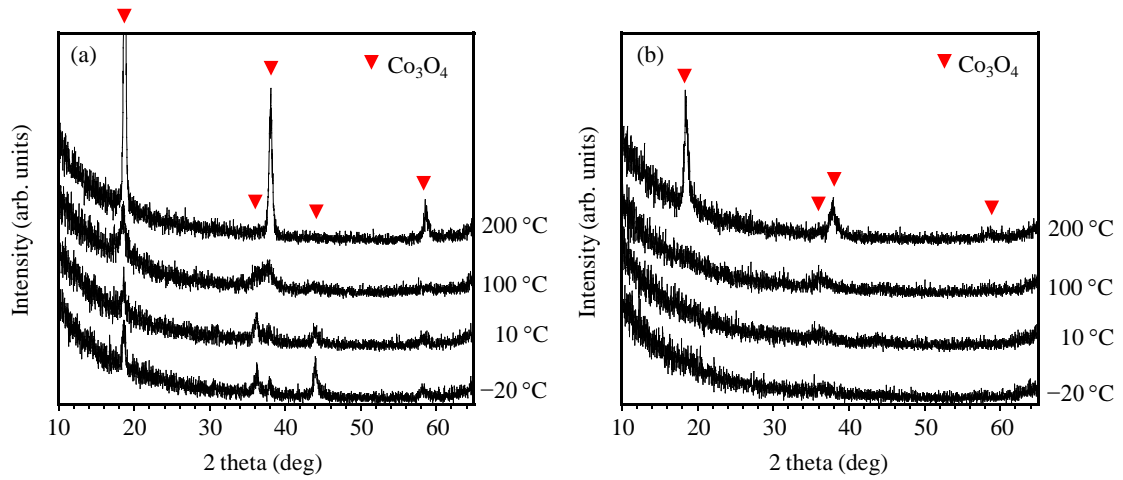


Figure 5.3 XRD patterns of films prepared at various substrate temperatures in O₂ (a) and in H₂O (b) gases.

5.3.3 Chemical bonding state

Figures 5.4 (a) and (b) show the FTIR spectra in the low-wavenumber region for the films deposited on Si substrates at various substrate temperatures in O₂ and H₂O gases. Absorption peaks at 564 ~ 566 and 664 cm⁻¹, were observed for all of the films deposited in O₂ and for the films deposited at 100 °C and 200 °C in H₂O gas. The intensity of the lower-wavenumber peak at 566 cm⁻¹ decreased, and its peak wavenumber shifted to 575 cm⁻¹ for the films deposited in H₂O at lower substrate temperatures. The intensity of the higher-wavenumber peak at 664 cm⁻¹ also decreased with decreasing substrate temperature and nearly disappeared for the film deposited at -20 °C in H₂O. These results indicate that all of the films prepared in O₂ and the films deposited at 100 °C and 200 °C in H₂O were Co₃O₄, and that deposited at a substrate temperatures of 10 °C in H₂O was a mixture of Co₃O₄ and CoOOH, because the absorption peaks at 566 cm⁻¹ and 664 cm⁻¹ have been reported for Co₃O₄¹⁹⁾ and that at 584 cm⁻¹ has been reported for CoOOH²⁰⁾. The film deposited at -20 °C in H₂O is thought to be cobalt oxyhydroxide due to the disappearance of the peak at 664 cm⁻¹.

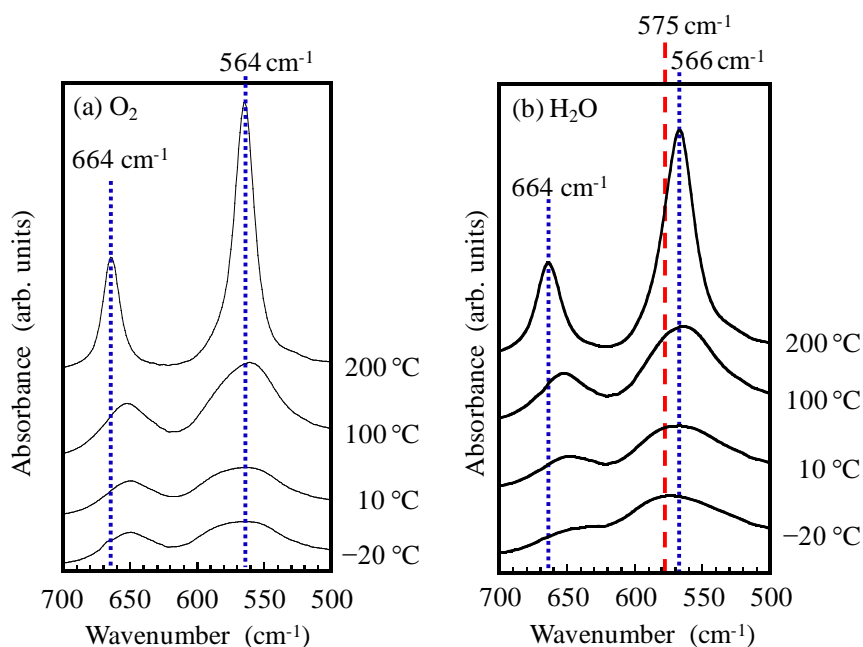


Figure 5.4 FTIR spectra of the films prepared at various substrate temperatures in (a) O₂ and (b) H₂O gases.

5.3.4 Film density

Film density was estimated by XRR analysis. Figure 5.5 presents the obtained XRR data and data simulated using “X’pert Relectivity” software. The film densities were obtained by curve fitting.

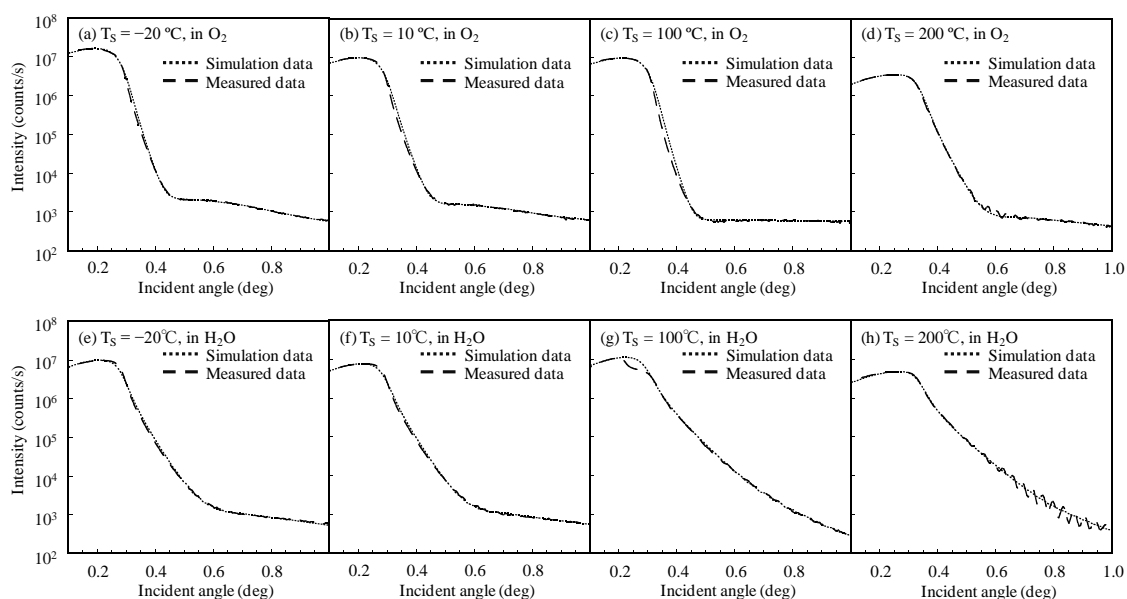


Figure 5.5 Comparison of measured and simulated XRR data for the films deposited in O₂ and H₂O gases at different substrate temperatures.

The film density results are plotted in Figure 5.6 as a function of the substrate temperature. It can be clearly seen in this figure that the film density decreased with decreasing substrate temperature, and the densities of the films deposited in H₂O were lower than those deposited in O₂, which is similar to the results obtained for hydrated ZrO₂.¹⁷⁾ The density of the film prepared at a substrate temperature of -20 °C in H₂O gas was estimated to be approximately 4.2 g/cm³, which is less than that of bulk Co₃O₄ (6.0 g/cm³)¹⁸⁾ and CoOOH (5.2 g/cm³)²¹⁾.

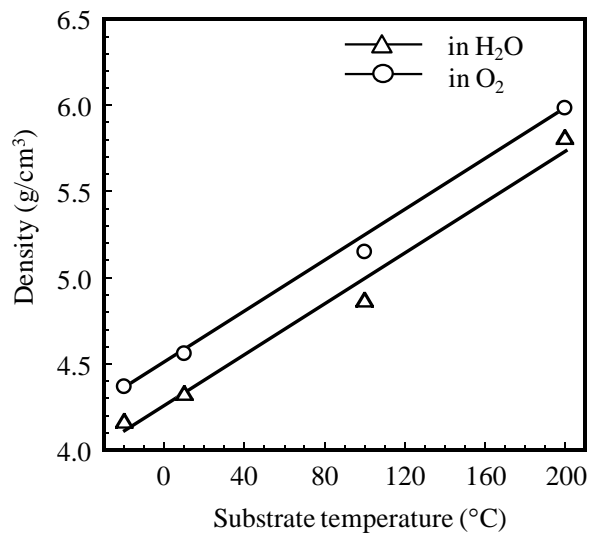


Figure 5.6 Density of the films deposited in O₂ and H₂O gases as a function of substrate temperature.

5.3.5 Electrochemical and electrochromic properties

The electrochemical properties of the films deposited on ITO-coated glass substrates were studied in 0.1 M aqueous KOH electrolyte solutions. Figures 5.7 (a) and (b) show the CV curves for the films deposited at substrate temperatures of -20°C to 200°C . The current density increased with decreasing substrate temperature, which corresponds to the decrease in the film density. Square CV curves were obtained for the films deposited in O_2 and in H_2O at high substrate temperatures of 100°C and 200°C , and redox peaks cannot be clearly observed. However, the redox peaks can be clearly observed in the CV curves for the hydroxide films deposited at substrate temperatures of 10°C and -20°C in H_2O , and the film deposited at -20°C exhibited the highest current density.

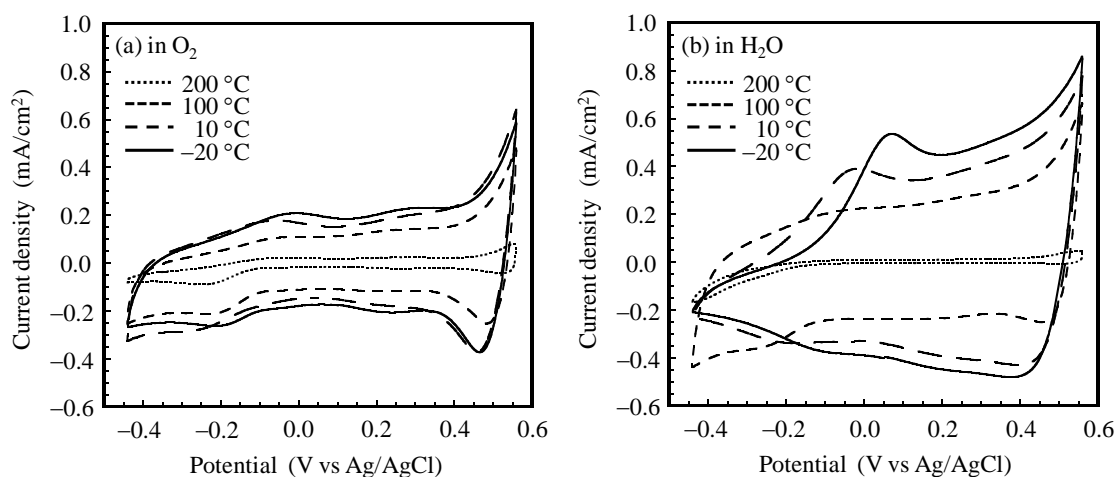


Figure 5.7 Cyclic voltammograms of the films prepared at various substrate temperatures in (a) O_2 and (b) H_2O gases.

The EC properties of the films were also studied in 0.1 M aqueous KOH electrolyte solutions. Figure 5.8 shows the bleached and colored transmittance spectra of the films obtained by applying constant voltages of -0.44 V and $+0.56\text{ V}$ for 5 min.

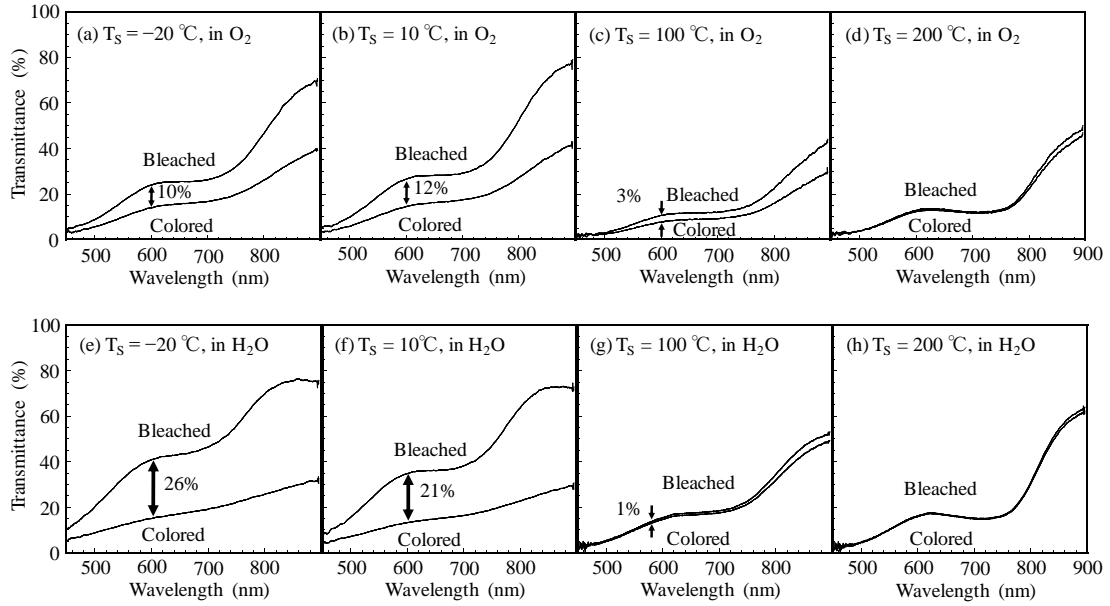


Figure 5.8 Bleached and colored transmittance spectra for the films prepared at various substrate temperature (T_s) in O_2 and H_2O gases.

For the cobalt oxide thin film deposited at $-20\text{ }^\circ\text{C}$ in O_2 gas, a transmittance change of approximately 10% at 600 nm was observed compared to 26% for the cobalt oxyhydroxide thin film deposited at $-20\text{ }^\circ\text{C}$ in H_2O gas. However, the width of the transmittance change decreased with increasing substrate temperature, and no remarkable transmittance change was observed for the films deposited at $200\text{ }^\circ\text{C}$ in either O_2 or H_2O .

The transmittance changes at 600 nm for the thin films deposited in O_2 and H_2O gases over 100 cycles are shown in Figure 5.9. Notably, stable transmittance changes were observed from the first cycle up to 100 cycles. The thin films deposited at $10\text{ }^\circ\text{C}$ and $-20\text{ }^\circ\text{C}$ exhibited larger transmittance changes than those deposited at $100\text{ }^\circ\text{C}$ and $200\text{ }^\circ\text{C}$. Again, the transmittance change of the cobalt oxyhydroxide thin film deposited at $-20\text{ }^\circ\text{C}$ in H_2O gas was larger than that of the cobalt oxide thin film deposited at $-20\text{ }^\circ\text{C}$ in O_2 gas. These results indicate that the increase in the width of the transmittance change with decreasing substrate temperature corresponds to the decrease in the film density.

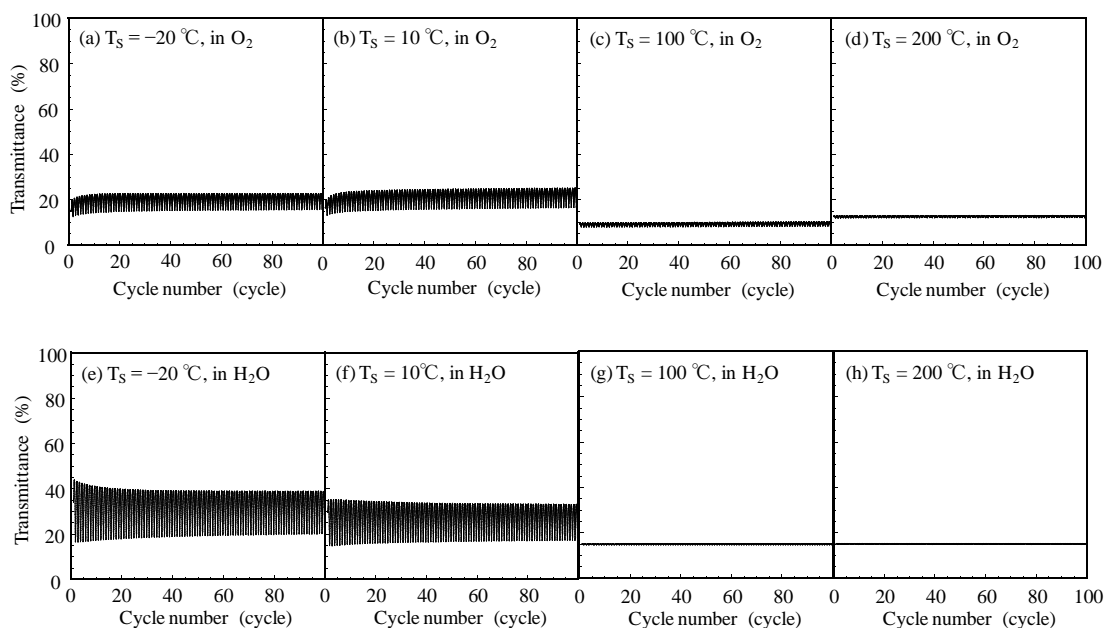


Figure 5.9 Transmittance changes ($\lambda = 600$ nm) for the films prepared at various substrate temperatures (T_s) in O_2 and H_2O gases.

Figure 5.10 shows the transferred charge density (ΔQ) and optical density change (ΔOD) at 600 nm in the bleached and colored states for the films deposited in O_2 and H_2O gases as a function of the substrate temperature. The ΔQ and ΔOD values were obtained from the cyclic voltammograms after 10 cycles and were found to increase with decreasing substrate temperature. The ΔQ and ΔOD values of the films deposited in H_2O gas were higher than those of the films deposited in O_2 gas, and the highest ΔQ (18 mC/cm^2) and ΔOD (0.372) were obtained for the oxyhydroxide film deposited at -20 °C in H_2O . A large EC coloration efficiency of approximately $20 \text{ cm}^2/\text{C}$, which is similar to the reported values for Co oxide films,^{2,4,7)} was obtained, and these values were nearly almost independent of the substrate temperature.

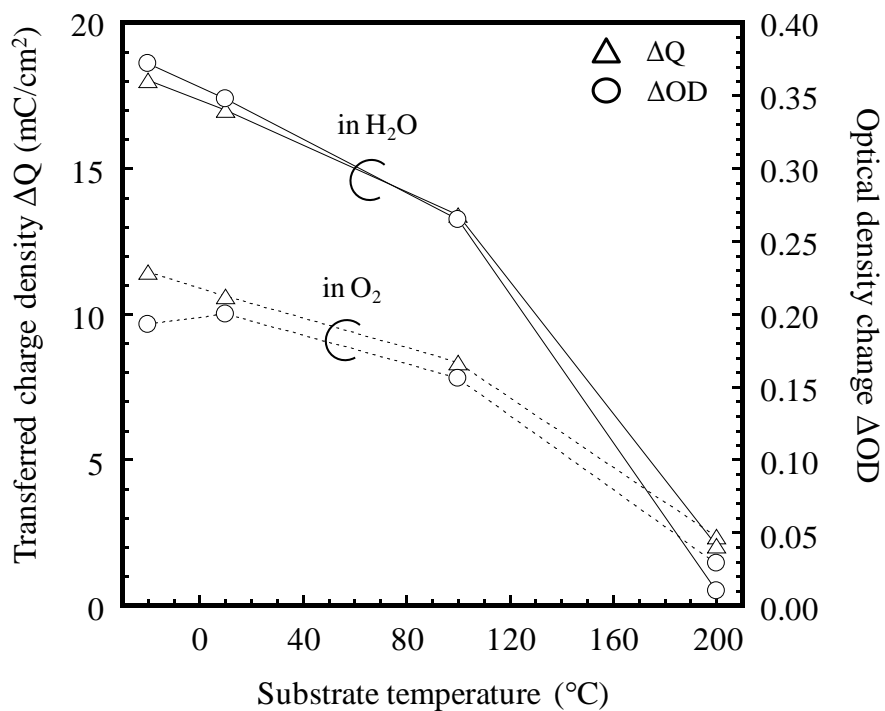


Figure 5.10 Transferred charge density (ΔQ) and optical density change (ΔOD) at 600 nm for the films deposited in O_2 and H_2O gases as a function of substrate temperature.

These results indicate that the substrate temperature has a great influence on the structure and chemical composition of the deposited films and that cobalt hydroxide thin films, which exhibited better electrochromic properties, were prepared at lower substrate temperatures in H_2O . It is thought that the low film density and amorphous structure of the latter films are responsible for the enhancement of electrochromic performance.

5.4 Summary

Cobalt oxide and oxyhydroxide thin films were prepared by reactive sputtering using O₂ and H₂O gases. The electrochemical and EC properties of the cobalt oxide and cobalt oxyhydroxide thin films were examined in 0.1 M aqueous KOH electrolyte solutions, and the highest transmittance change of 26% and EC coloration efficiency of 20 cm²/C were obtained for the cobalt oxyhydroxide film deposited at -20 °C in H₂O gas. Reactive sputtering using H₂O gas at low substrate temperatures was thus found to be a promising method for the fabrication of cobalt oxyhydroxide thin films with good EC properties.

References

- 1) N. Baba, M. Yamana, H. Yamamoto: *Electrochromic Display*, (Sangyo Tosho, Tokyo, 1991) p. 28 [in Japanese].
- 2) F. Švegl, B. Orel, M.G. Hutchins, K Kalcher: *J. Electrochem. Soc.* **143** (1996) 1532.
- 3) P. S. Patil, L. D. Kadam, C. D. Lokhande: *Sol. Energy Mater. Sol. Cells* **53** (1998) 229.
- 4) C. N. Polo da Fonseca, Macro-A. De Paoli, A. Gorenstein: *Sol. Energy Mater. Sol. Cells* **33** (1994) 73.
- 5) H. S. Shim, V. R. Shinde, H. J. Kim, Y. E. Sung, W. B. Kim: *Thin Solid Films* **516** (2008) 8573.
- 6) W. Estrada, M. C. A. Fantini, S. C. de Castro, C. N. Polo da Fonseca, A. Gorenstein: *J. Appl. Phys.* **74** (1993) 5835.
- 7) T. Maruyama, S. Arai: *J. Electrochem. Soc.* **143** (1996) 1383.
- 8) X. H. Xia, J. P. Tu, J. Zhang, X. H. Huang, X. L. Wang, W. K. Zhang, H. Huang: *Electrochem. Commu.* **10** (2008) 1815.
- 9) X. H. Xia, J. P. Tu, J. Zhang, X. H. Huang, X. L. Wang, X. B. Zhao: *Electrochim. Acta* **55** (2010) 989.
- 10) Y. F. Yuan, X. H. Xia, J. B. Wu, J. S. Gui, Y. B. Chen, S. Y. Guo: *J. Membrane Sci.* **364** (2010) 298.
- 11) L. B. Kong, M. C. Liu, J. W. Lang, M. Liu, Y. C. Luo, L. Kang: *J. Solid State Electrochem.* **15** (2011) 571.
- 12) W. J. Zhou, M. W. Xu, D. D. Zhao, C. L. Xu, H. L. Li: *Micropor. Mesopor. Mater.* **117** (2009) 55.
- 13) E. Hosono, S. Fujihara, I. Honma, M. Ichihara, H. Zhou: *J. Power Sources* **158** (2006) 779.
- 14) H. Ueta, Y. Abe, K. Kato, M. Kawamura, K. Sasaki, H. Itoh: *Jpn. J. Appl. Phys.* **48** (2009) 015501.
- 15) N. Li, M. Suzuki, Y. Abe, M. Kawamura, K. Sasaki, H. Itoh, T. Suzuki: *Sol. Energy Mater. Sol. Cells* **99** (2012) 160.

- 16) D. R. Lide: *Handbook of Chemistry and Physics* (CRC Press, Boca Raton, FL, 2003) Sect. 10.
- 17) Y. Abe, H. Ueta, T. Obata, M. Kawamura, K. Sasaki, H. Itoh: *Jpn. J. Appl. Phys.* **49** (2010) 115802.
- 18) International Center for Diffraction Data (ICDD), Power Diffraction File (PDF)-2, Release 2009, reference code 00-042-1467.
- 19) A. S. Bhatt, D. K. Bhat, C. W. Tai, M. S. Santosh: *Mater. Chem. Phys.* **125** (2011) 347.
- 20) C. W. Tang, C. B. Wang, S. H. Chien: *Thermochim. Acta* **473** (2008) 68.
- 21) International Center for Diffraction Data (ICDD), Power Diffraction File (PDF)-2, Release 2009, reference code 00-026-0480.

Chapter 6 Research Summary and Conclusion

6.1 Research summary

Zinc hexacyanoferrate nanoparticles (ZnHCF-NPs) were classified by a centrifugal separation method, and ZnHCF-NPs thin films were deposited on ITO/glass substrates. The EC properties of the ZnHCF-NP thin films improved with decreasing particle size, and a large current density and long cycle durability were obtained for the films with average particles sizes less than 100nm. Furthermore, ZnHCF-NP ECDs fabricated using FeHCF-NPs thin films exhibited improvement in transmission spectra and response properties compared to NiHCF-NP ECDs. An increase in the surface area of ZnHCF-NPs and a decrease in the ion-diffusion path for K^+ ion acceptance from the electrolyte are thought to cause the improvement EC properties.

Copper hexacyanoferrate (CuHCF) was synthesized by a micro-mixer method. The disadvantages of surface-modified CuHCF-NPs, such as side reactions and high solubility in aqueous electrolytes, were overcome using Cu^{2+} injection into a surface-modified film. Cu^{2+} injection removed the surface modifier ($[Fe(CN)_6]^{3-}$) and insolubilized the CuHCF particles due to the formation of CuHCF by the reaction of Cu^{2+} and $[Fe(CN)_6]^{3-}$. In addition, the quantitative relationship between the amount of Fe and Cu ions and the electrochromic properties was discussed.

Cobalt oxide and hydroxide thin films were deposited by a reactive sputtering method. The transferred charge density and optical density change increased with decreasing substrate temperature, and the CoOOH films deposited in an H_2O atmosphere exhibited transmittance changes greater than those observed for Co_3O_4 films deposited in an O_2 atmosphere. The largest transferred charge density and optical density changes were obtained for the CoOOH thin film deposited in an H_2O atmosphere at $T_s = -20$ °C. The low film density and amorphous structure of the CoOOH thin films are thought to cause the improvement in EC properties.

6.2 Conclusion

In this dissertation, new methods for the preparation of MHCF and oxide thin films with good EC properties were presented.

1) Particle size classification of powdery MHCFs with different sizes using an ultracentrifuge is a promising method for improving the EC properties of these materials.

2) The micro-mixer synthesis method for MHCFs is expected to lead to the low-cost, mass production of ECDs.

3) Chemical modification by Cu^{2+} injection into aqueous solutions of water-dispersible MHCFs to enable the deposition of the MHCF films, is a method that can be applied for the fabrication of ECDs with aqueous electrolytes.

4) RF magnetron sputtering deposition using H_2O process gas at low substrate temperatures is a promising method for the fabrication of homogenous large-area oxyhydroxide thin films with good EC properties.

These new methods will contribute to the development of future low-cost, large-area ECDs that can be mass-produced with high performances.

Achievements of This Research

Journal Papers

- 1) K.M. Lee, Y. Abe, M. Kawamura, and Kyung Ho Kim: “Effects of substrate temperature on electrochromic properties of cobalt oxide and oxyhydroxide thin films prepared by reactive sputtering using O₂ and H₂O gases”, Jpn. J. Appl. Phys. **51** (2012) 045501.
- 2) K.M. Lee, H. Tanaka, K. H. Kim, M. Kawamura, Y. Abe, and T. Kawamoto: “Improvement of redox reactions by miniaturizing nanoparticles of zinc Prussian blue analog”, Appl. Phys. Lett. **102** (2013) 141901.

International Conferences

- 1) K.M. Lee, Y. Yamamoto, Y. Abe, M. Kawamura, K. Sasaki, and H. Itoh: “Preparation of Co₃O₄-CoOOH composite films by reactive sputtering and their electrochromic property”, International Union of Materials Research Societies - International Conference on Electronic Materials 2010, Goyang, Korea (2010.8).
- 2) K.M. Lee, Y. Abe, M. Kawamura, and H. Itoh: “Effect of substrate temperature on electrochromic properties of cobalt hydroxide thin films prepared by reactive sputtering”, 2011 Materials Research Society Spring Meetings & Exhibits, San Francisco, USA (2011.4).
- 3) K.M. Lee, T. Kawamoto, H. Tanaka, K. H. Kim, M. Kawamura, and Y. Abe: “Electrochemical properties of zinc Prussian blue analog (Zn-PBA) nanoparticles prepared by ultracentrifuge process”, The 10th International Meeting on Electrochromism, Holland, USA (2012. 8).
- 4) K.M. Lee, H. Tanaka, A. Takahashi, K. H. Kim, M. Kawamura, Y. Abe, and T. Kawamoto: “Electrochromic and electrochemical properties of copper Prussian blue analog nanoparticles prepared by micro flow mixing method”, 224th Electrochemical Society Meeting, San Francisco, USA (2013.10).

Domestic Conference

1) K.M. Lee, Y. Yamamoto, Y. Abe, M. Kawamura, K. Sasaki: Cobalt oxide thin film prepared by reactive sputtering method and their electrochromic property”, The 45th meeting of The Japan Society of Applied Physics (JSAP) Hokkaido Chapter, Sapporo, Japan (2010.1).

(李 慶武、山本 裕貴、阿部 良夫、川村 みどり、佐々木 克孝: “反応性スパッタリング法による酸化コバルト薄膜の作製とそのエレクトロクロミック特性”, 第45回応用物理学会北海道支部, 札幌 (2010.1).)

2) K.M. Lee, Y. Yamamoto, Y. Abe, M. Kawamura, K. Sasaki, H. Itoh: “Optical and electrochromic properties of $\text{Co}_3\text{O}_4\text{-CoOOH}$ mixed films”, The 77th Meeting of The Electrochemical Society of Japan (ECSJ), Toyama, Japan (2010.3).

(李 慶武、山本 裕貴、阿部 良夫、川村 みどり、佐々木 克孝、伊藤 英信: “ $\text{Co}_3\text{O}_4\text{-CoOOH}$ 混合膜の光学・電気化学的特性の評価”, 電気化学会第77回大会, 富山 (2010.3).)

3) K.M. Lee, T. Kawamoto, H. Tanaka, K. H. Kim, M. Kawamura, Y. Abe: “Particle size control of Prussian blue analog (Zn-PBA) nanoparticles prepared by the centrifuge process and their electrochemical properties”, The 79th Meeting of The Electrochemical Society of Japan (ECSJ), Hamamatsu, Japan (2012.3).

(李 慶武、川本 徹、田中 寿、金 敬鎬、川村 みどり、阿部 良夫: “プルシアンブルー類似体(Zn-PBA)ナノ粒子の遠心分離法による粒径制御とその電気化学特性の改善”, 電気化学会第79回大会, 浜松 (2012.3).)

4) K.M. Lee, T. Kawamoto, H. Tanaka, K. H. Kim, M. Kawamura, and Y. Abe: “Electrochromic property of zinc Prussian blue analog nanoparticles prepared by ultracentrifuge method” The 28th Lilac Seminar and the 18th Young Researcher Meeting of the Electrochemical Society of Japan (ECSJ), Otaru, Japan (2012.6).

(李 慶武、川本 徹、田中 寿、金 敬鎬、川村 みどり、阿部 良夫: “遠心分離法により作製した亜鉛プルシアンブルー類似体 (Zn-PBA) ナノ粒子のエレクトロクロミック (EC) 特性”, 電気化学会北海道支部・第28回ライラックセミナー・第18回若手研究者交流会, 小樽 (2012.6).)

5) K.M. Lee, H. Tanaka, K. H. Kim, M. Kawamura, Y. Abe, and T. Kawamoto: “Preparation of electrochromic device by using Prussian blue and zinc Prussian blue analog nanoparticles and their improved properties”, The 80th Meeting of The Electrochemical Society of Japan (ECSJ), Sendai, Japan (2013.3).

(李 慶武、田中 寿、金 敬鎬、川村 みどり、阿部 良夫、川本 徹: “プルシアンブルーとジンクプルシアンブルー類似体ナノ粒子を用いたエレクトロクロミックデバイスの作製とその特性の改善”, 電気化学会第 80 回大会, 仙台 (2013.3).)

Others

1) K. M. Lee, Y. Abe, M. Kawamura, and H. Itoh: “Effect of substrate temperature on electrochromic properties of cobalt hydroxide thin films prepared by reactive sputtering”, Materials Research Society Symposium Proceedings, Vol. 1328.

2) Y. Abe, M. Kawamura, K. H. Kim, K.M. Lee: “Sputter deposition technique for smart window electrode”, Chemical Engineering, Vol. 58, No. 11, p. 811.

(阿部 良夫、川村 みどり、金 敬鎬、李 慶武: “スマートウィンドウ用電極材料のスパッタ成膜技術”, 化学工学社ケミカルエンジニアリング, Vol. 58, No. 11, p. 811.)

Acknowledgments

This research would not have been possible without the support of many people. First and foremost I wish to thank my supervisor, Professor **Yoshio Abe** who was abundantly helpful and offered invaluable assistance, support and guidance. He not only taught me about electronic materials and techniques but also broadened my narrow views of science and society. The numerous discussions with him for 5 years helped me to become a mature scientist. In addition, he also helped me earn The Japanese Government Scholarship. I was able to work hard at Kitami Institute of Technology because of this scholarship. I would also like to thank Professor **Midori Kawamura** and Assistant professor **Kyung Ho Kim**. Both encouraged me to do my best, have given me numerous suggestions on my research reports and presentations, and without their knowledge and assistance, this study would not have been successful. My deepest gratitude is also due to the members of the supervisory committee Professor **Shinji Watanabe**, Professor **Keijiro Hiraga** and Associate Professor **Hidenobu Itoh** have provided me with individual advice and comments on my research. The technicians of the Instrumental Analysis Center, Mr. **Misao Yamane** and Mr. **Sho Tokuda**, gave me considerable advice on XRD and FESEM experimental technique.

I am very grateful to the members of the Green Technology Research Group of the Nanosystems Research Institute for Nanotechnology, Materials, and Manufacturing at the National Institute of Advanced Industrial Science and Technology (AIST). First and foremost, I would like to thank my adviser at AIST, Dr. **Tohru Kawamoto**, for all the exciting moments I shared with him and his group. I have profoundly benefited from my association with them over the past 3 years. I would also like to thank Dr. **Hisashi Tanaka** and Mr. **Akira Takahashi** for their many suggestions regarding my research. In particular, I would like to especially thank Mr. **Hiroshi Watanabe** and Mr. **Yutaka Sugiyama**: I am considerably indebted to them for their valuable advice and scientific discussions about electrochromic experiments, and furthermore, for the precious time they shared to help me with my experiments and provide critical comments. In addition, I wish to thank Mrs. **Keiko Noda** for her experimental assistance and Mrs. **Ken U** for her administrative support on the research conducted at AIST. I also benefited from meetings with Dr. **Akiko Kitajima**, Dr. **Parajuli Durga**, Dr. **Kimitaka Minami**, Dr. **Rongzhi Chen**, Mr. **Naoto Hashimoto**, Mrs. **Miyuki Asai**, Mrs. **Chikako Fukushima**, Ms. **Hiromi Noguchi**, Mr. **Hokuto Hariu**, and Mr. **Kenta Ishigami**.

I also want to thank the students of the Electronic Materials Laboratory at in Kitami institute of Technology, second year masters students, **Geng Jin Tao**, **Yuta Ishizuka**,

Shogo Koino, Ryosuke Todo, Kazuomi Utahiro, and Yuzuru Matsumura, first year masters students **Hongpeng Nie, Zhuguang Jin, and Yoshihisa Kudo**, and fourth year students **Tomoya Chiba, Yasutaka Kato, Tomoyuki Umakoshi, Keisuke Enomoto, Satoshi Ito, Naotake Kimura, Mizuki Sugita, and Tatsuya Sasaki**.

I would like to profoundly thank the Okazaki and Hayase families my Japanese friends, and my Korean seniors and juniors at the Kitami Institute of Technology for the past 5 years. I would also like to thank Professor **WonDuck Kim**, Professor **MuKun Roh**, Professor **Hyun Pack**, Professor **KyungNam Kim**, Professor **JuYoung Kim**, and Professor **SunGi Shin** of the Kangwon National University in Korea. They gave me considerable advice about my study abroad.

Lastly, I wish to thank my father, mother, and brother for their constant support and unconditional love. I love you all dearly.